

1 SEARCH FOR $t\bar{t}Z' \rightarrow t\bar{t}t\bar{t}$ PRODUCTION IN THE MULTILEPTON FINAL STATE IN
2 pp COLLISIONS AT $\sqrt{s} = 13$ TEV WITH THE ATLAS DETECTOR

By

Hieu Le

A DISSERTATION

Submitted to
Michigan State University
in partial fulfillment of the requirements
for the degree of

Physics — Doctor of Philosophy

2025

12

ABSTRACT

13 This dissertation presents a search for a new beyond-the-Standard-Model (BSM) particle
14 at the Large Hadron Collider (LHC). Many BSM models predict a new heavy vector boson
15 (Z') that couples primarily to the top quark in both production and decay (topophilic). The
16 search is performed in multilepton events consistent with four-top-quark ($t\bar{t}t\bar{t}$) production,
17 due to the distinctive signature of the multilepton final states and its robustness against
18 common background processes at the LHC. Analysis data was collected by the ATLAS
19 detector from 2015 to 2018, using proton-proton collisions at the LHC at a center-of-mass
20 energy of 13 TeV. No statistically significant deviation from Standard Model predictions is
21 observed. Exclusion limits are set on the production cross section of the targeted topophilic
22 particle in the mass range between 1 TeV and 3 TeV.

ACKNOWLEDGMENTS

24 First and foremost, I am deeply grateful for my dissertation advisor and P.I, Professor
25 Reinhard Schwienhorst, for his support, guidance and tolerance as part of my role in ATLAS
26 and my doctoral program at Michigan State. Reinhard is the primary driving force in many
27 exciting opportunities that I've had the chance to experience, and he also provides much-
28 appreciated support both in knowledge and wisdom in times of need. I am incredibly thankful
29 that Reinhard is one of the people that plays a part in who I am today.

30 I would like to express sincere gratitude to one of our postdocs in the MSU ATLAS
31 group, Binbin Dong, who I closely worked with within ATLAS. Binbin is a massive source
32 of support for physics, technical and ATLAS-specific knowledge that played a pivotal role
33 during my training with ATLAS, during the analysis in this dissertation, and during my
34 time at CERN. I would have never been able to find my way through without her help.

35 I am also extremely thankful for the MSU ATLAS group, in particular Professors Wade
36 Fisher and Daniel Hayden, for their guidance and feedback on my professional and per-
37 sonal endeavors which helped immensely in my development both scientifically and socially.
38 I thank Rongqian Qian and Jason Gombas, my fellow advisees that offered great ideas,
39 knowledge and friendship. I would like to thank Julia Hinds, Stergios Kazakos and Pratik
40 Kafle for their support and companionship during my time at CERN. I also thank former and
41 presents members of our group that I've had the pleasure to work with: Joey Huston, Jos
42 Gabriel Reyes Rivera, Cecilia Imthurn, Xinfei Huang, Ahmed Tarek, Kyle Fielman, Robert
43 Les and Trisha Farooque. It was a wonderful experience being part of the MSU ATLAS
44 group and I hope our group continues to grow, even if it makes scheduling weekly meetings
45 for everyone that much harder.

46 I would like to express my gratitude to my dissertation committee members, Professors
47 Reinhard Schwienhorst, Johannes Pollanen, Wade Fisher, Remco Zegers and Yuying Xie, for
48 their guidance, patience and commitment to my growth and success as a researcher and a
49 person.

50 It has been a pleasure to work with the many outstanding people in ATLAS, especially
51 the BSM multi-top analysis team. I would like to thank Philipp Gadow, Krisztian Peters,
52 Frédéric Déliot and Neelam Kumari for their dedication and commitment to fostering a
53 successful and fruitful collaboration. I also thank Meng-Ju Tsai, Hui-Chi Lin, Thomas
54 Nommensen, Jianming Qian, Quake Qin, Tomke Schröer, Xilin Wang, Helena Gomez and
55 Daniela Paredes for their tireless efforts in the analysis. I am truly glad to have had the
56 chance to work with all of you.

57 Special thanks to my fellow graduate students that I have had the chance to befriend
58 during my doctoral journey: Daniel Lay, Grayson Perez, Jordan Purcell, Eric Flynn, Isabella
59 Molina, Mo Hassan, Cavan Maher and Hannah Berg. You all taught me a lot more than I
60 could ever imagine and helped me more than I could ever asked for, and I look forward to
61 see where we go from here.

62 Finally, I would like to thank my family, to whom this dissertation is dedicated: my
63 spouse Allen Sechrist, for encouraging me tirelessly everyday and always being there for me
64 even when I can't be there for myself; my cat Eddie, for being the best cat anyone could ask
65 for; my brother Hien Le, my dad Bac Le, and my mom Thuy Cao, for their endless love and
66 support. Thank you for being the reason that I am where I am today.

TABLE OF CONTENTS

67	List of Tables	vii
68	List of Figures	ix
69	KEY TO ABBREVIATIONS	xii
70	Chapter 1. Introduction	1
71	Chapter 2. Theoretical Overview	5
72	2.1 The Standard Model	5
73	2.1.1 Elementary particles	5
74	2.1.2 Mathematical formalism	9
75	2.1.2.1 Quantum chromodynamics	10
76	2.1.2.2 Electroweak theory	11
77	2.1.2.3 Higgs mechanism	14
78	2.2 Beyond the Standard Model: $t\bar{t}Z' \rightarrow t\bar{t}t\bar{t}$	17
79	2.2.1 Top-philic vector resonance	17
80	2.2.2 Production channels	19
81	2.2.3 Decay modes	20
82	Chapter 3. LHC & ATLAS Experiment	22
83	3.1 The Large Hadron Collider	22
84	3.1.1 Overview	22
85	3.1.2 LHC operations	24
86	3.1.3 Physics at the LHC	25
87	3.2 The ATLAS detector	25
88	3.2.1 Inner detector	28
89	3.2.2 Calorimeter systems	29
90	3.2.3 Muon spectrometer	31
91	3.2.4 Trigger & data acquisition	33
92	Chapter 4. Particle Reconstruction & Identification	34
93	4.1 Primary reconstruction	34
94	4.1.1 Tracks	34
95	4.1.2 Vertices	35
96	4.1.3 Topological clusters	36
97	4.2 Jets	37
98	4.2.1 Jet reconstruction	38
99	4.2.2 Flavor tagging	39
100	4.3 Leptons	43
101	4.3.1 Electrons	43
102	4.3.2 Muons	46

103	4.4	Missing transverse momentum	48
104	4.5	Overlap removal	49
105	4.6	Object definition	50
106	Chapter 5. Data & Simulated Samples	51
107	5.1	Data samples	51
108	5.2	Monte Carlo samples	51
109	5.2.1	$t\bar{t}Z'$ signal samples	52
110	5.2.2	Background samples	54
111	Chapter 6. Analysis Strategy	59
112	6.1	Event selection	59
113	6.1.1	Event categorization	60
114	6.2	Analysis regions	61
115	6.2.1	Signal regions	63
116	6.2.2	Control regions	64
117	6.3	Background estimation	67
118	6.3.1	Template fitting for fake/non-prompt estimation	68
119	6.3.2	Charge misidentification data-driven estimation	69
120	6.3.3	$t\bar{t}W$ background data-driven estimation	71
121	Chapter 7. Systematic Uncertainties	74
122	7.1	Experimental uncertainties	74
123	7.1.1	Luminosity & pile-up reweighting	74
124	7.1.2	Leptons	74
125	7.1.3	Jets	75
126	7.1.4	Missing transverse energy	77
127	7.2	Modeling uncertainties	78
128	7.2.1	Signal and irreducible background uncertainties	78
129	7.2.2	Reducible background uncertainties	80
130	Chapter 8. Results	82
131	8.1	Statistical interpretation	82
132	8.1.1	Profile likelihood fit	82
133	8.1.2	Exclusion limit	85
134	8.2	Fit results	87
135	Chapter 9. Summary	97
136	References	98

¹³⁷ List of Tables

¹³⁸ 137	Table 4.1: Overlap removal process for this analysis, applied sequentially from top to bottom.	49
¹⁴⁰ 141	Table 4.2: Summary of object selection criteria used in this analysis. ℓ_0 refers to the leading lepton in the event.	50
¹⁴² 143	Table 5.1: Summary of all HLT triggers used in this analysis. Events are required to pass at least one trigger.	52
¹⁴⁴ 145 ¹⁴⁶ ¹⁴⁷	Table 5.2: Summary of all Monte-Carlo samples used in this analysis. V refers to an EW ($W^\pm/Z/\gamma^*$) or Higgs boson. Matrix element (ME) order refers to the order in QCD of the perturbative calculation. Tune refers to the underlying-event tune of the parton shower (PS) generator.	53
¹⁴⁸ 149 ¹⁵⁰ ¹⁵¹ ¹⁵² ¹⁵³	Table 6.1: Definitions of signal, control and validation regions (VR) used in this analysis. N_{jets} and N_b refers to the number of jets and number of b -tagged jets respectively. ℓ_1 refers to the leading lepton, ℓ_2 refers to the subleading lepton and so on. H_T refers to the p_T scalar sum of all leptons and jets in the event. $m_{\ell\ell}$ refers to the dilepton invariant mass, which must not coincide with the Z -boson mass range of 81-101 GeV for SS2L+3L events.	62
¹⁵⁴ 155	Table 6.2: Definitions of SR sub-regions. Events are sorted into different sub-regions based on the number of b -tagged jets and leptons present.	63
¹⁵⁶	Table 6.3: List of possible assigned values for DFCAA.	66
¹⁵⁷ 158 ¹⁵⁹ ¹⁶⁰	Table 8.1: Normalization factors for backgrounds with dedicated CRs, obtained from a simultaneous fit in all CRs and SR under the background-only hypothesis. The nominal pre-fit value is 1 for all NFs and 0 for the scaling factors a_0 and a_1 . Uncertainties shown include both statistical and systematic uncertainties.	89

161	Table 8.2: Pre-fit and post-fit background yields in the inclusive SR. The number of 162 data events and pre-fit estimate signal yields are also shown. Background 163 yields shown are obtained using the $t\bar{t}Z'$ signal sample with $m_{Z'} = 2$ TeV. 164 Total yield uncertainty differs from the quadrature sum of constituent un- 165 certainties due to (anti-)correlation effects. [†] Pre-fit yields for $t\bar{t}W$ back- 166 ground are nominally set to 0 prior to data-driven normalization. Yields 167 shown are estimated using best fit parameters.	94
168	Table 8.3: Post-fit impact of uncertainty sources on the signal strength μ , grouped by 169 categories. Values shown are obtained from the fit using the $t\bar{t}Z'$ signal 170 sample with $m_{Z'} = 2$ TeV. Impact on μ is evaluated for each uncertainty 171 category by re-fitting with the corresponding set of NPs fixed to their best- 172 fit values. Total uncertainty differs from the quadrature sum of constituent 173 uncertainties due to correlation between NPs in the fit.	95

List of Figures

174	Figure 2.1: Particles within the SM and their properties.	6
176	Figure 2.2: Feynman diagram for $t\bar{t}$ production and subsequent decay processes. Top quark decays into a W -boson and b -quarks, and W -boson can decay to a $q\bar{q}$ or a $\ell\nu_\ell$ pair.	8
179	Figure 2.3: Illustration of a common representation of the Higgs potential. Before SSB, the ground state $\phi(0)$ is located at A which is symmetric with respect to the potential. A perturbation to this state fixes the ground state energy $ \phi(0) ^2$ to a particular value at B, "spontaneously" breaking the symmetry and degeneracy in $ \phi(0) ^2$	15
184	Figure 2.4: Feynman diagrams for tree level Z' production in association with (a) $t\bar{t}$, (b) tj (light quark) and (c) tW , decaying to final states containing (a) $t\bar{t}t\bar{t}$ or (b)(c) $t\bar{t}t$	19
187	Figure 2.5: Theoretical $t\bar{t}Z'$ production cross-section times $Z' \rightarrow t\bar{t}$ branching ratio as a function of the Z' mass at LO in QCD coupling to top with $c_t = 1$ under a simplified top-philic model.	20
190	Figure 2.6: Branching ratios for $t\bar{t}t\bar{t}$ decay. The same-sign dilepton and multilepton channels together forms the SSML channel.	21
192	Figure 3.1: The full CERN accelerator complex as of 2022.	23
193	Figure 3.2: Current and future timeline of LHC operations as of 2025 with corresponding center-of-mass energies and projected integrated luminosities. . .	24
195	Figure 3.3: Summary of predicted and measured cross-section for SM processes at the LHC at different center-of-mass energies	26
197	Figure 3.4: A cross section slice of the ATLAS detector showing different subsystems along with visualization of different types of particles traveling through the detector	27

200	Figure 3.5: Cutaway illustration of the inner detector along with its subsystems.	28
201	Figure 3.6: Cutaway illustration of the calorimeter system including the EM, hadronic 202 and LAr forward calorimeters	30
203	Figure 4.1: Stages of topo-cluster formation corresponding to each threshold. In (a), 204 proto-clusters are seeded from cells with adequate signal significance $\zeta_{\text{cell}}^{\text{EM}}$. 205 The clusters are further merged and split in (b) according to a predefined 206 cluster growth threshold. The process stops in (c) when all sufficiently 207 significant signal hits have been matched to a cluster.	37
208	Figure 4.2: Jet energy scale calibration sequence for EM-scale jets.	39
209	Figure 4.3: Overview of the GN2 architecture. The number of jet and track features 210 are represented by n_{jf} and n_{tf} respectively. The global jet representation 211 and track embeddings output by the Transformer encoder are used as 212 inputs for three task-specific networks.	41
213	Figure 4.4: The c -, light- and τ -jet rejection rate as a function of b -tagging efficiency 214 for GN2 and DL1d using (a) jets in the $t\bar{t}$ sample, and (b) jets in the Z' 215 sample. The performance ratios of GN2 to DL1d are shown in the bottom 216 panels.	42
217	Figure 6.1: Post-fit background composition in each analysis region and sub-region. 218 The fit was performed using ideal pseudo-datasets (Asimov data) in the SR. 61	
219	Figure 6.2: Pre-fit kinematic distributions and event compositions in the inclusive 220 SR for (a) H_T i.e. scalar sum of p_T of all objects in the event, (b) jet 221 multiplicity, (c) b -jet multiplicity, (d) leading lepton p_T . The shaded band 222 represents the uncertainty in the total distribution. The first and last bins 223 of each distribution contains underflow and overflow events respectively.	65
224	Figure 6.3: Feynman diagram for one possible $t\bar{t}W$ decay process with similar SS2L 225 lepton signature to the $t\bar{t}Z'$ signal. Usually only two b -jets are present due 226 to CKM suppression of b -quark production from W -boson decays; this is 227 enough to allow $t\bar{t}W$ decays to enter and contaminate the SR.	68
228	Figure 6.4: Charge flip rate calculated for SR and CR $t\bar{t}W$ in bins of $ \eta $ and p_T	71
229	Figure 7.1: Combined QmisID uncertainty rate for SR in bins of $ \eta $ and p_T	81

230	Figure 8.1: Example of an exclusion limit graph. The solid (dotted) line represents the 231 observed (expected) upper limits as a function of the Z' mass at 95% CL 232 on the cross-section of $pp \rightarrow t\bar{t}Z'$ production times the $Z' \rightarrow t\bar{t}$ branching 233 ratio. The solid blue line represents the theoretical signal cross-section 234 with $c_t = 1$ at LO in QCD [74]. The green and yellow bands represent the 235 68% ($\pm 1\sigma$) and 95% ($\pm 2\sigma$) confidence intervals for the expected upper 236 limits. Cross section of $t\bar{t}Z'$ within the region above the observed limit is 237 excluded under the current model. Masses below the $m_{Z'}$ value at which 238 the observed limit intersect the theoretical cross section are excluded.	86
239	Figure 8.2: Comparison between data and post-fit prediction for the discriminant ob- 240 servable in each CR. Distributions shown are obtained from the fit using 241 the $t\bar{t}Z'$ signal sample with $m_{Z'} = 2$ TeV. The lower panel shows the 242 ratio between data and post-fit predictions. The shaded band represents 243 the total uncertainty on the fit. The dashed line represents the pre-fit 244 distribution.	90
245	Figure 8.4: Post-fit pull from nominal values for nuisance parameters representing 246 systematic uncertainties. Systematics pruned during the fit are not shown. 247 The dashed line represents the nominal pre-fit values. The green and 248 yellow bands represent the 68% ($\pm 1\sigma$) and 95% ($\pm 2\sigma$) confidence intervals 249 for the nominal fit value.	93
250	Figure 8.5: Observed (solid line) and expected (dotted line) upper limits as a function 251 of the Z' mass at 95% CL on the cross-section of $pp \rightarrow t\bar{t}Z'$ production 252 times the $Z' \rightarrow t\bar{t}$ branching ratio. The region above the observed limit is 253 excluded. The solid blue line represents the theoretical signal cross-section 254 with $c_t = 1$ at LO in QCD. The green and yellow bands represent the 255 68% ($\pm \sigma$) and 95% ($\pm 2\sigma$) confidence intervals respectively.	96

KEY TO ABBREVIATIONS

257

Physical & Mathematical Quantities

258 χ^2 chi-squared259 d_0 transverse impact parameter260 ΔR angular distance261 \sqrt{s} center-of-mass energy262 η pseudorapidity263 E_T transverse energy264 E_T^{miss} missing transverse energy265 Γ decay width266 γ_5 chirality projection operator267 γ_μ Dirac matrices268 H_0 null hypothesis269 H_T scalar sum of transverse momenta p_T of all objects in an event270 \mathcal{L} Lagrangian271 $\mathcal{L}(\theta)$ likelihood function272 L instantaneous luminosity273 $m_{\ell\ell}$ dilepton invariant mass274 μ signal strength275 μ_F factorization scale276 μ_R renormalization scale277 N_{jets} number of jets/jet multiplicity278 $\mathcal{O}(n)$ on the order of n 279 \mathcal{P} Poisson probability280 p_T transverse momentum

- ²⁸¹ Q electric charge
²⁸² q_μ profile likelihood ratio
²⁸³ σ standard deviation
²⁸⁴ $\sigma[b]$ cross-section
²⁸⁵ z_0 longitudinal impact parameter

Particles & Processes

- ²⁸⁶
- ²⁸⁷ γ^* virtual photon
²⁸⁸ gg gluon-gluon fusion
²⁸⁹ pp proton-proton
²⁹⁰ PbPb lead-lead
²⁹¹ q quark
²⁹² $q\bar{q}$ quark-antiquark pair
²⁹³ $t\bar{t}$ top/anti-top quark pair
²⁹⁴ $t\bar{t}X$ top pair in association with another particle
²⁹⁵ $t\bar{t}t\bar{t}$ four-top-quark
²⁹⁶ V massive vector bosons (W^\pm, Z)
²⁹⁷ H Higgs in association with a vector boson

Acronyms

- ²⁹⁸
- ²⁹⁹ **1LOS** one lepton, or two leptons of opposite charges
³⁰⁰ **2HDM** two-Higgs doublet model
³⁰¹ **AF3** AtlFast3 fast simulation
³⁰² **ALICE** A Large Ion Collider Experiment
³⁰³ **ATLAS** A Toroidal LHC ApparatuS
³⁰⁴ **AWAKE** Advanced WAKEfield Experiment
³⁰⁵ **BDT** boosted decision tree
³⁰⁶ **BR** branching ratio

- ³⁰⁷ **BSM** Beyond the Standard Model
- ³⁰⁸ **CB** combined muon
- ³⁰⁹ **CERN** European Organization for Nuclear Research
- ³¹⁰ **CKM** Cabibbo-Kobayashi-Maskawa matrix
- ³¹¹ **CL** confidence level
- ³¹² **CMS** Compact Muon Solenoid
- ³¹³ **CP** charge-parity symmetry
- ³¹⁴ **CR** control region
- ³¹⁵ **CSC** Cathode Strip Chambers
- ³¹⁶ **CTP** Central Trigger Processor
- ³¹⁷ **ECIDS** Electron Charge ID Selector
- ³¹⁸ **EFT** effective field theory
- ³¹⁹ **EM** electromagnetic
- ³²⁰ **EW** electroweak
- ³²¹ **FASER** ForwArd Search ExpeRiment
- ³²² **FCal** forward calorimeter
- ³²³ **FS** full detector simulation
- ³²⁴ **GNN** graph neural network
- ³²⁵ **GRL** Good Run List
- ³²⁶ **GSC** Global Sequential Calibration
- ³²⁷ **GSF** Gaussian-sum filter
- ³²⁸ **GUT** Grand Unified Theory
- ³²⁹ **HEC** hadronic endcap calorimeter
- ³³⁰ **HF** heavy-flavor
- ³³¹ **HL-LHC** High-Luminosity Large Hadron Collider
- ³³² **HLT** High-Level Trigger
- ³³³ **ID** Inner Detector

- ³³⁴ **IP** interaction point
- ³³⁵ **JER** jet energy resolution
- ³³⁶ **JES** jet energy scale
- ³³⁷ **JVT** Jet Vertex Tagger
- ³³⁸ **KATRIN** Karlsruhe Tritium Neutrino Experiment
- ³³⁹ **L1** Level 1
- ³⁴⁰ **LAr** liquid argon
- ³⁴¹ **LF** light-flavor
- ³⁴² **LH** likelihood
- ³⁴³ **LHC** Large Hadron Collider
- ³⁴⁴ **LHCb** Large Hadron Collider beauty
- ³⁴⁵ **LINAC** linear accelerator
- ³⁴⁶ **LLH** log-likelihood
- ³⁴⁷ **LO** leading order
- ³⁴⁸ **MC** Monte Carlo simulation
- ³⁴⁹ **ME** matrix element
- ³⁵⁰ **ML** multilepton
- ³⁵¹ **MS** Muon Spectrometer
- ³⁵² **MDT** Monitored Drift Tubes
- ³⁵³ **MET** missing transverse energy
- ³⁵⁴ **NF** normalization factor
- ³⁵⁵ **NNJvt** Neural Network-based Jet Vertex Tagger
- ³⁵⁶ **NLO** next-to-leading order
- ³⁵⁷ **NNLO** next-to-next-to-leading order
- ³⁵⁸ **NP** nuisance parameter
- ³⁵⁹ **OP** operating point (also working point)
- ³⁶⁰ **OS** opposite-sign

- ³⁶¹ **PCBT** pseudo-continuous b -tagging
- ³⁶² **PDF** parton distribution function
- ³⁶³ **POI** parameter of interest
- ³⁶⁴ **PS** parton shower
- ³⁶⁵ **PV** primary vertex
- ³⁶⁶ **QCD** quantum chromodynamics
- ³⁶⁷ **QED** quantum electrodynamics
- ³⁶⁸ **QFT** quantum field theory
- ³⁶⁹ **QmisID** charge mis-identification
- ³⁷⁰ **RPC** Resistive Plate Chamber
- ³⁷¹ **SCT** Semiconductor Tracker
- ³⁷² **SF** scale factor
- ³⁷³ **SM** Standard Model
- ³⁷⁴ **SR** signal region
- ³⁷⁵ **SS** same-sign
- ³⁷⁶ **SSB** spontaneous symmetry breaking
- ³⁷⁷ **SS2L** same-sign dilepton
- ³⁷⁸ **SSML** same-sign dilepton, or more than two leptons of any charges
- ³⁷⁹ **TDAQ** Trigger and Data Acquisition
- ³⁸⁰ **TGC** Thin-Gap Chamber
- ³⁸¹ **TRT** Transition Radiation Tracker
- ³⁸² **VEV** vacuum expectation value
- ³⁸³ **VR** validation region
- ³⁸⁴ **UE** underlying-event

³⁸⁵ Chapter 1. Introduction

³⁸⁶ The 20th century ushered in a revolutionary period for mankind's understanding of the
³⁸⁷ fundamental nature of matter and the forces that govern our universe with the development
³⁸⁸ of special relativity and quantum mechanics, which redefined our understanding of space,
³⁸⁹ time, energy and matter at the furthest extremes of scale from the vast reaches of the cosmos
³⁹⁰ to the tiniest constituents of matter. Building on these principles, Quantum Electrodynamics
³⁹¹ (QED) [1–3] was developed as the first successful quantum field theory (QFT) describing
³⁹² electromagnetism. The discovery of beta decay [4] and its paradoxical behaviors within the
³⁹³ framework of QED prompted the prediction of neutrinos and development of the theory of
³⁹⁴ weak interaction.

³⁹⁵ At around the same time, a spectrum of strongly interacting particles was discovered
³⁹⁶ [5] as particle accelerators probed deeper into atomic nuclei, leading to the formation of
³⁹⁷ the quark model in the 1960s and with it a hypothesized new binding force, the strong
³⁹⁸ force. However, the QFT framework remained incapable of describing the weak and strong
³⁹⁹ interactions until advancements in gauge theory and the quantization of non-Abelian gauge
⁴⁰⁰ via QFT resulted in the formation of Yang-Mills theory [6, 7]. This sparked a renaissance
⁴⁰¹ in modern physics with the unification of electromagnetism and weak force in 1967 under
⁴⁰² the framework of electroweak (EW) [8] theory, as well as the development of Quantum
⁴⁰³ Chromodynamics (QCD) [9, 10] to describe the strong force binding quarks.

⁴⁰⁴ At this point, the prediction of massless bosons within EW formalism remained a contra-
⁴⁰⁵ diction to the predicted massive W^\pm and Z bosons that mediate the weak force. This was
⁴⁰⁶ resolved by the introduction of EW spontaneous symmetry breaking and the Higgs mech-
⁴⁰⁷ anism in 1964 [11–13], which explained the generation of masses for both the EW bosons

408 and fermions. Together, these developments culminated in the Standard Model of parti-
409 cle physics SM [14], a comprehensive theory that described the electromagnetic, weak, and
410 strong interactions, classified all known fundamental particles and predicted mathematically
411 consistent but not yet observed particles. Following its inception, particles predicted by the
412 Standard Model were gradually observed experimentally, starting with the gluon in 1979
413 [15], then the W^\pm and Z bosons [16, 17], and finally the top quark in 1995 [18, 19]. The
414 final missing piece was confirmed as the Higgs boson was observed in 2012 independently
415 by the ATLAS [20] and CMS [21] detectors at the Large Hadron Collider, completing the
416 Standard Model after a 40-year search and cementing it as the most successful framework
417 so far describing fundamental constituents of matter and their governing forces.

418 Despite its successes, the Standard Model remains incomplete. Key unanswered questions
419 include the nature of dark matter [22], which makes up about 27% of the universes energy
420 content but has no explanation within the Standard Model; the origin of neutrino masses and
421 their oscillations [23]; the observed matter-antimatter asymmetry in the universe; possible
422 unification of the EW and strong interaction into a Grand Unified Theory (GUT); and the
423 hierarchy problem describing the large discrepancy in scales between forces and the apparent
424 lightness of the Higgs boson compared to values predicted from quantum corrections.

425 After the discovery of the Higgs boson, efforts have been underway to construct new
426 hypotheses and models in search of beyond the Standard Model (BSM) physics via different
427 avenues, one of which being direct searches at colliders for new resonances or particles not
428 predicted by the SM. In particular, the top quark possesses large mass and strong coupling to
429 the Higgs boson [24] which gives it a special role in many proposed BSM models as a possible
430 connection with strong coupling to new particles and heavy resonances. In addition, the
431 top quark has a clean decay signature with well-understood final states and is produced in

abundance at the LHC from pp collisions in the form of top pairs $t\bar{t}$ [25, 26]. This dissertation presents a search for the production of a heavy resonance that couples preferentially to top quark (top-philic) in association with a top pair ($t\bar{t}$) in the final state with either two leptons of the same electric charge or at least three leptons (SSML). The search is performed in proton-proton collisions at $\sqrt{s} = 13$ TeV with the ATLAS detector [27] via the four-top ($t\bar{t}t\bar{t}$) production channel.

A similar search for top-philic heavy resonances was performed using the $t\bar{t}t\bar{t}$ final state containing either one lepton or two opposite-sign leptons (1LOS) [28] with a much larger branching ratio of 56% and larger irreducible background of SM processes. Despite the small cross-section within the SM, the $t\bar{t}t\bar{t}$ SSML final state provides heightened sensitivity to BSM physics and higher signal-to-background ratio than inclusive resonance searches (e.g. in dijet or dilepton final states) due to the distinctive signal signature and suppression of large SM background processes present in $t\bar{t}$ -associated production i.e. diboson (VV), $t\bar{t}$ production with an additional boson ($t\bar{t}V/ttH+jets$) or with additional light leptons from heavy-flavor decays ($t\bar{t} + HF$). The cross-section for $t\bar{t}t\bar{t}$ production can be enhanced by many proposed BSM models including supersymmetric gluino pair-production [29, 30], scalar gluon pair-production [31, 32], top-quark-compositeness models [33, 34], effective field theory (EFT) operators [26, 35–38] and two-Higgs-doublet models (2HDM) [39–43]. Searching within this channel is particularly motivated by the recent observed excess in the measurement of four-top production in the SSML final state at the LHC by the ATLAS detector [44] with a measured cross-section of 24^{+7}_{-6} fb, almost double the SM prediction of $13.4^{+1.0}_{-1.8}$ fb.

A simplified color-singlet vector boson model [45] is employed for the search to minimize parameter dependency on model choice. Data-driven background estimation methods are implemented for $t\bar{t}W$ - one of the dominant irreducible backgrounds in the analysis - and

456 the charge misidentification background to rectify mismodeling related to jet multiplicity
457 in simulated background that were not covered in the previous 1LOS $t\bar{t}Z'$ search [28] and
458 SSML $t\bar{t}H/A \rightarrow t\bar{t}t\bar{t}$ search [46]. These methods are employed similarly to that in previous
459 SM $t\bar{t}t\bar{t}$ analyses [44, 47].

460 This dissertation is organized as follows. Chapter 2 presents the formalism of the SM and
461 relevant BSM concepts. Chapter 3 provides an introduction to the LHC and ATLAS detector.
462 Chapter 4 describes the reconstruction and identification of physics object from detector
463 signals. Chapter 5 defines the data and simulated samples used in the analysis. Chapter 6
464 describes the analysis strategy, including object definition, analysis region description and
465 background estimation methods. Chapter 7 summarizes the uncertainties involved in the
466 analysis. Chapter 8 presents the statistical interpretation and analysis results. Finally,
467 Chapter 9 discusses a summary of the analysis and future outlook.

468 Chapter 2. Theoretical Overview

469 2.1 The Standard Model

470 The Standard Model of Physics (SM) [48] is currently the most successful formalism to
471 describe the physical world at a microscopic scale by providing descriptions for all currently
472 known elementary particles, along with three out of four fundamental forces (electromag-
473 netism, weak force, strong force) with the exception of gravity. The SM is however not
474 perfect, and there remain unanswered questions that require development and discovery of
475 new physics beyond the Standard Model (BSM). This chapter describes an overview of
476 important components within the SM and relevant BSM aspects for this analysis.

477 2.1.1 Elementary particles

478 Elementary particles in the SM can be classified into two groups: bosons consisting
479 of particles following Bose-Einstein statistics with integer spin, and fermions consisting of
480 particles following Fermi-Dirac statistics with half-integer spin. Fermions are the building
481 blocks of composite particles and consequently all known matter, and can be further classified
482 into quarks & leptons. Bosons act as force mediators for all fundamental forces described by
483 the SM, and can either be a scalar boson with spin 0 or vector gauge bosons with spin 1. For
484 each elementary particle, there also exists a corresponding antiparticle with identical mass
485 and opposite charge (electric or color). Figure 2.1 shows all known elementary particles in
486 the SM.

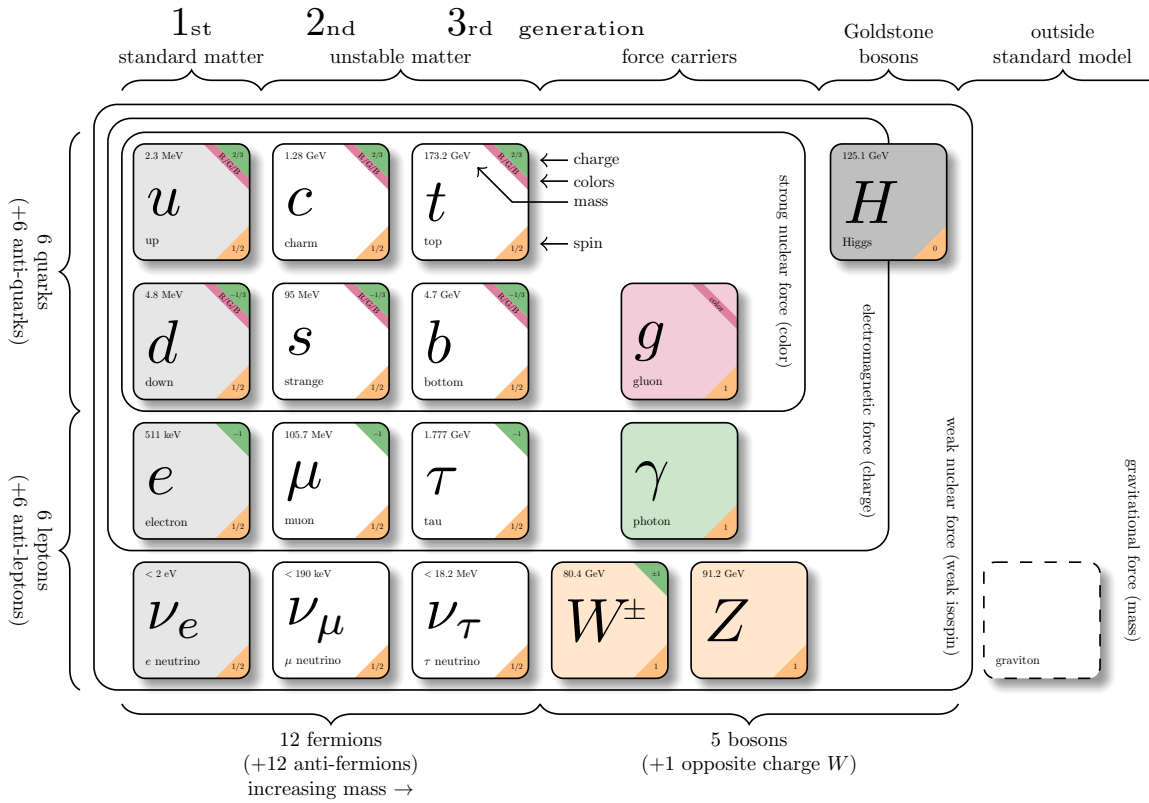


Figure 2.1: Particles within the SM and their properties [49].

487 Fermions

488 Fermions consist of quarks and leptons with six flavors each, grouped into three genera-
 489 tions of doublets. The six quark flavors are up (u), down (d), charm (c), strange (s), bottom
 490 (b) and top (t), arranged in increasing order of mass. The quark flavors form three doublets
 491 (u, d), (c, s) and (t, b), with each doublet containing one quark with electric charge of $+2/3$
 492 (u, s, t), and the other with charge of $-1/3$ (d, c, b). Each quark also possesses a property
 493 known as color charge, with possible values of red (R), green (G), blue (B) or their corre-
 494 sponding anticolor ($\bar{R}, \bar{G}, \bar{B}$). Color charge follows color confinement rules, which allows
 495 only configurations of quarks with total neutral color charge to exist in isolation. Neutral

496 charge configurations can be formed from either a set of three colors (R, G, B), a set of a
497 color and its anticolor, or any combination of the two. Consequently, quarks can only exist
498 in bound states called hadrons and no isolated quark can be found in a vacuum. Quarks are
499 the only elementary particles in the SM that can interact with all four fundamental forces.

500 The three leptons doublets consist of three charged leptons: electron (e), muon (μ), tau
501 (τ), and their respective neutrino flavors: electron neutrino (ν_e), muon neutrino (ν_μ), tau
502 neutrino (ν_τ). Charged leptons carry an electric charge of -1 , while their antiparticles carry
503 the opposite charge ($+1$) and their corresponding neutrino flavors carry no charge. Charged
504 leptons interact with all fundamental forces except the strong force, while neutrinos only
505 interact with the weak force and gravity.

506 **Bosons**

507 The SM classifies bosons into two types: one scalar boson with spin 0 known as the
508 Higgs (H) boson, and vector gauge bosons with spin 1 known as gluons (g), photon (γ), W^\pm
509 and Z bosons [22]. Gluons and photon are massless, while the W^\pm , Z and H bosons are
510 massive. Each vector gauge boson serves as the mediator for a fundamental force described
511 by the SM. Gluons are massless particles mediating the strong interaction by carrying color
512 charges between quarks following quantum chromodynamics (QCD). Each gluon carries a
513 non-neutral color charge out of eight linearly independent color states in the gluon color octet
514 [50]. The photon is the massless and charge-neutral mediator particle for the electromagnetic
515 interaction following quantum electrodynamics (QED). The W^\pm and Z bosons are massive
516 mediator particles for the weak interaction, with the W^\pm boson carrying an electric charge
517 of ± 1 while the Z boson is charge neutral.

518 Other than the vector gauge boson, the only scalar boson in the SM is the massive and

519 charge neutral Higgs boson [22]. The Higgs boson does not mediate any fundamental force
 520 like vector bosons, but serve to provide the rest mass for all massive elementary particles in
 521 the SM through the Higgs mechanism described in section 2.1.2.3.

522 **Top quark**

523 As of now, the top quark (t) is the heaviest particle in the SM with mass of about 173 GeV
 524 [51], approaching the EW symmetry breaking scale. Its high mass gives the top quark the
 525 strongest Yukawa coupling to the Higgs boson ($y_t \approx 1$) [24] and exotic resonances in many
 526 proposed BSM models [52–55], making the top quark and its processes attractive vehicles
 527 with which to probe new physics.

528 Due to its mass, the top quark has a
 529 very short lifetime of 10^{-24} s [22] and de-
 530 cays before it can hadronize following color
 531 confinement. The top quark decays to a W
 532 boson and a b -quark with a branching ratio
 533 of almost 100%. The W boson can subse-
 534 quently decay to a quark-antiquark pair or
 535 to a lepton-neutrino pair (Figure 2.2), with
 536 branching ratios of approximately 68% and
 537 32% respectively. All lepton flavors have
 538 similar branching ratios during a leptonic W
 539 decay.

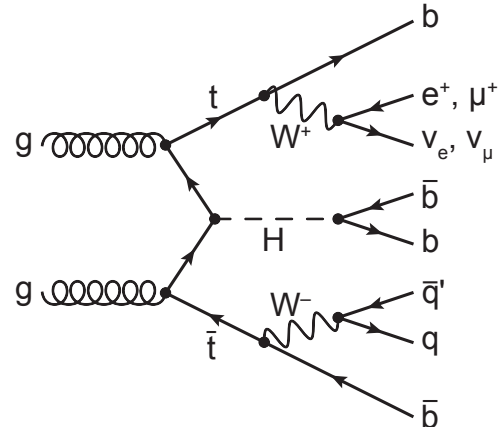


Figure 2.2: Feynman diagram for $t\bar{t}$ production and subsequent decay processes [56]. Top quark decays into a W -boson and b -quarks, and W -boson can decay to a $q\bar{q}$ or a $\ell\nu_\ell$ pair.

540 2.1.2 Mathematical formalism

541 The SM can be described within the formalism of quantum field theory (QFT) with the
542 Lagrangian [57]

$$\mathcal{L}_{\text{SM}} = \mathcal{L}_{\text{QCD}} + \underbrace{(\mathcal{L}_{\text{gauge}} + \mathcal{L}_{\text{fermion}} + \mathcal{L}_{\text{Higgs}} + \mathcal{L}_{\text{Yukawa}})}_{\mathcal{L}_{\text{EW}}} \quad (2.1)$$

543 where \mathcal{L}_{QCD} is the QCD term and \mathcal{L}_{EW} is the electroweak (EW) term of the Lagrangian.
544 Formalism of QFT within the SM treats particles as excitations [58] of their corresponding
545 quantum fields i.e. fermion field ψ , electroweak boson fields $W_{1,2,3}$ & B , gluon fields G_α and
546 Higgs field ϕ .

547 The foundation of modern QFT involves gauge theory. A quantum field has gauge sym-
548 metry if there exists a continuous gauge transformation that when applied to every point in
549 a field (local gauge transformation) leaves the field Lagrangian unchanged. The set of gauge
550 transformations of a gauge symmetry is the symmetry group of the field which comes with
551 a set of generators, each with a corresponding gauge field. Under QFT, the quanta of these
552 gauge fields are called gauge bosons.

553 The SM Lagrangian is gauge invariant under global Poincaré symmetry and local $SU(3)_C \times$
554 $SU(2)_L \times U(1)_Y$ gauge symmetry, with the $SU(3)_C$ symmetry group corresponding to the
555 strong interaction and $SU(2)_L \times U(1)_Y$ to the EW interaction. Global Poincaré symmetry
556 ensures that \mathcal{L}_{SM} satisfies translational symmetry, rotational symmetry and Lorentz boost
557 frame invariance [59]. These symmetries give rise to corresponding conservation laws, which
558 lead to conservation of momentum, angular momentum and energy in the SM as a result of
559 Noether's theorem [60].

560 2.1.2.1 Quantum chromodynamics

561 Quantum chromodynamics is a non-Abelian gauge theory i.e. Yang-Mills theory [6, 7]
 562 describing the strong interaction between quarks in the SM with the gauge group $SU(3)_C$,
 563 where C represents conservation of color charge under $SU(3)_C$ symmetry. According to
 564 QFT, quarks can be treated as excitations of the corresponding quark fields ψ . The free Dirac
 565 Lagrangian for the quark fields $\mathcal{L}_0 = \bar{\psi}(i\gamma^\mu\partial_\mu - m)\psi$ is invariant under global $SU(3)$ sym-
 566 metry, but not under local $SU(3)_C$ symmetry. To establish invariance under local $SU(3)_C$
 567 symmetry, the gauge covariant derivative D_μ is defined so that

$$D_\mu\psi = (\partial_\mu - ig_s G_\mu^a T_a)\psi, \quad (2.2)$$

568 where $g_s = \sqrt{4\pi\alpha_s}$ is the QCD coupling constant, $G_\mu^a(x)$ are the eight gluon fields, and
 569 T_a are generators of $SU(3)_C$, represented as $T_a = \lambda_a/2$ with λ_a being the eight Gell-Mann
 570 matrices [50]. Let the gluon field strength tensors $G_{\mu\nu}^a$ be

$$G_{\mu\nu}^a \equiv \partial_\mu G_\nu^a - \partial_\nu G_\mu^a - g_s f^{abc} G_\mu^b G_\nu^c, \quad (2.3)$$

571 where f^{abc} are the structure constants of $SU(3)_C$. The gauge invariant QCD Lagrangian
 572 can then be written as

$$\begin{aligned} \mathcal{L}_{\text{QCD}} &= \bar{\psi}(i\gamma^\mu D_\mu - m)\psi - \frac{1}{4}G_{\mu\nu}^a G_a^{\mu\nu} \\ &= \underbrace{-\frac{1}{4}G_{\mu\nu}^a G_a^{\mu\nu}}_{\text{gluon kinematics}} + \underbrace{\bar{\psi}(i\gamma^\mu\partial_\mu - m)\psi}_{\text{quark kinematics}} + \underbrace{\bar{\psi}^i(g_s\gamma^\mu(T_a)_{ij}G_\mu^a)\bar{\psi}^j}_{\text{quark-gluon interaction}}, \end{aligned} \quad (2.4)$$

⁵⁷³ where i, j are color indices with integer values from 1 to 3. Gluons are forced to be massless
⁵⁷⁴ from the lack of a gluon mass term to maintain gauge invariance for the Lagrangian.

⁵⁷⁵ **2.1.2.2 Electroweak theory**

⁵⁷⁶ The electroweak interaction is the unified description of the weak interaction and electro-
⁵⁷⁷ magnetism under the $SU(2)_L \times U(1)_Y$ symmetry group, where L represents the left-handed
⁵⁷⁸ chirality of the weak interaction and Y represents the weak hypercharge quantum number.
⁵⁷⁹ Fermions can have either left-handed or right-handed chirality with the exception of neutr-
⁵⁸⁰inos which can only have left-handed chirality within the SM framework. Fermions in the
⁵⁸¹ SM can be divided into left-handed doublets and right-handed singlets

$$\psi_L = \begin{pmatrix} \nu_e \\ e_L \end{pmatrix}, \begin{pmatrix} \nu_\mu \\ \mu_L \end{pmatrix}, \begin{pmatrix} \nu_\tau \\ \tau_L \end{pmatrix}, \begin{pmatrix} u_L \\ d_L \end{pmatrix}, \begin{pmatrix} c_L \\ s_L \end{pmatrix}, \begin{pmatrix} t_L \\ b_L \end{pmatrix} \quad (2.5)$$

$$\psi_R = e_R, \mu_R, \tau_R, u_R, d_R, c_R, s_R, t_R, b_R.$$

⁵⁸² where g' is the B_μ coupling constant and $B_\mu(x)$ is a vector gauge field that transforms under
⁵⁸³ $U(1)_Y$ as

$$B_\mu \rightarrow B_\mu + \frac{1}{g'} \partial_\mu \theta(x). \quad (2.6)$$

⁵⁸⁴ Right-handed fermion singlets are not affected by $SU(2)_L$ transformation, so the fermion
⁵⁸⁵ fields ψ transform under $SU(2)_L$ as

$$\psi_L \rightarrow e^{iI_3\vec{\theta}(x)\cdot\vec{\sigma}/2}\psi_L \quad (2.7)$$

$$\psi_R \rightarrow \psi_R.$$

⁵⁸⁶ where $\vec{\sigma}/2$ are generators of $SU(2)_L$ with $\vec{\sigma}$ being the Pauli matrices. In order to preserve
⁵⁸⁷ local symmetry, the gauge covariant derivative for $SU(2)_L$ and $U(1)_Y$ can be defined [61] so

588 that the gauge covariant derivative for $SU(2)_L \times U(1)_Y$ can be written as

$$\begin{aligned} D_\mu \psi_L &= \left(\partial_\mu - ig' \frac{Y_L}{2} B_\mu - ig \frac{\sigma_i}{2} W_\mu^i \right) \psi_L \\ D_\mu \psi_R &= \left(\partial_\mu - ig' \frac{Y_R}{2} B_\mu \right) \psi_R. \end{aligned} \quad (2.8)$$

589 where $B_\mu(x)$ is a vector gauge field associated with $U(1)_Y$ and $W_\mu^i(x)$ ($i = 1, 2, 3$) are three
590 vector gauge fields associated with $SU(2)_L$. The B_μ and W_μ^i gauge fields transform under
591 their corresponding symmetry groups $U(1)_Y$ and $SU(2)_L$ as

$$\begin{aligned} B_\mu &\rightarrow B_\mu + \frac{1}{g'} \partial_\mu \theta(x) \\ W_\mu^i &\rightarrow W_\mu^i + \frac{2}{g} \partial_\mu \theta_a(x) + \epsilon^{ijk} \theta_j(x) W_\mu^k, \end{aligned} \quad (2.9)$$

592 where g' is the B_μ gauge coupling constant, g is the W_μ^i gauge coupling constants and ϵ^{ijk}
593 is the $SU(2)_L$ structure constant. Similar to section 2.1.2.1, the kinetic term is added by
594 defining field strengths for the four gauge fields

$$\begin{aligned} B_{\mu\nu} &\equiv \partial_\mu B_\nu - \partial_\nu B_\mu \\ W_{\mu\nu}^i &\equiv \partial_\mu W_\nu^i - \partial_\nu W_\mu^i - g e^{ijk} W_\mu^j W_\nu^k. \end{aligned} \quad (2.10)$$

595 The local $SU(2)_L \times U(1)_Y$ invariant EW Lagrangian [61] is then

$$\begin{aligned} \mathcal{L}_{\text{EW}} &= i \bar{\psi} (\gamma^\mu D_\mu) \psi - \frac{1}{4} W_{\mu\nu}^i W_i^{\mu\nu} - \frac{1}{4} B_{\mu\nu} B^{\mu\nu} \\ &= \underbrace{i \bar{\psi} (\gamma^\mu \partial_\mu) \psi}_{\text{fermion kinematics}} - \underbrace{\bar{\psi} \left(\gamma^\mu g' \frac{Y}{2} B_\mu \right) \psi}_{\text{fermion-gauge boson interaction}} - \underbrace{\bar{\psi}_L \left(\gamma^\mu g \frac{\sigma_i}{2} W_\mu^i \right) \psi_L}_{\text{boson kinematics \& self-interaction}} - \frac{1}{4} W_{\mu\nu}^i W_i^{\mu\nu} - \frac{1}{4} B_{\mu\nu} B^{\mu\nu}. \end{aligned} \quad (2.11)$$

596 Under ≈ 159.5 GeV, the EW symmetry $SU(2)_L \times U(1)_Y$ undergoes spontaneous symmetry
 597 breaking [62] into $U(1)_{\text{QED}}$ symmetry, which corresponds to a separation of the weak and
 598 electrodynamic forces. Electroweak spontaneous symmetry breaking replaces the four mass-
 599 less and similarly-behaved EW gauge bosons B_μ and W_μ^i with the EM boson γ and the weak
 600 bosons Z/W^\pm , as well as giving the Z and W^\pm bosons masses via the Higgs mechanism.
 601 This is due to a specific choice of gauge for the Higgs field leading to the reparameterization
 602 of the EW bosons B_μ and W_μ^i to $W^\pm/Z/\gamma$ using the relations

$$\begin{aligned}
 W_\mu^\pm &\equiv \frac{1}{\sqrt{2}} (W_\mu^1 \mp iW_\mu^2) \\
 \begin{pmatrix} A_\mu \\ Z_\mu \end{pmatrix} &\equiv \begin{pmatrix} \cos \theta_W & \sin \theta_W \\ -\sin \theta_W & \cos \theta_W \end{pmatrix} \begin{pmatrix} B_\mu \\ W_\mu^3 \end{pmatrix}
 \end{aligned} \tag{2.12}$$

603 where $\theta_W \equiv \cos^{-1} (g/\sqrt{g^2 + g'^2})$ is the weak mixing angle. The boson kinetic term can also
 604 be refactorized to extract cubic (three vertices) and quartic (four vertices) self-interactions
 605 among the gauge bosons [61]. The Lagrangian can then be rewritten as

$$\begin{aligned}
 \mathcal{L} = & \underbrace{eA_\mu \bar{\psi} (\gamma^\mu Q) \psi}_{\text{electromagnetism}} + \underbrace{\frac{e}{2 \sin \theta_W \cos \theta_W} \bar{\psi} \gamma^\mu (v_f - a_f \gamma_5) \psi Z_\mu}_{\text{neutral current interaction}} \\
 & + \underbrace{\frac{g}{2\sqrt{2}} \sum_{\psi_L} [\bar{f}_2 \gamma^\mu (1 - \gamma_5) f_1 W_\mu^+ + \bar{f}_1 \gamma^\mu (1 - \gamma_5) f_2 W_\mu^-]}_{\text{charged current interaction}} \\
 & + \underbrace{\mathcal{L}_{\text{kinetic}} + \mathcal{L}_{\text{cubic}} + \mathcal{L}_{\text{quartic}}}_{\text{boson self-interaction}}
 \end{aligned} \tag{2.13}$$

606 where $\gamma_5 = i\gamma^0\gamma^1\gamma^2\gamma^3$ is the chirality projection operator, $a_f = I_3$, $v_f = I_3(1 - 4|Q| \sin^2 \theta_W)$
 607 and f_1, f_2 are up and down type fermions of a left-handed doublet.

608 **2.1.2.3 Higgs mechanism**

609 So far, the EW bosons are massless since the mass terms $-m\bar{\psi}\psi$ for fermions and
 610 $-mA^\mu A_\mu$ for bosons are not invariant under the EW Lagrangian symmetries. The parti-
 611 cles must then acquire mass under another mechanism. The Brout-Engler-Higgs mechanism
 612 [11–13] was introduced in 1964 to rectify this issue and verified in 2012 with the discovery
 613 of the Higgs boson [20, 21].

614 The Higgs potential is expressed as

$$V(\phi^\dagger \phi) = \mu^2 \phi^\dagger \phi + \lambda (\phi^\dagger \phi)^2 \quad (2.14)$$

615 where μ^2 and $\lambda > 0$ are arbitrary parameters, and the $SU(2)_L$ doublet $\phi = \begin{pmatrix} \phi^+ \\ \phi^0 \end{pmatrix}$ is the Higgs
 616 field with complex scalar fields ϕ^+ and ϕ^0 carrying +1 and 0 electric charge respectively.

617 The Lagrangian for the scalar Higgs field is

$$\mathcal{L}_H = (\partial_\mu \phi)^\dagger (\partial^\mu \phi) - V(\phi^\dagger \phi). \quad (2.15)$$

618 Since the potential $V(\phi^\dagger \phi)$ is constrained by $\lambda > 0$, the ground state is solely controlled by
 619 μ . If $\mu^2 > 0$, the ground state energy is $\phi = 0$, and the EW bosons would remain massless.
 620 If $\mu^2 < 0$, the ground state is

$$|\phi|^2 = -\frac{\mu^2}{2\lambda} \equiv \frac{v^2}{\sqrt{2}}, \quad (2.16)$$

621 where v is defined as the vacuum expectation value (VEV). The standard ground state for
 622 the Higgs potential without loss of generality can be chosen as $\phi(0) = 1/\sqrt{2}(0)_v$.

623 Having $U(1)$ symmetry allows any $-e^{i\theta} \sqrt{\mu^2/\lambda}$ to be a ground state energy for the Higgs

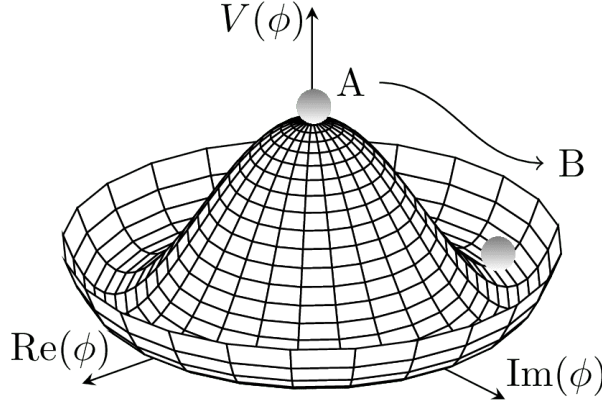


Figure 2.3: Illustration of a common representation of the Higgs potential [63]. Before SSB, the ground state $\phi(0)$ is located at A which is symmetric with respect to the potential. A perturbation to this state fixes the ground state energy $|\phi(0)|^2$ to a particular value at B, "spontaneously" breaking the symmetry and degeneracy in $|\phi(0)|^2$.

624 Lagrangian. This degeneracy results in spontaneous symmetry breaking of the $SU(2)_L \times$
 625 $U(1)_Y$ symmetry into $U(1)_{\text{EM}}$ symmetry when the Higgs field settles on a specific vacuum
 626 state as a result of a perturbation or excitation (Figure 2.3). The spontaneous symmetry
 627 breaking introduces three massless (Nambu-Goldstone [64]) vector gauge boson ξ and a
 628 massive scalar boson η , each corresponds to a generator of the gauge group. The vector field
 629 for ξ and η are real fields parameterized as $\xi \equiv \phi^+ \sqrt{2}$ and $\eta \equiv \phi^0 \sqrt{2} - v$ [65]. The Higgs
 630 field now becomes

$$\phi = \frac{v + \eta + i\xi}{\sqrt{2}} = \frac{1}{\sqrt{2}} e^{i\xi} \begin{pmatrix} 0 \\ v + \eta \end{pmatrix}. \quad (2.17)$$

631 Due to $U(1)_{\text{EM}}$ invariance, a unitary gauge with the transformation $\phi \rightarrow \exp(-i\xi \cdot) \frac{\sigma}{2v}$ can
 632 be chosen for the Higgs field to eliminate the massless bosons and incorporate them into the
 633 EM/weak bosons via Equation 2.12. This leaves the massive η which can now be observed as
 634 an excitation of the Higgs field from the standard ground state and must be the Higgs boson
 635 h . Using the EW covariant derivative from Equation 2.8, the Higgs Lagrangian around the

636 vacuum state becomes

$$\begin{aligned}\mathcal{L}_H &= (D_\mu \phi)^\dagger (D^\mu \phi) - \mu^2 \left(\frac{v+h}{\sqrt{2}} \right)^2 - \lambda \left(\frac{v+h}{\sqrt{2}} \right)^4 \\ &= (D_\mu \phi)^\dagger (D^\mu \phi) - \frac{1}{2} \mu^2 h^2 - \lambda v h^3 - \frac{\lambda}{4} h^4 - \dots\end{aligned}\tag{2.18}$$

637 The Higgs mass can be extracted from the quadratic term as $m_H = \sqrt{-2\mu^2}$. The kinetic

638 term in the Lagrangian can be written as

$$\begin{aligned}(D_\mu \phi)^\dagger (D^\mu \phi) &= \frac{1}{2} (\partial_\mu h)^2 + \frac{g^2}{8} (v+h)^2 \left| W_\mu^1 - i W_\mu^2 \right|^2 + \frac{1}{8} (v+h)^2 (g' W_\mu - g B_\mu) \\ &= \frac{1}{2} (\partial_\mu h)^2 + (v+h)^2 \left(\frac{g^2}{4} W_\mu^+ W^{-\mu} + \frac{1}{8} (g^2 + g'^2) Z_\mu^0 Z^{0\mu} \right).\end{aligned}\tag{2.19}$$

639 Masses for the EW bosons can be extracted from the quadratic terms

$$m_{W^\pm} = \frac{v}{2} g, \quad m_Z = \frac{v}{2} \sqrt{g^2 + g'^2}, \quad m_\gamma = 0.\tag{2.20}$$

640 However, the fermion mass term $-m\bar{\psi}\psi$ still breaks EW invariance after spontaneous sym-

641 metry breaking. Instead, fermions acquire mass by replacing the mass term with a gauge

642 invariant Yukawa term in the EW Lagrangian representing fermions' interactions with the

643 Higgs field [65]

$$\begin{aligned}\mathcal{L}_{\text{Yukawa}} &= -c_f \frac{v+h}{\sqrt{2}} (\bar{\psi}_R \psi_L + \bar{\psi}_L \psi_R) \\ &= -\underbrace{\frac{c_f}{\sqrt{2}} v (\bar{\psi} \psi)}_{\text{fermion mass}} - \underbrace{\frac{c_f}{\sqrt{2}} (h \bar{\psi} \psi)}_{\text{fermion-Higgs interaction}},\end{aligned}\tag{2.21}$$

644 where c_f is the fermion-Higgs Yukawa coupling. The fermion mass is then $m_f = c_f v / \sqrt{2}$.

645 2.2 Beyond the Standard Model: $t\bar{t}Z' \rightarrow t\bar{t}t\bar{t}$

646 This analysis uses the $t\bar{t}t\bar{t}$ final state signal signature to search for the existence of a
647 heavy neutral BSM resonance that couples strongly to the top quark, nominally named
648 Z' . The cross-section for $t\bar{t}t\bar{t}$ production at the LHC can be enhanced by many possible
649 BSM models, in particular production of heavy scalars and pseudoscalar bosons predicted in
650 Type-II two-Higgs-doublet models (2HDM) [39–43] or possible production of a heavy neutral
651 resonance boson $Z'(\rightarrow t\bar{t})$ in association with a $t\bar{t}$ pair [66, 67]. The $t\bar{t}Z'$ production mode
652 and consequently $t\bar{t}t\bar{t}$ signal signature can provide a more sensitive channel for searches by
653 avoiding contamination from the large SM $gg \rightarrow t\bar{t}$ background in an inclusive $Z' \rightarrow t\bar{t}$
654 search.

655 2.2.1 Top-philic vector resonance

656 Many BSM models extend the SM by adding to the SM gauge group additional $U(1)'$
657 gauge symmetries [68, 69], each with an associated vector gauge boson (Z'). In the case of
658 a BSM global symmetry group with rank larger than the SM gauge group, the symmetry
659 group can spontaneously break into $G_{\text{SM}} \times U(1)'^n$, where G_{SM} is the SM gauge group
660 $SU(3)_C \times SU(2)_L \times U(1)_Y$ and $U(1)'^n$ is any $n \geq 1$ number of $U(1)'$ symmetries. The
661 existence of additional vector boson(s) Z' would open up many avenues of new physics e.g.
662 extended Higgs sectors from $U(1)'$ symmetry breaking [70, 71] and possible new particles as
663 heavy Z' decay products [73].

664 Due to the top quark having the largest mass out of all known elementary particles in the
665 SM, many BSM models [38–43, 74, 75] predict 'top-philic' vector resonances that have much
666 stronger coupling to the top quark compared to other quarks. Previous BSM $t\bar{t}t\bar{t}$ search at

667 the LHC for top-philic resonances [28] with a similar model in the single-lepton final state
 668 and similar mass ranges set upper limits on observed (expected) Z' production cross section
 669 between 21 (14) fb to 119 (86) fb depending on parameter choice. This analysis is also moti-
 670 vated by the recent observation of SM $t\bar{t}t\bar{t}$ production in the same-sign multilepton (SSML)
 671 channel by ATLAS [44] and CMS [76] at 6.1σ and 5.6σ discovery significance respectively.

672 A simplified top-philic color-singlet vector particle model [45, 74] is employed in the
 673 search. The interaction Lagrangian assumes the Z' couples dominantly the top quark and
 674 has the form

$$\begin{aligned}
 \mathcal{L}_{Z'} &= \bar{t}\gamma_\mu (c_L P_L + c_R P_R) t Z'^\mu \\
 &= c_t \bar{t}\gamma_\mu (\cos\theta P_L + \sin\theta P_R) t Z'^\mu,
 \end{aligned} \tag{2.22}$$

675 where $c_t = \sqrt{c_L^2 + c_R^2}$ is the Z' -top coupling strength, $P_{L/R} = (1 \mp \gamma_5)/2$ are the chirality
 676 projection operators, and $\theta = \tan^{-1}(c_R/c_L)$ is the chirality mixing angle. Expanding the
 677 Lagrangian results in

$$\mathcal{L}_{Z'} = \frac{1}{\sqrt{2}} \bar{t}\gamma_\mu \left[\sin\left(\theta + \frac{\pi}{4}\right) - \left(\sqrt{2} \cos\left(\theta + \frac{\pi}{4}\right) \right) \gamma_5 \right] t Z'^\mu, \tag{2.23}$$

678 which bears striking resemblance to the EW Lagrangian neutral current interaction term in
 679 Equation 2.13, showing the similarity between the Z' and the Z boson that acquires mass
 680 from $SU(2)_L \times U(1)_Y$ spontaneous symmetry breaking. Assuming the Z' mass $m_{Z'}$ is much
 681 larger than the top mass ($m_t^2/m_{Z'}^2 \approx 0$), the Z' decay width at leading-order (LO) can be
 682 approximated as

$$\Gamma(Z' \rightarrow t\bar{t}) \approx \frac{c_t^2 m_{Z'}}{8\pi}. \tag{2.24}$$

683 It can be observed that $\Gamma/m_{Z'} \approx c_t^2/8\pi \ll 1$ for $c_t \approx 1$, which suggests a very narrow and

684 well-defined resonance peak, validating the narrow-width approximation for the choice of

685 $c_t = 1$.

686 2.2.2 Production channels

687 The main production channels at the LHC proton-proton collider for the aforementioned
688 heavy topophilic color singlet Z' are at tree level and loop level, with the one-loop level being
689 the dominant processes [45]. Loop level processes are dependent on the chirality angle θ ,
690 where $\theta = \pi/4$ suppresses all but gluon-initiated box sub-processes. To minimize model
691 dependence, only the tree level production was considered for this analysis by choosing
692 $\theta = \pi/4$. Figure 2.4 illustrates several tree level Z' production processes.

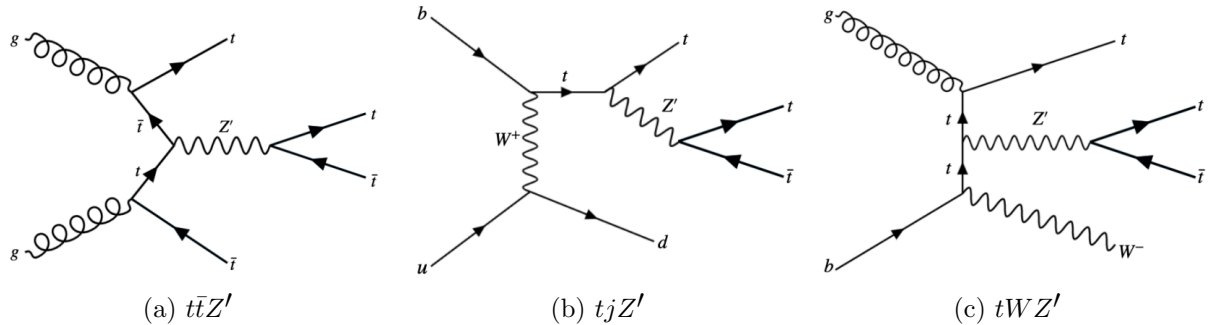


Figure 2.4: Feynman diagrams for tree level Z' production in association with (a) $t\bar{t}$, (b) tj (light quark) and (c) tW , decaying to final states containing (a) $t\bar{t}t\bar{t}$ or (b)(c) $t\bar{t}t$ [45].

693 The tree level $t\bar{t}$ -associated process $t\bar{t}Z'$ is the targeted production channel for the search
694 in this dissertation. The $t\bar{t}Z'$ cross-section at LO in QCD is shown in Figure 2.5. Con-
695 tributions from the single-top-associated channels tjZ' and tWZ' are not considered due
696 to a smaller cross-section by a factor of two compared to $t\bar{t}Z'$ due to suppression in the
697 three-body phase space [45]. Additionally, $t\bar{t}Z' \rightarrow t\bar{t}t\bar{t}$ production is independent of θ while
698 tjZ' and tWZ' are minimally suppressed under pure left-handed interactions ($\theta = 0$) and
699 maximally suppressed under pure right-handed interactions ($\theta = \pi/2$); both channels are

700 affected by the choice of $\theta = \pi/4$ to suppress loop level production.

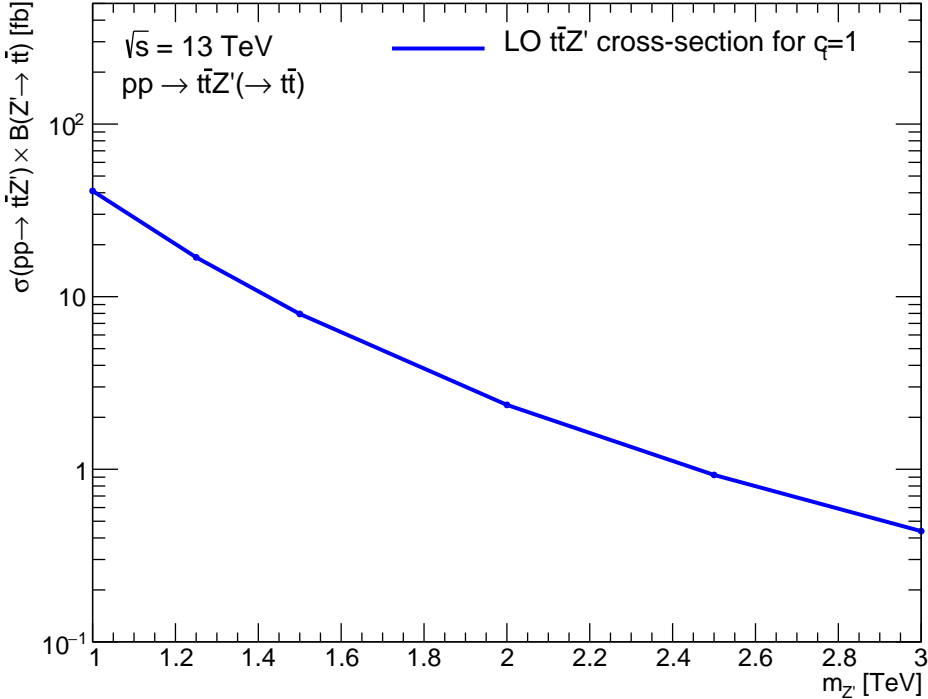


Figure 2.5: Theoretical $t\bar{t}Z'$ production cross-section times $Z' \rightarrow t\bar{t}$ branching ratio as a function of the Z' mass at LO in QCD coupling to top with $c_t = 1$ under a simplified topophilic model [45, 74, 77].

701 2.2.3 Decay modes

702 The different W boson decay modes shown in Figure 2.2 result in many different final
 703 states for $t\bar{t}Z'/t\bar{t}t\bar{t}$ decay, which can each be classified into one of three channels shown in
 704 Figure 2.6: all hadronic decays; exactly one lepton or two opposite-sign leptons (1LOS);
 705 exactly two same-sign leptons or three or more leptons (SSML). The branching ratio for
 706 each channel is shown in Figure 2.6. The all hadronic and 1LOS channels have much larger
 707 branching ratios compared to SSML channel but suffer heavily from $gg \rightarrow t\bar{t}$ background
 708 contamination, giving the SSML channel better sensitivity at the cost of lower statistics.

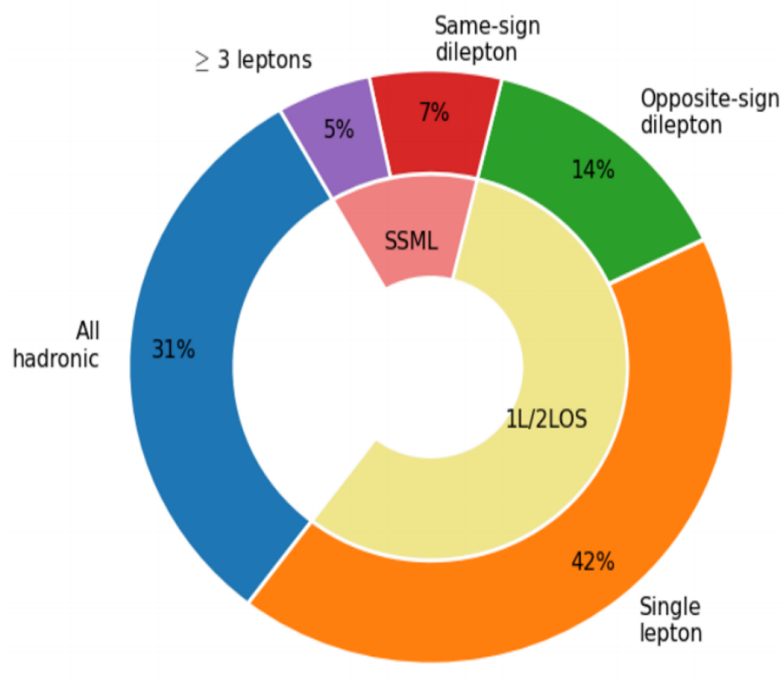


Figure 2.6: Branching ratios for $t\bar{t}t\bar{t}$ decay [78]. The same-sign dilepton and multilepton channels together forms the SSML channel.

⁷⁰⁹ This is also the targeted channel for this analysis.

710 Chapter 3. LHC & ATLAS Experiment

711 3.1 The Large Hadron Collider

712 Predictions from theoretical models are evaluated against experimental data collected
713 from particle detectors. This chapter provides a detailed overview of the Large Hadron
714 Collider (LHC) and the ATLAS detector, one of the key experiments designed to study
715 high-energy collisions at the LHC.

716 3.1.1 Overview

717 The Large Hadron Collider [79] (LHC) is currently the world's largest particle collider
718 with a circumference of almost 27 km. Built by CERN on the border of Switzerland and
719 France, the LHC is designed as a particle collider for proton-proton (pp), sometimes heavy
720 ions i.e. lead-lead (PbPb) and proton-lead (pPb) beams at TeV-scale energies. Two beams
721 of particles are injected into the LHC in opposite directions and allowed to collide at the
722 center of four major experiments:

- 723 • **A Toroidal LHC ApparatuS** (ATLAS) [27] and **Compact Muon Solenoid** (CMS)
724 [80]: multi-purpose detectors, designed to target a variety of phenomena including SM,
725 BSM and heavy-ion physics.
- 726 • **Large Ion Collider Experiment** (ALICE) [81]: specialized detector to record ion
727 collisions and study heavy-ion physics.
- 728 • **Large Hadron Collider beauty** (LHCb) [82]: detector dedicated to study properties
729 of b -quarks and b -hadrons.

730 Aside from the four major experiments, the LHC also houses smaller experiments e.g.
 731 AWAKE [83], FASER [84], KATRIN [85], that either share an interaction point with one of
 732 the above experiments or make use of particle beams pre-LHC injection.

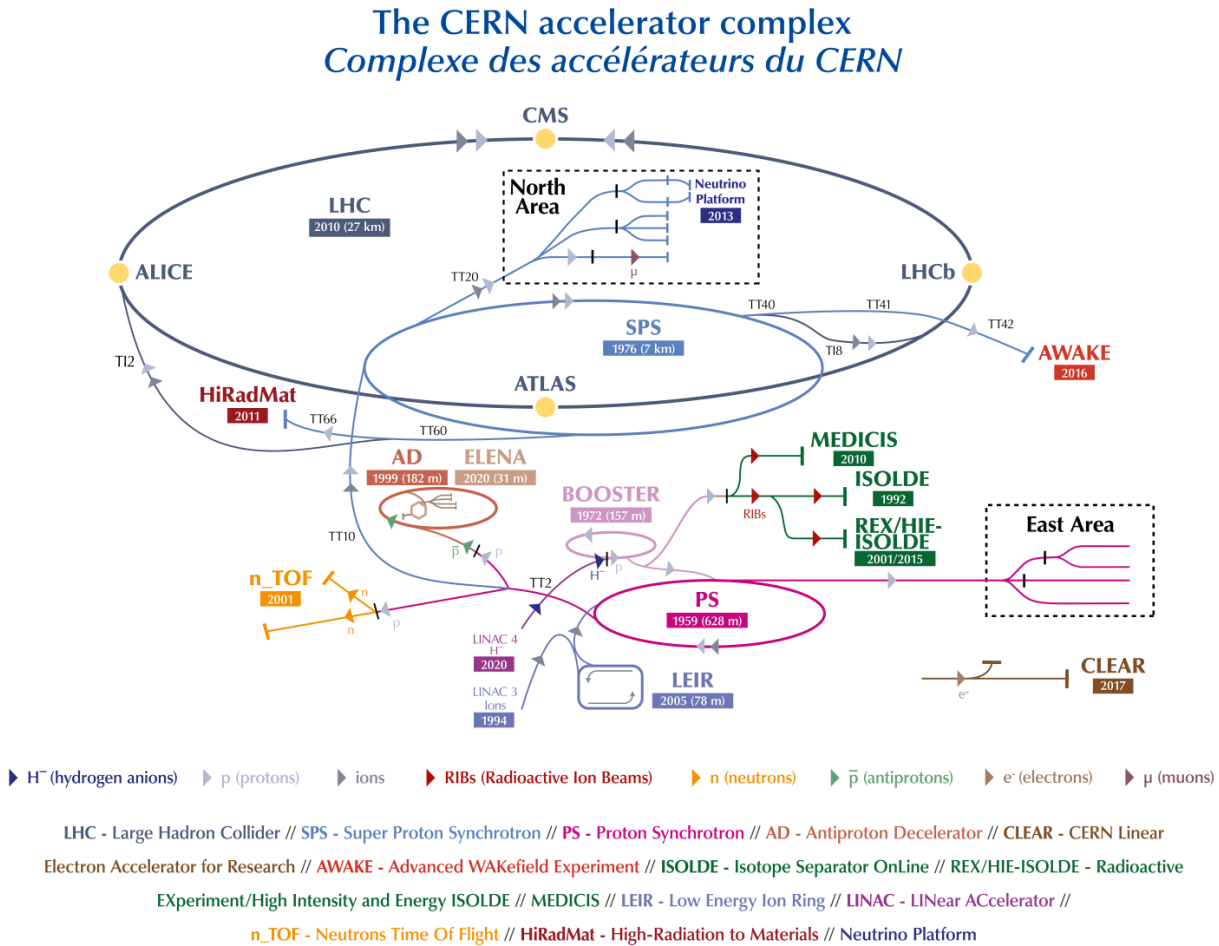


Figure 3.1: The full CERN accelerator complex as of 2022 [86].

733 The majority of the LHC operational time is dedicated to studying pp collisions of up to
 734 ~ 13 TeV center-of-mass energy, denoted as \sqrt{s} . Reaching collision energy requires a sequence
 735 of accelerators within the CERN accelerator complex, shown in Figure 3.1. Proton produc-
 736 tion starts at LINAC 4, where hydrogen atoms are accelerated to 160 MeV then stripped
 737 of electrons. The leftover proton beams are injected into the Proton Synchrotron Booster

738 (PSB) and accelerated to 2 GeV before being transferred into the Proton Synchrotron (PS).
 739 Here, the beams are ramped up to 26 GeV then injected into the Super Proton Synchrotron
 740 (SPS) to further raise the energy threshold to 450 GeV. The beams are finally injected into
 741 the LHC in opposite directions, continuously increasing in energy up to 6.5 TeV per beam,
 742 reaching the 13 TeV center-of-mass energy threshold necessary for collision during Run 2.
 743 As of the start of Run 3 in 2022, proton beams can now be ramped up to 6.8 TeV per beam
 744 for a total of $\sqrt{s} = 13.6$ TeV.

745 3.1.2 LHC operations

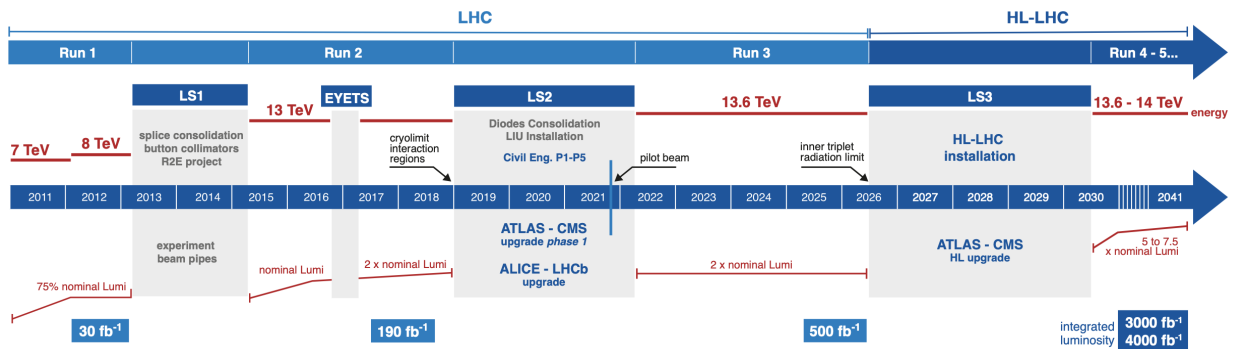


Figure 3.2: Current and future timeline of LHC operations with corresponding center-of-mass energies and projected integrated luminosities. [87].

746 Operations at the LHC are defined in periods of data-taking and shut-down known as
 747 runs and long shutdowns respectively; the first period (Run 1) started with first collisions
 748 at the LHC in 2010 at $\sqrt{s} = 7$ TeV [88]. Upgrades are usually carried out for detectors and
 749 accelerators during long shutdowns, raising the maximum energy threshold in preparation
 750 for the next run. An overview of the LHC runtime and corresponding center-of-mass energies
 751 are summarized in Figure 3.2. During Run 2 from 2015-2018, the ATLAS detector recorded
 752 a total of 1.1×10^{16} pp collisions at $\sqrt{s} = 13$ TeV, which corresponds to an integrated

753 luminosity of $140 \pm 0.83\% \text{ fb}^{-1}$ that passed data quality control and are usable for analyses
754 [89]. This is also the data set used for the analysis in this dissertation.

755 3.1.3 Physics at the LHC

756 The majority of physics studied at the LHC focus primarily on QCD proton-proton hard
757 scattering processes and the resulting products. Hard scattering processes involve large
758 momentum transfer compared to the proton mass e.g. top pair production ($gg \rightarrow t\bar{t}$) and
759 Higgs production ($gg \rightarrow H$), and can be predicted using perturbative QCD [90]. Hard
760 processes probe distance scales much lower than the proton radius and can be considered
761 collisions between the constituent quarks and gluons i.e. partons. Soft processes involve
762 lower momentum transfer between partons and are dominated by less well-understood non-
763 perturbative QCD effects. The hard interaction between two partons are represented by a
764 parton distribution function (PDF) $f_i(x, Q^2)$, which describes the probability of interacting
765 with a constituent parton i that carries a fraction x of the external hadron's momentum
766 when probed at a momentum scale of Q^2 [91]. Other partons within the hadron that did
767 not participate in the collision can still interact via lower momentum underlying-events
768 (UE). The probability of a particular interaction occurring is defined as its cross-section
769 $\sigma[b]$. Figure 3.3 gives an overview of SM processes produced within the LHC and their
770 cross-sections.

771 3.2 The ATLAS detector

772 One of the four main experiments at the LHC is ATLAS [27], designed as a multi-purpose
773 detector for the role of studying high-energy physics in pp and heavy-ion collisions. ATLAS

Standard Model Production Cross Section Measurements

Status: October 2023

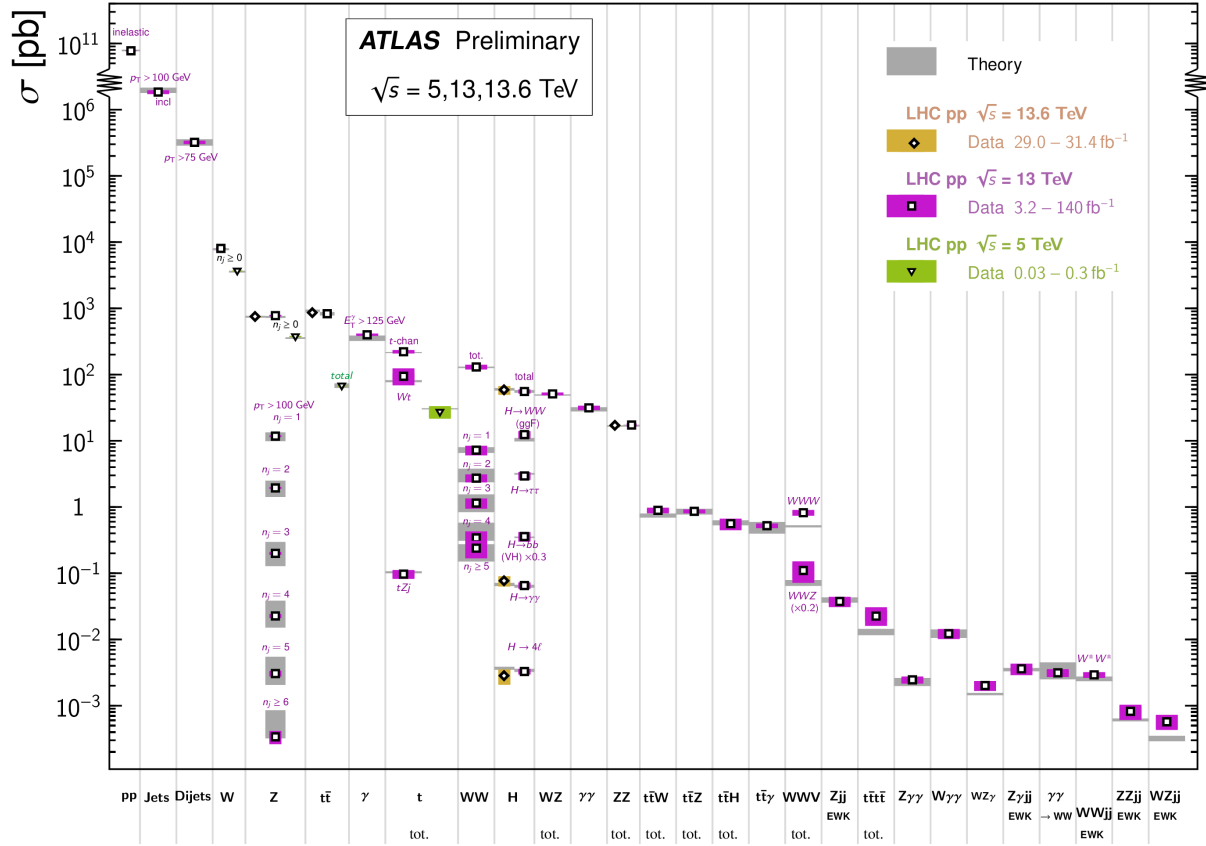


Figure 3.3: Summary of predicted and measured cross-section for SM processes at the LHC at different center-of-mass energies [92].

774 is a detector with symmetric cylindrical geometry with dimensions of 44 m in length and 25
 775 m in diameter, covering a solid angle of almost 4π around the collision point. The detector is
 776 built concentrically around the beamline with the collision point at the center to maximally
 777 capture signals produced by interactions. Figure 3.4 shows a slice of the ATLAS detector.
 778 From the inside out, the main ATLAS subdetector system consists of the inner detector
 779 (ID), calorimeter systems (electromagnetic and hadronic) and the muon spectrometer (MS).
 780 The ATLAS detector uses a right-handed coordinate system [27] designed to align with
 781 the geometry of a collision interaction, with the origin set at the interaction point, the z -axis

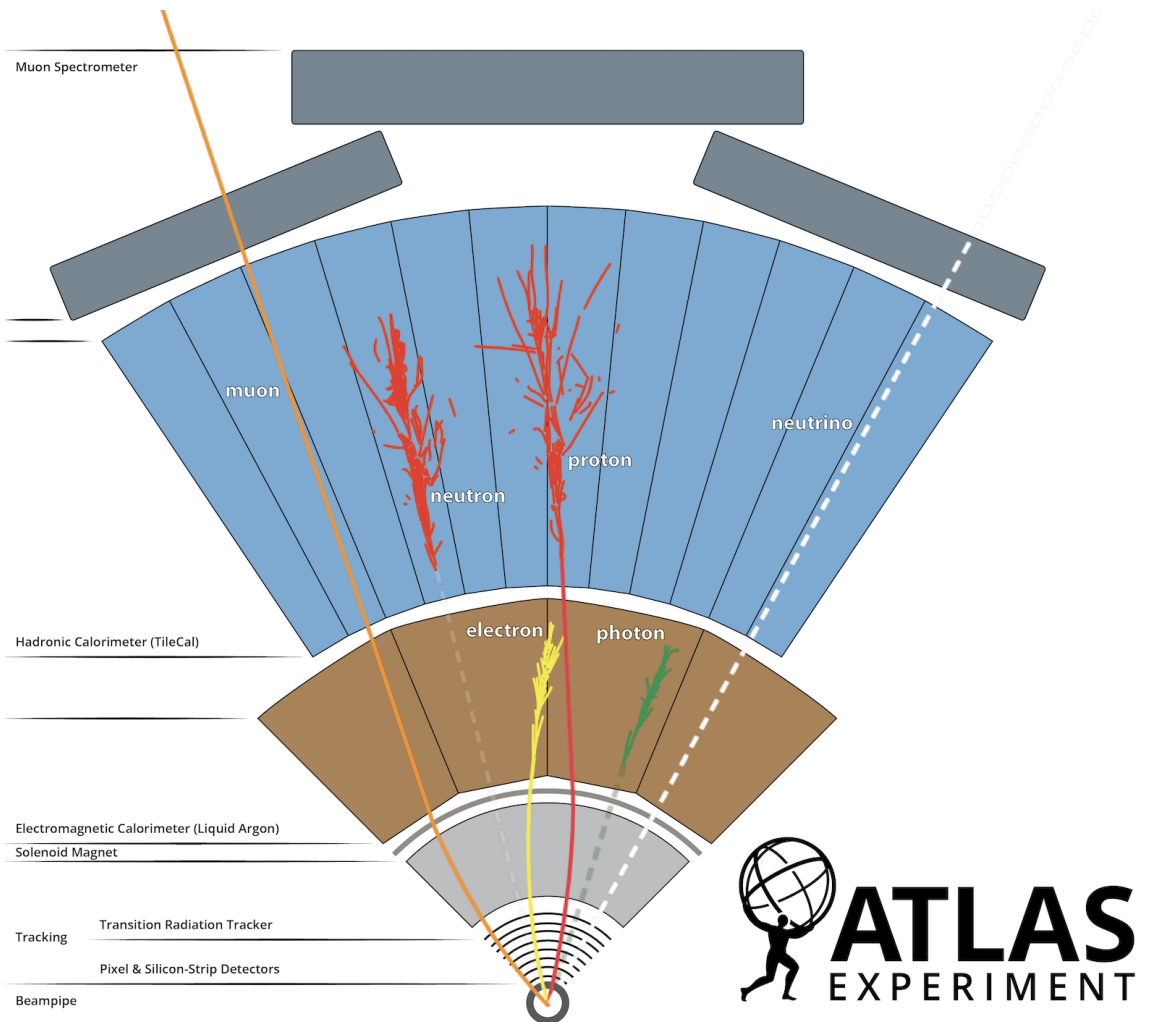


Figure 3.4: A cross section slice of the ATLAS detector showing different subsystems along with visualization of different types of particles traveling through the detector [93].

following (either of) the beamline and the x -axis pointing towards the center of the LHC ring. In cylindrical coordinates, the polar angle θ is measured from the beam axis, and the azimuthal angle ϕ is measured along the transverse plane (xy -plane) starting at the x -axis. Additional observables are defined for physics purposes: the pseudorapidity defined as $\eta = -\ln \tan(\theta/2)$; angular distance within the detector defined as $\Delta R = \sqrt{\Delta\eta^2 + \Delta\phi^2}$; and transverse momentum p_T (transverse energy E_T) defined as the component of the particle's momentum (energy) projected onto the transverse plane.

789 3.2.1 Inner detector

790 The innermost part of ATLAS is the inner detector (ID) [27], constructed primarily for
791 the purpose of measuring and reconstructing charged tracks within the $|\eta| < 2.5$ region with
792 high momentum resolution ($\sigma_{p_T}/p_T = 0.05\% \pm 1\%$). Figure 3.5 shows the composition of
793 the ID with three subsystems, the innermost being the pixel detector, then Semiconductor
794 Tracker (SCT), and the Transition Radiation Tracker (TRT) on the outermost layer; all of
795 which are surrounded by a solenoid magnet providing a magnetic field of 2 T.

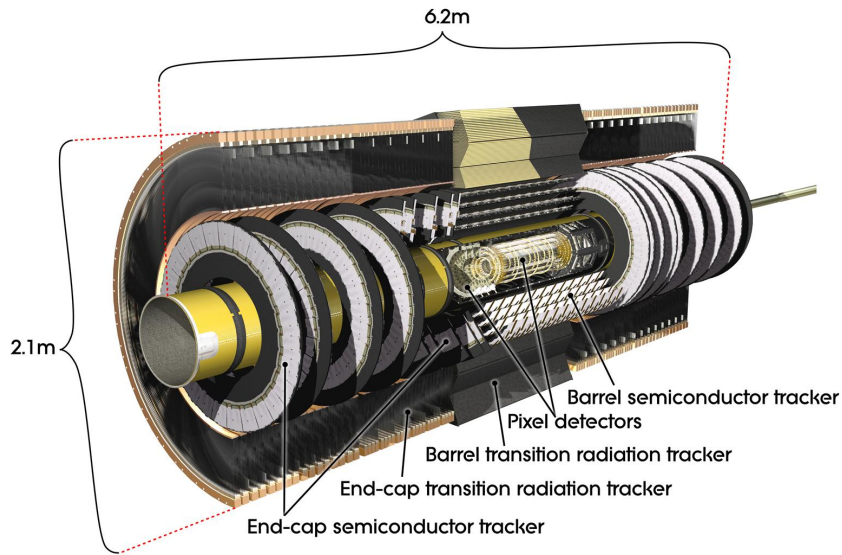


Figure 3.5: Cutaway illustration of the inner detector along with its subsystems [94].

796 Pixel detector

797 The pixel detector subsystem [27] consists of 250 μm silicon semiconductor pixel layers
798 with about 80.4 million readout channels, reaching a spatial resolution of 10 μm in the
799 $R - \phi$ (transverse) plane and 115 μm in the z -direction for charged tracks. Charged particles
800 passing through the pixel detector ionize the silicon layers and produce electron-hole pairs;

801 the electrons drift towards the detector's electrode under an applied electric field and the
802 resulting electric signals are collected in read-out regions. The pixel detector is used primarily
803 for impact parameter measurement, pile-up suppression, vertex finding and seeding for track
804 reconstruction.

805 Semiconductor Tracker

806 The Semiconductor Tracker (SCT) [27] functions similarly to the pixel detector, using
807 silicon semiconductor microstrips totaling about 6.3 million read-out channels, reaching a
808 per layer resolution of 17 μm in the $R\text{-}\phi$ plane and 580 μm in the z -direction [27]. The
809 SCT plays an important role in precise p_{T} measurement of charged particles as well as track
810 reconstruction.

811 Transition Radiation Tracker

812 The outermost layer of the ID, the Transition Radiation Tracker (TRT) [27], consists of
813 layers of 4 mm diameter straw tubes filled with a xenon-based gas mixture and a 30 μm
814 gold-plated wire in the center. The TRT contains a total of about 351 thousand readout
815 channels with a resolution of 130 μm for each straw tube in the $R\text{-}\phi$ plane, and provides
816 extended track measurement, particularly estimation of track curvature under the solenoidal
817 magnetic field. Importantly, the TRT also serves to identify electrons through absorption of
818 emitted transition-radiation within the Xe-based gas mixture.

819 3.2.2 Calorimeter systems

820 Surrounding the ID is the ATLAS calorimeter system [27] with electromagnetic (EM) and
821 hadronic calorimeters, covering a range of $|\eta| < 4.9$. The calorimeters are sampling calorime-

822 ters with alternating absorbing layers to stop incoming particles and active layers to collect
 823 read-out signals from energy deposits. Incoming particles passing through the calorimeters
 824 interact with the absorbing layers, producing EM or hadronic showers of secondary particles.
 825 The particle showers deposit energy in the corresponding layer of the calorimeters, which
 826 are collected and aggregated to identify and reconstruct the original particle's energy and
 827 direction. Figure 3.6 shows a schematic overview of the ATLAS calorimeter system.

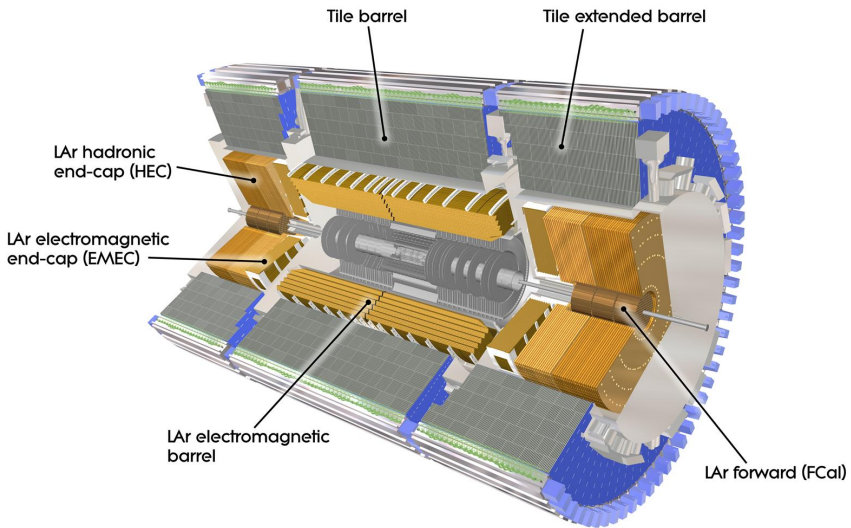


Figure 3.6: Cutaway illustration of the calorimeter system including the EM, hadronic and LAr forward calorimeters [95].

828 Electromagnetic calorimeter

829 The EM calorimeter [27] covers the innermost part of the calorimeter system, with lead
 830 (Pb) absorbing layers and liquid argon (LAr) active layers to capture the majority of electrons
 831 and photons exiting the ID. The EM calorimeter is divided into regions depending on η
 832 coverage: a barrel region ($|\eta| < 1.475$), two endcap regions ($1.375 < |\eta| < 3.2$) and a
 833 transition region ($1.372 < |\eta| < 1.52$). The endcap calorimeters are further divided into an

834 outer wheel region ($1.372 < |\eta| < 2.5$) and an inner wheel region ($2.5 < |\eta| < 3.2$) in order
835 to provide precise coverage within the same η range as the ID. Overlap between the barrel
836 and endcap regions compensates for the lower material density in the transition region.

837 Hadronic calorimeter

838 The hadronic calorimeter [27] covers up to $|\eta| < 4.9$ and is comprised of three parts: the
839 tile calorimeter with a barrel region ($|\eta| < 1.0$) and extended barrel regions ($0.8 < |\eta| < 1.7$);
840 the hadronic endcap calorimeter (HEC) covering $1.5 < |\eta| < 3.2$; and the forward calorimeter
841 (FCal) covering $3.2 < |\eta| < 4.9$. The tile calorimeter covers the EM calorimeter barrel region
842 and uses steel as material for the absorbing layers with scintillating tiles for the active layers.
843 Signals captured by scintillating tiles are read out from both sides using photomultiplier
844 tubes. The HEC calorimeter covers the endcap regions of the EM calorimeter and uses a
845 copper-LAr calorimeter layer scheme. The FCal is located close to the beamline providing
846 coverage for particles traveling close to parallel with the beam axis. The subdetector contains
847 three modules: one with copper absorbing layers optimized for EM measurements, and two
848 with tungsten absorbing layers targeting hadronic cascades. All modules in the FCal use
849 LAr as the active layer.

850 3.2.3 Muon spectrometer

851 Generally, the only particles that penetrate past the calorimeter layer are muons and
852 neutrinos. The muon spectrometer (MS) [27] is situated on the outermost of the ATLAS
853 detector and aims to track and measure muons within $|\eta| < 2.7$. The MS utilizes an array
854 of toroid magnets to provide a magnetic field perpendicular to the muon trajectory, bending
855 the track in order to measure its curvature. The magnetic field is powered by a large barrel

856 toroid ($|\eta| < 1.4$) with strength of 0.5 T and two endcap toroid magnets ($1.6 < |\eta| < 2.7$) of
857 1 T. Both types contribute to the magnetic field in the transition region ($1.4 < |\eta| < 1.6$).

858 To measure the muon itself, four types of large gas-filled chambers known as muon cham-
859 bers [27] are designed and constructed for two main goals: triggering on potential muon
860 candidates entering the MS and tracking their trajectories through the detector with high
861 precision. The tracking system include Monitored Drift Tubes (MDTs), which record muon
862 track information over the entire MS η range ($|\eta| < 2.7$). The MDTs are built with multi-
863 ple layers of drift tubes and filled with a mixture of 93% Ar and 7% CO₂. Muons passing
864 through drift tubes in the MDT ionize the gas within each tube; signals are then recorded
865 as freed electrons drift to read-out channels under an applied electric field. In the forward
866 region ($2.0 < |\eta| < 2.7$), Cathode Strip Chambers (CSCs) are included along with MDTs.
867 The CSCs are multiwire proportional chambers built with higher granularity and shorter
868 drift time than the MDTs to handle tracking in an environment with high background rates.

869 The MS trigger system includes Resistive Plate Chambers (RPCs) [27], which provide
870 triggering in the barrel region ($|\eta| < 1.05$) using parallel electrode plates made of resistive
871 materials with a gas mixture inbetween. High voltage is applied to the plates, accelerat-
872 ing the electrons freed from ionized gas and creating a fast avalanche of charge, which is
873 collected on external read-out strips almost instantaneously. Triggering and coarse position
874 measurements in the endcap region ($1.05 < |\eta| < 2.5$) is handled by Thin-Gap Chambers
875 (TGCs). Similar to CSCs, TGCs are multiwire proportional chambers with a small wire gap
876 ("thin-gap") and high applied voltage across the gap, resulting in fast response time giving
877 TGCs the capabilities to identify muon candidates in real time.

878 **3.2.4 Trigger & data acquisition**

879 The LHC produces a colossal amount of collision data at a bunch crossing rate of 40 MHz
880 with bunch spacing of 25 ns. The ATLAS Trigger and Data Acquisition (TDAQ) system [96]
881 synchronously identifies and records interesting events for in-depth analysis. The ATLAS
882 trigger system in Run 2 consists of two steps: Level-1 (L1) trigger and High-Level Trigger
883 (HLT). Events failing any step in the trigger chain are permanently lost.

884 The L1 trigger hardware is divided into L1 calorimeter triggers (L1Calo) and L1 muon
885 triggers (L1Muon) [96]. L1Calo trigger uses information from ATLAS calorimeter system
886 to quickly identify signs of high p_T objects e.g. EM clusters, jets and missing transverse
887 energy E_T^{miss} (section 4.4). Similarly, L1Muon uses information from the RPCs and TGCs
888 of the MS to make quick decisions on potentially interesting muon candidates. Outputs
889 from L1Calo and L1Muon are fed into the L1 topological trigger (L1Topo) for additional
890 filtering based on event topology and multi-object correlation, allowing for more selective
891 and physics-motivated triggering. Decisions from all three types of L1 triggers are provided
892 as inputs for the Central Trigger Processor (CTP) for a final Level-1 Accept (L1A) decision.

893 The entire L1 trigger chain results in a 2.5 μs latency and reduces the event rate to 100 kHz.

894 Events passing L1 triggers are sent to HLTs before being saved to offline storage at
895 CERN data centers. HLTs are software-based triggers used for more complex and specific
896 selections on physics objects required by targeted analysis goals, in turn requiring more
897 computing power with longer latency. After HLT selections, the event rate is reduced to 1
898 kHz on average [96]. Overall, the full trigger chain reduces the event rate for ATLAS by
899 approximately a factor of 4×10^4 .

900 Chapter 4. Particle Reconstruction & Identification

902 Activity within the ATLAS detector is recorded as raw electronic signals, which can
903 be utilized by ATLAS reconstruction software to derive physics objects for analysis. This
904 chapter describes the reconstruction and identification of basic objects (e.g. interaction
905 vertices, tracks, topological clusters of energy deposits) and subsequently of complex physics
906 objects i.e. particles and particle signatures.

907 4.1 Primary reconstruction

908 4.1.1 Tracks

909 Charged particles traveling through the ATLAS detector deposit energy in different layers
910 of the ID and MS. The ID track reconstruction software consists of two algorithm chains:
911 inside-out and outside-in track reconstruction [97–99].

912 The inside-out algorithm is primarily used for the reconstruction of primary particles
913 i.e. particles directly produced from pp collisions or decay products of short-lived particles.
914 The process starts by forming space points from seeded hits in the silicon detectors within
915 the pixel & SCT detectors. Hits further away from the interaction vertex are added to
916 the track candidate using a combinatorial Kalman filter [100] pattern recognition algorithm.
917 Track candidates are then fitted with a χ^2 filter [101] and loosely matched to a fixed-sized
918 EM cluster. Successfully matched track candidates are re-fitted with a Gaussian-sum filter
919 (GSF) [102], followed by a track scoring strategy to resolve fake tracks & hit ambiguity

920 between different tracks [103]. The track candidate is then extended to the TRT to form
921 final tracks satisfying $p_T > 400$ MeV. The outside-in algorithm handles secondary tracks
922 mainly produced from long-lives particles or decays of primary particles by back-tracking
923 from TRT segments, which are then extended inward to match silicon hits in the pixel and
924 SCT detectors to form track reconstruction objects.

925 4.1.2 Vertices

926 Vertices represent the point of interaction or decay for particles within the ATLAS de-
927 tector. Primary vertices (PVs) are defined as the point of collision for hard-scattering pp
928 interactions, while secondary or displaced vertices result from particle decays occurring at a
929 distance from its production point.

930 Reconstruction of PVs is crucial to accurately profile the kinematic information of an
931 event and form a basis for subsequent reconstruction procedures. Primary vertex recon-
932 struction occurs in two stages: vertex finding and vertex fitting [104]. The vertex finding
933 algorithm uses the spatial coordinates of reconstructed tracks to form the seed for a vertex
934 candidate. An adaptive vertex fitting algorithm [105] then iteratively evaluates track-vertex
935 compatibility to estimate a new best vertex position. Less compatible tracks are down-
936 weighted in each subsequent iteration, and incompatible tracks are removed and can be
937 used for another vertex seed; the process is repeated until no further PV can be found.
938 All reconstructed vertices without at least two matched tracks are considered invalid and
939 discarded.

940 Secondary vertex reconstruction uses the Secondary Vertex Finder (SVF) algorithm [106]
941 which is primarily designed to reconstruct b - and c -hadrons for flavor tagging purposes. The
942 SVF aims to reconstruct one secondary vertex per jet and only considers tracks that are

943 matched to a two-track vertex and contained within a p_T -dependent cone around the jet
944 axis. The tracks are then used to reconstruct a secondary vertex candidate using an iterative
945 process similar to the PV vertex fitting procedure.

946 **Pile-up**

947 At high luminosities, multiple interactions can be associated with one bunch crossing,
948 resulting in many PVs. The effect is called pile-up [107], and usually result from soft QCD
949 interactions. Pile-up can be categorized into two types: in-time pile-up, stemming from
950 additional pp collisions in the same bunch crossing that is not the hard-scatter process; out-
951 of-time pile-up, resulting from leftover energy deposits in the calorimeters from other bunch
952 crossings.

953 **4.1.3 Topological clusters**

954 Topological clusters (topo-clusters) [108] consist of clusters of spatially related calorimeter
955 cell signals. Topo-clusters are primarily used to reconstruct hadron- and jet-related objects
956 in an effort to extract signal while minimizing electronic effects and physical fluctuations, and
957 also allow for recovery of energy lost through bremsstrahlung or photon conversions. Cells
958 with signal-to-noise ratio $\zeta_{\text{cell}}^{\text{EM}}$ passing a primary seed threshold are seeded into a dynamic
959 topological cell clustering algorithm as part of a proto-cluster. Neighboring cells satisfying a
960 cluster growth threshold are collected into the proto-cluster. If a cell is matched to two proto-
961 clusters, the clusters are merged. Two or more local signal maxima in a cluster satisfying
962 $E_{\text{cell}}^{\text{EM}} > 500 \text{ MeV}$ suggest the presence of multiple particles in close proximity, and the cluster
963 is split accordingly to maintain good resolution of the energy flow. The process continues
964 iteratively until all cells with $\zeta_{\text{cell}}^{\text{EM}}$ above a principal cell filter level have been matched to a

965 cluster.

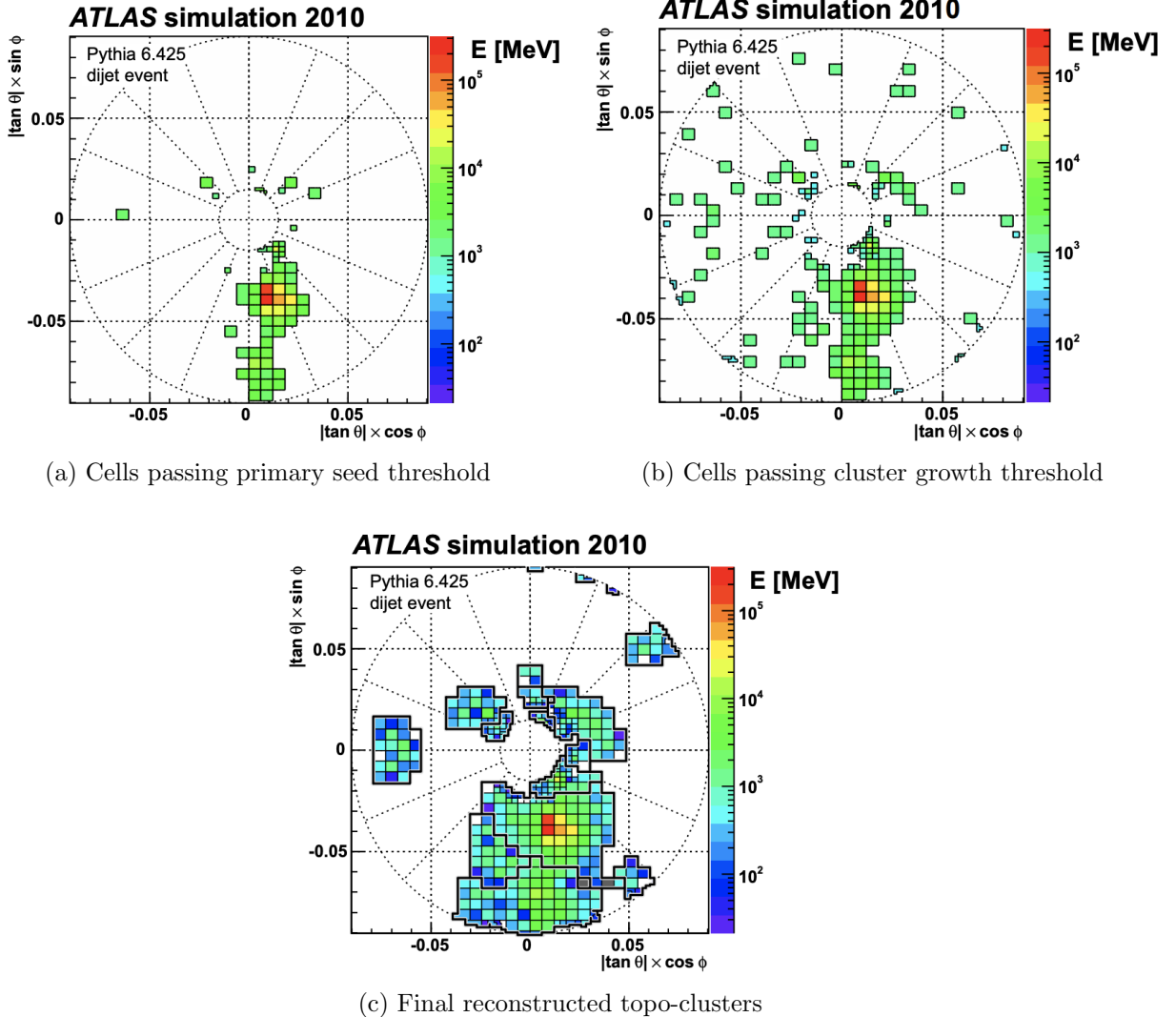


Figure 4.1: Stages of topo-cluster formation corresponding to each threshold. In (a), proto-clusters are seeded from cells with adequate signal significance ζ_{cell}^{EM} . The clusters are further merged and split in (b) following a predefined cluster growth threshold. The process stops in (c) when all sufficiently significant signal hits have been matched to a cluster [108].

966 4.2 Jets

967 Quarks, gluons and other hadrons with non-neutral color charge cannot be observed
 968 individually due to QCD color confinement, which forces a non-color-neutral hadron to

almost immediately undergo hadronization, producing a collimated cone of color-neutral hadrons defined as a jet. Jet signals can be used to reconstruct and indirectly observe the quarks or gluons from which the jet originated in the original hard-scattering process.

4.2.1 Jet reconstruction

The ATLAS jet reconstruction pipeline is largely carried out using a particle flow (PFlow) algorithm combined with an anti- k_t jet clustering algorithm. The PFlow algorithm [109] utilizes topo-clusters along with information from both the calorimeter systems and the ID in order to make use of the tracker system’s advantages in low-energy momentum resolution and angular resolution. First, the energy from charged particles is removed from the calorimeter topo-clusters; then, it is replaced by particle objects created using the remaining energy in the calorimeter and tracks matched to topo-clusters. The ensemble of ”particle flow objects” and corresponding matched tracks are used as inputs for the iterative anti- k_t algorithm [110].

The main components of the anti- k_t algorithm involve the distance d_{ij} between two jet candidates i and j , and the distance d_{iB} between the harder jet candidate of the two (defined as i) and the beamline B . If $d_{ij} < d_{iB}$, then the two jet candidates are combined and returned to the pool of candidates; otherwise, jet candidate i is considered a jet and removed from the pool. The distance d_{ij} is inversely proportional to a predefined radius parameter ΔR in order to control reconstruction quality for small- R and large- R jets. This analysis uses $\Delta R = 0.4$ to better handle heavily collimated small- R jets resulting from parton showers.

The anti- k_t jets so far have only been reconstructed at the EM level and need to be calibrated to match the energy scale of jets reconstructed at particle level. This is done via a MC-based jet energy scale (JES) calibration sequence, along with further calibrations

992 to account for pile-up effects and energy leakage. The full JES calibration sequence is
 993 shown in Figure 4.2. All calibrations except origin correction are applied to the jet's four-
 994 momentum i.e. jet p_T , energy and mass. Afterwards, a jet energy resolution (JER) [111]
 995 calibration step is carried out in a similar manner to JES to match the resolution of jets in
 996 dijet events. To further suppress pile-up effects, a neural-network based jet vertex tagger
 997 (NNJvt) discriminant was developed based on the previous jet vertex tagger (JVT) algorithm
 998 [107] and applied to low- p_T reconstructed jets.

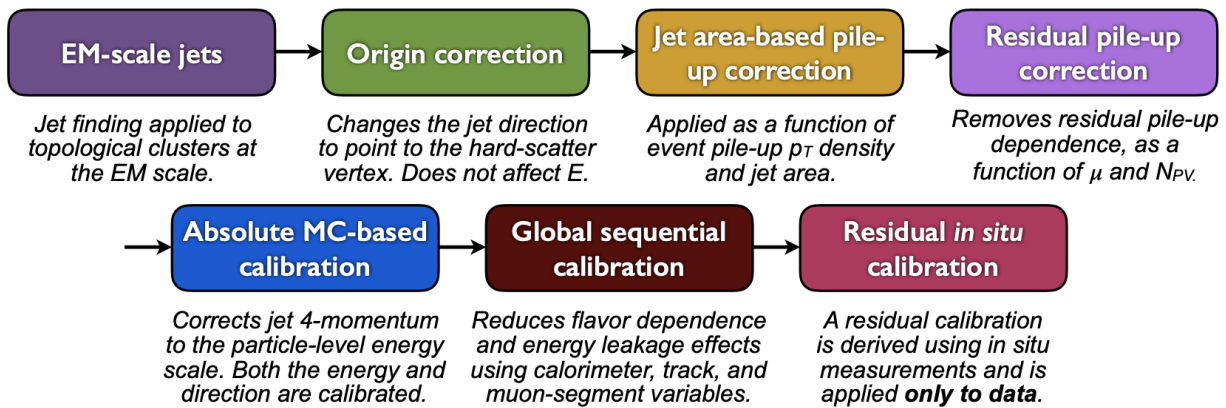


Figure 4.2: Jet energy scale calibration sequence for EM-scale jets [112].

999 4.2.2 Flavor tagging

1000 Identifying and classifying hadronic jets are important tasks for ATLAS physics, for
 1001 example analyses involving Higgs decays $H \rightarrow b\bar{b}$ or top quarks. Flavor tagging or b -tagging
 1002 is the process of identifying jets containing b -hadrons, c -hadrons, light-hadrons (uds -hadrons)
 1003 or jets from hadronically decaying τ leptons. Distinguishing b -jets is possible due to their
 1004 characteristically long lifetime ($\tau \approx 1.5$ ps), displaced secondary decay vertex and high decay
 1005 multiplicity.

1006 Usage of b -tagging in this analysis is done via five operating points (OPs), corresponding

1007 to 65%, 70%, 77%, 85% and 90% b -jet tagging efficiency ε_b in simulated $t\bar{t}$ events, in order
1008 from the tightest to loosest discriminant cut point. The OPs are defined by placing selections
1009 on the tagger output to provide a predefined ε_b level; the selection cuts act as a variable
1010 trade-off between b -tagging efficiency and b -jet purity i.e. c - or light-jet rejection. For this
1011 analysis, a jet is considered b -tagged if it passes the 85% OP. The b -tagged jet is then
1012 assigned a pseudo-continuous b -tagging (PCBT) score, which quantifies a jet's ability to
1013 satisfy different OPs. The score can take integer values between 1 and 6, where a score of 6
1014 is assigned to jets passing all OP thresholds; a score of 2 for jets that pass only the tightest
1015 OP (90%); and a score of 1 for jets that pass no OP. A value of -1 is also defined for any jet
1016 that does not satisfy b -tagging criteria. Since the targeted $t\bar{t}t\bar{t}$ final states contain at least
1017 four b -hadrons from top and W decays, a b -tagging OP of 85% is used to maintain high
1018 purity during b -tagged jet selections in the signal region.

1019 **GN2 b -tagging algorithm**

1020 For this analysis, b -jets are identified and tagged with the GN2v01 b -tagger [113]. The
1021 GN2 algorithm uses a Transformer-based model [114] modified to incorporate domain knowl-
1022 edge and additional auxiliary physics objectives: grouping tracks with a common vertex and
1023 predicting the underlying physics process for a track. The network structure is shown in
1024 Figure 4.3. The GN2 b -tagger form the input vector by concatenating 2 jet variables and
1025 19 track reconstruction variables (for up to 40 tracks), normalized to zero mean and unit
1026 variance. The output consists of a track-pairing output layer of size 2, a track origin clas-
1027 sification layer of 7 categories, and a jet classification layer of size 4 for the probability of
1028 each jet being a b -, c -, light- or τ -jet respectively. For b -tagging purpose, a discriminant is

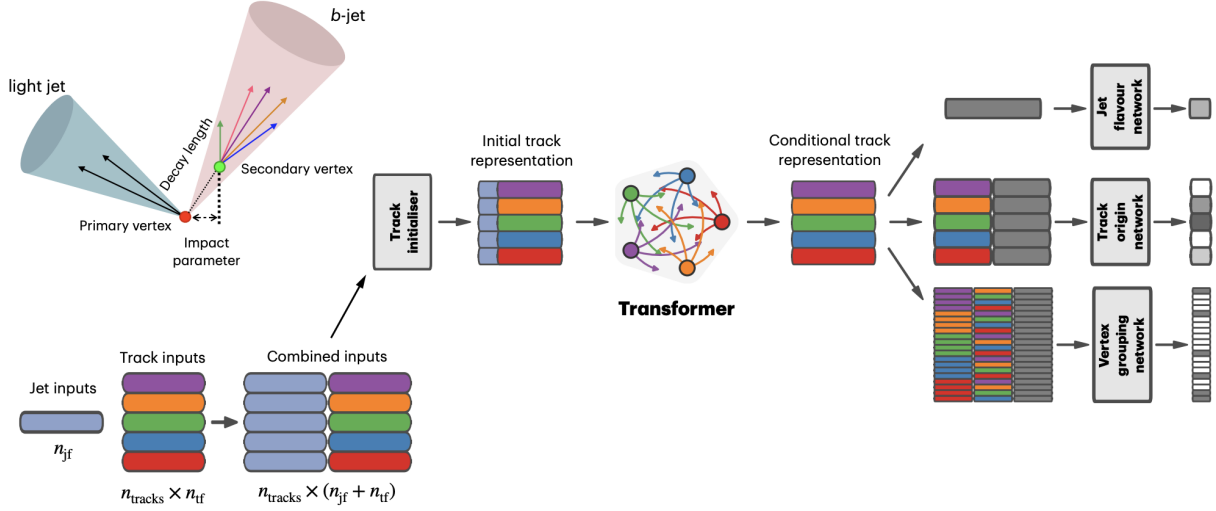


Figure 4.3: Overview of the GN2 architecture. The number of jet and track features are represented by n_{jf} and n_{tf} respectively. The global jet representation and track embeddings output by the Transformer encoder are used as inputs for three task-specific networks [113].

1029 defined using these four outputs

$$D_b = \ln \left(\frac{p_b}{f_c p_c + f_\tau p_\tau + (1 - f_c - f_\tau)p_{\text{light}}} \right) \quad (4.1)$$

1030 where p_x is the probability of the jet being an x -jet as predicted by GN2, and f_c, f_τ are tun-
 1031 able free parameters controlling balance between c - and light-jet rejection. Simulated SM $t\bar{t}$
 1032 and BSM Z' events from pp collisions were used as training and evaluation samples. In order
 1033 to minimize bias, both b - and light-jet samples are re-sampled to match c -jet distributions.
 1034 Figure 4.4 shows the performance of GN2 compared to the previous convolutional neural
 1035 network-based standard b -tagging algorithm DL1d, in terms of c -, light- and τ -jet rejection
 1036 as a function of b -tagging efficiency. The network gives a factor of 1.5-4 improvement in
 1037 experimental applications compared to DL1d [113], without dependence on the choice of
 1038 MC event generator or inputs from low-level flavor tagging algorithm.

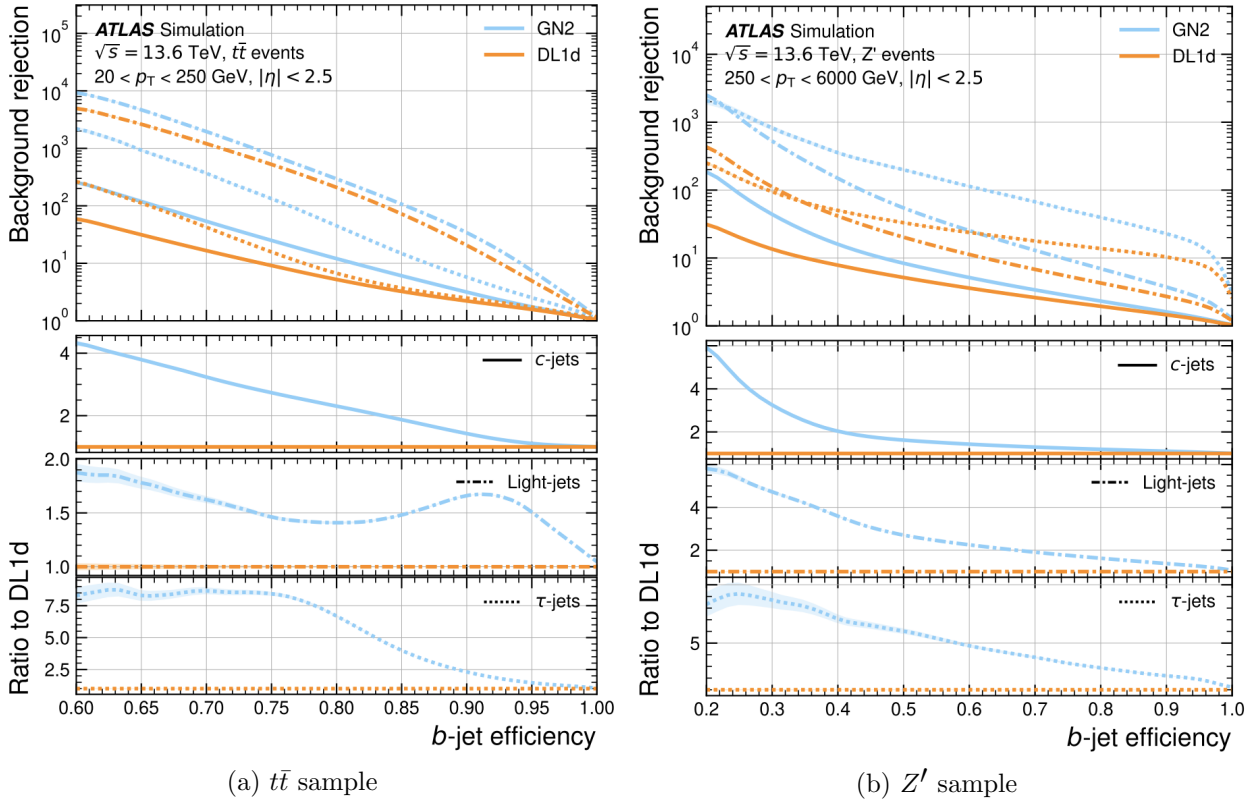


Figure 4.4: The c -, light- and τ -jet rejection rate as a function of b -tagging efficiency for GN2 and DL1d using (a) jets in the $t\bar{t}$ sample, and (b) jets in the Z' sample. The performance ratios of GN2 to DL1d are shown in the bottom panels [113].

1039 Efficiency calibration

1040 Due to imperfect description of detector response and physics modeling effects in simu-
 1041 lation, the b -tagging efficiency predicted by MC simulation $\varepsilon_b^{\text{sim}}$ requires a correction factor
 1042 to match the efficiency measured in collision data $\varepsilon_b^{\text{data}}$. The correction scale factors (SFs)
 1043 are defined as $\text{SF} = \varepsilon_b^{\text{data}} / \varepsilon_b^{\text{sim}}$ and are determined by data-to-MC calibration using samples
 1044 enriched in dileptonic $t\bar{t}$ decays [115]. The resulting SFs are applied to MC simulated jets
 1045 individually.

1046 4.3 Leptons

1047 Lepton reconstruction in ATLAS involves electron and muon reconstruction since tau
1048 decays quickly, and depending on decay mode can be reconstructed using either jets or light
1049 leptons. From here on out within this dissertation, leptons will be used exclusively to refer to
1050 electrons and muons. Leptons can be classified into two categories: prompt leptons resulting
1051 from heavy particle decays and non-prompt leptons resulting from detector or reconstruction
1052 effects, or from heavy-flavor hadron decays.

1053 4.3.1 Electrons

1054 Electrons leave energy signature in the detector by interacting with the detector materials
1055 and losing energy in the form of bremsstrahlung photons. A bremsstrahlung photon can
1056 produce an electron-positron pair which can itself deposit signals in the detector, creating a
1057 cascade of particles that can leave multiple of either tracks in the ID or EM showers in the
1058 calorimeters, all of which are considered part of the same EM topo-cluster. Electron signal
1059 signature has three characteristic components: localized energy deposits in the calorimeters,
1060 multiple tracks in the ID and compatibility between the above tracks and energy clusters in
1061 the $\eta \times \phi$ plane [116]. Electron reconstruction in ATLAS follows these steps accordingly.

1062 Seed-cluster reconstruction and track reconstruction are performed sequentially in ac-
1063 cordance with the iterative topo-clustering algorithm and track reconstruction method de-
1064 scribed in section 4.1. The seed-cluster and GSF-refitted track candidate not associated
1065 with a conversion vertex are matched to form an electron candidate. The cluster energy is
1066 then calibrated using multivariate techniques on data and simulation to match the original
1067 electron energy.

1068 **Electron identification**

1069 Additional LH-based identification selections using ID and EM calorimeter information
1070 are implemented to further improve the purity of reconstructed electrons in the $|\eta| < 2.47$ re-
1071 gion of the detector [116]. The electron LH function is built with the signal being prompt elec-
1072 trons and background being objects with similar signature to prompt electrons i.e. hadronic
1073 jet deposits, photon conversions or heavy-flavor hadron decays. Three identification OPs
1074 are defined for physics analyses: *Loose*, *Medium* and *Tight*, optimized for 9 bins in $|\eta|$ and
1075 12 bins in E_T with each OP corresponding to a fixed efficiency requirement for each bin.
1076 For typical EW processes, the target efficiencies for *Loose*, *Medium* and *Tight* start at 93%,
1077 88% and 80% respectively and increase with E_T . Similar to b -tagging OPs, the electron
1078 identification OPs represent a trade-off in signal efficiency and background rejection. The
1079 electron efficiency are estimated using tag-and-probe method on samples of $J/\Psi \rightarrow ee$ and
1080 $Z \rightarrow ee$ [116]. The *Tight* electron identification OP is used for this analysis.

1081 **Electron isolation**

1082 A characteristic distinction between prompt electrons and electrons from background
1083 processes is the relative lack of activity in both the ID and calorimeters within an $\Delta\eta \times \Delta\phi$
1084 area surrounding the reconstruction candidate. Calorimeter-based and track-based electron
1085 isolation variables [116] are defined to quantify the amount of activity around the electron
1086 candidate using topo-clusters and reconstructed tracks respectively.

1087 Calorimeter-based isolation variables $E_T^{\text{cone}XX}$ are computed by first summing the energy
1088 of topo-clusters with barycenters falling within a cone of radius $\Delta R = \sqrt{(\Delta\eta)^2 + (\Delta\phi)^2} =$
1089 $XX/100$ around the direction of the electron candidate. The final isolation variables are

obtained by subtracting from the sum the energy belonging to the candidate electron at the core of the cone, then applying corrections for pile-up effects and energy leakage outside of the core. Similar to calorimeter-based variables, track-based isolation variables $p_T^{\text{varcone}XX}$ are calculated by summing all track p_T within a cone of radius ΔR around the electron candidate, minus the candidate's contribution. The cone radius is variable as a function of p_T and is described as

$$\Delta R \equiv \min \left(\frac{10}{p_T}, \Delta R_{\max} \right), \quad (4.2)$$

where p_T is expressed in GeV and ΔR_{\max} is the maximum cone size, defined to account for closer proximity of decay products to the electron in high-momentum heavy particle decays. Four isolation operating points are implemented to satisfy specific needs by physics analyses: *Loose*, *Tight*, *HighPtCaloOnly* and *Gradient* [116]. For this analysis, electrons isolation uses *Tight* requirements.

1101 Electron charge misidentification

Charge misidentification is a crucial irreducible background, particularly for analyses with electron charge selection criteria. Electron charge is determined by the curvature of the associated reconstructed track, and misidentification of charge can occur via either an incorrect curvature measurement or an incorrectly matched track. Inaccurate measurement is more likely for high energy electrons due to the small curvature in track trajectories at high p_T , while track matching error usually results from bremsstrahlung pair-production generating secondary tracks in close proximity [116]. Suppression of charge misidentification background in Run 2 is additionally assisted by a boosted decision tree discriminant known

1110 as the Electron Charge ID Selector (ECIDS). For this analysis, all electrons are required to
1111 pass the ECIDS criterion.

1112 4.3.2 Muons

1113 Muons act as minimum-ionizing particles, leaving tracks in the MS or characteristics
1114 energy deposits in the calorimeter and can be reconstructed globally using information from
1115 the ID, MS and calorimeters. Five reconstruction strategies corresponding to five muon
1116 types [117] are utilized in ATLAS:

- Combined (CB): the primary ATLAS muon reconstruction method. Combined muons
1117 are first reconstructed using MS tracks then extrapolated to include ID tracks (outside-in strategy). A global combined track fit is performed on both MS and ID tracks.
- Inside-out combined (IO): complementary to CB reconstruction. IO muon tracks are
1118 extrapolated from ID to MS, then fitted with MS hits and calorimeter energy loss in a
1119 combined track fit.
- MS extrapolated (ME): ME muons are defined as muons with a MS track that cannot
1120 be matched to an ID track using CB reconstruction. ME muons allow extension of
1121 muon reconstruction acceptance to regions not covered by the ID ($2.5 < |\eta| < 2.7$)
- Segment-tagged (ST): ST muons are defined as a successfully matched ID track that
1122 satisfies tight angular matching criteria to at least one reconstructed MDT or CSC
1123 segment when extrapolated to the MS. MS reconstruction is used primarily when
1124 muons only crossed one layer of MS chambers.
- Calorimeter-tagged (CT): CT muons are defined as an ID track that can be matched to

1131 energy deposits consistent with those of a minimum-ionizing particle when extrapolated
1132 through the calorimeter. CT reconstruction extends acceptance range to regions in the
1133 MS with sparse instrumentation ($|\eta| < 0.1$) with a higher p_T threshold of 5 GeV,
1134 compared to the 2 GeV threshold used by other muon reconstruction algorithms due
1135 to large background contamination at the low p_T range of $15 < p_T < 100$ GeV [118].

1136 Muon identification

1137 Reconstructed muons are further filtered by identification criteria to select for high-
1138 quality prompt muons. Requirements include number of hits in the MS and ID, track fit
1139 properties and compatibility between measurements of the two systems. Three standard
1140 OPs (*Loose*, *Medium*, *Tight*) are defined to better match the needs of different physics
1141 analyses concerning prompt muon p_T resolution, identification efficiency and non-prompt
1142 muon rejection. The default identification OP for ATLAS physics and also the OP used in
1143 this analysis is *Medium*, which provides efficiency and purity suitable for a wide range of
1144 studies while minimizing systematic uncertainties [117].

1145 Muon isolation

1146 Muons from heavy particle decays are often produced in an isolated manner compared to
1147 muons from semileptonic decays, and is therefore an important tool for background rejection
1148 in many physics analyses. Muon isolation strategies are similar to that of electron in section
1149 4.3.1, with track-based and calorimeter-based isolation variables. Seven isolation OPs are
1150 defined using either or both types of isolation variables, balancing between prompt muon
1151 acceptance and non-prompt muon rejection. The full definition and description for the muon
1152 isolation OPs are detailed in Ref. [117].

1153 4.4 Missing transverse momentum

1154 Collisions at the LHC happen along the z -axis of the ATLAS coordination system between
1155 two particle beam of equal center-of-mass energy. By conservation of momentum, the sum of
1156 transverse momenta of outgoing particles should be zero. A discrepancy between measured
1157 momentum and zero would then suggest the presence of undetectable particles, which would
1158 consist of either SM neutrinos or some unknown BSM particles, making missing transverse
1159 momentum (E_T^{miss}) an important observable to reconstruct.

1160 Reconstructing E_T^{miss} utilizes information from fully reconstructed leptons, photons, jets
1161 and other matched track-vertex objects not associated with a prompt object (soft signals),
1162 defined with respect to the $x(y)$ -axis as

$$E_{x(y)}^{\text{miss}} = - \sum_{i \in \{\text{hard objects}\}} p_{x(y),i} - \sum_{j \in \{\text{soft signals}\}} p_{x(y),j}, \quad (4.3)$$

1163 where $p_{x(y)}$ is the $x(y)$ -component of p_T for each particle [119]. The following observables
1164 can then be defined:

$$\begin{aligned} \mathbf{E}_T^{\text{miss}} &= (E_x^{\text{miss}}, E_y^{\text{miss}}), \\ E_T^{\text{miss}} &= |\mathbf{E}_T^{\text{miss}}| = \sqrt{(E_x^{\text{miss}})^2 + (E_y^{\text{miss}})^2}, \\ \phi^{\text{miss}} &= \tan^{-1}(E_y^{\text{miss}}/E_x^{\text{miss}}), \end{aligned} \quad (4.4)$$

1165 where E_T^{miss} represents the magnitude of the missing transverse energy vector $\mathbf{E}_T^{\text{miss}}$, and
1166 ϕ^{miss} its direction in the transverse plane. The vectorial sum $\mathbf{E}_T^{\text{miss}}$ can be broken down into

$$\mathbf{E}_T^{\text{miss}} = - \underbrace{\sum_{\text{selected electrons}} \mathbf{p}_T^e - \sum_{\text{selected muons}} \mathbf{p}_T^\mu - \sum_{\text{accepted photons}} \mathbf{p}_T^\gamma - \sum_{\text{accepted } \tau\text{-leptons}} \mathbf{p}_T^\tau}_{\text{hard term}} - \underbrace{\sum_{\text{accepted jets}} \mathbf{p}_T^{\text{jet}} - \sum_{\text{unused tracks}} \mathbf{p}_T^{\text{track}}}_{\text{soft term}}. \quad (4.5)$$

1167 Two OPs are defined for E_T^{miss} , *Loose* and *Tight*, with selections on jet p_T and JVT criteria
1168 [120]. The *Tight* OP is used in this analysis; *Tight* reduces pile-up dependence of E_T^{miss}
1169 by removing the phase space region containing more pile-up than hard-scatter jets, at the
1170 expense of resolution and scale at low pile-up,

1171 4.5 Overlap removal

1172 Since different objects are reconstructed independently, it is possible for the same de-
1173 tector signals to be used to reconstruct multiple objects. An overlap removal strategy is
1174 implemented to resolve ambiguities; the overlap removal process for this analysis applies
1175 selections in Table 4.1 sequentially, from top to bottom.

Table 4.1: Overlap removal process for this analysis, applied sequentially from top to bottom.

Remove	Keep	Matching criteria
Electron	Electron	Shared ID track, $p_{T,1}^e < p_{T,2}^e$
Muon	Electron	Shared ID track, CT muon
Electron	Muon	Shared ID track
Jet	Electron	$\Delta R < 0.2$
Electron	Jet	$\Delta R < 0.4$
Jet	Muon	($\Delta R < 0.2$ or ghost-associated) & $N_{\text{track}} < 3$
Muon	Jet	$\Delta R < \min(0.4, 0.04 + 10\text{GeV}/p_T^\mu)$

1176 4.6 Object definition

1177 Table 4.2 summarizes the selections on physics objects used in this analysis. Each se-
1178 lection comes with associated calibration scale factors (SFs) to account for discrepancies
1179 between data and MC simulation, and are applied multiplicatively to MC event weights.

Table 4.2: Summary of object selection criteria used in this analysis. ℓ_0 refers to the leading lepton in the event.

Selection	Electrons	Muons	Jets
p_T [GeV]	> 15 $p_T(\ell_0) > 28$	> 15	> 20
$ \eta $	$1.52 \leq \eta < 2.47$ < 1.37	< 2.5	< 2.5
Identification	<i>TightLH</i> pass ECIDS ($ee/e\mu$)	<i>Medium</i>	NNJvt <i>FixedEffPt</i> ($p_T < 60$, $ \eta < 2.4$)
Isolation	<i>Tight_VarRad</i>	<i>PflowTight_VarRad</i>	
Track-vertex assoc.			
$ d_0^{\text{BL}}(\sigma) $	< 5	< 3	
$ \Delta z_0^{\text{BL}} \sin \theta $ [mm]	< 0.5	< 0.5	

1180 Chapter 5. Data & Simulated Samples

1181 5.1 Data samples

1182 Data samples used in this analysis were collected by the ATLAS detector during the Run
1183 2 data-taking campaign between 2015-2018. The samples contain pp collisions at center-of-
1184 mass energy of $\sqrt{s} = 13$ TeV with 25 ns bunch-spacing, which corresponds to an integrated
1185 luminosity of 140 fb^{-1} with an uncertainty of 0.83% [89]. The HLT trigger strategy is similar
1186 to that of previous $t\bar{t}t\bar{t}$ observation analysis [44] and include single lepton and dilepton
1187 triggers. Calibration for di-muon and electron-muon triggers were not ready for the samples
1188 used in this analysis, and are therefore not included. Events are also required to contain at
1189 least one lepton matched to the corresponding object firing the trigger. Triggers utilized in
1190 this analysis are summarized in Table 5.1, with efficiency close to 100% when used together.

1191 5.2 Monte Carlo samples

1192 Monte Carlo simulated samples are used to estimate signal acceptance before unblinding,
1193 profile the physics background for the analysis and to study object optimizations. Simulated
1194 samples for this analysis use are generated from ATLAS generalized MC20a/d/e samples for
1195 Run 2, using full detector simulation (FS) and fast simulation (AF3) to simulate detector
1196 response. MC samples used and simulation processes are summarized in Table 5.2.

Table 5.1: Summary of all HLT triggers used in this analysis. Events are required to pass at least one trigger.

Trigger	Data period			
	2015	2016	2017	2018
Single electron triggers				
HLT_e24_lhmedium_L1EM20VH	✓	-	-	-
HLT_e60_lhmedium	✓	-	-	-
HLT_e120_lhloose	✓	-	-	-
HLT_e26_lhtight_nod0_ivarloose	-	✓	✓	✓
HLT_e60_lhmedium_nod0	-	✓	✓	✓
HLT_e140_lhloose_nod0	-	✓	✓	✓
Di-electron triggers				
HLT_2e12_lhloose_L12EM10VH	✓	-	-	-
HLT_2e17_lhvloose_nod0	-	✓	-	-
HLT_2e24_lhvloose_nod0	-	-	✓	✓
HLT_2e17_lhvloose_nod0_L12EM15VHI	-	-	-	✓
Single muon trigger				
HLT_mu20_iloose_L1MU15	✓	-	-	-
HLT_mu40	✓	-	-	-
HLT_mu26_ivarmedium	-	✓	✓	✓
HLT_mu50	-	✓	✓	✓

¹¹⁹⁷ 5.2.1 $t\bar{t}Z'$ signal samples

¹¹⁹⁸ Signal $t\bar{t}Z'$ samples were generated based on the simplified topophilic resonance model in
¹¹⁹⁹ section 2.2.1. Six Z' mass points were utilized for the generation of the signal sample: 1000,
¹²⁰⁰ 1250, 1500, 2000, 2500 and 3000 GeV. The top- Z' coupling c_t is chosen to be 1 for a narrow
¹²⁰¹ resonance peak, and the chirality angle θ is chosen to be $\pi/4$ to suppress loop production
¹²⁰² of Z' . The samples were then generated with MADGRAPH5_AMC@NLO v.3.5.0 [121] at
¹²⁰³ LO with the NNPDF3.1LO [122] PDF set interfaced with PYTHIA8 [123] using A14 tune
¹²⁰⁴ and NNPDF2.3lo PDF set for parton showering and hadronization. The resonance width is
¹²⁰⁵ calculated to be 4% for $c_t = 1$.

Table 5.2: Summary of all Monte-Carlo samples used in this analysis. V refers to an EW ($W^\pm/Z/\gamma^*$) or Higgs boson. Matrix element (ME) order refers to the order in QCD of the perturbative calculation. Tune refers to the underlying-event tune of the parton shower (PS) generator.

Process	ME Generator	ME Order	ME PDF	PS	Tune	Sim.
Signals						
$t\bar{t}Z'$	MADGRAPH5_AMC@NLO LO		NNPDF3.1LO		PYTHIA8 A14	FS
$t\bar{t}t\bar{t}$ and $t\bar{t}\bar{t}$						
$t\bar{t}t\bar{t}$	MADGRAPH5_AMC@NLO NLO		NNPDF3.0nlo		PYTHIA8 A14	AF3
	MADGRAPH5_AMC@NLO NLO		MMHT2014 LO		HERWIG7 H7-UE-MMHT	AF3
	SHERPA	NLO	NNPDF3.0nnlo		HERWIG7 SHERPA	FS
$t\bar{t}\bar{t}$	MADGRAPH5_AMC@NLO LO		NNPDF2.3lo		PYTHIA8 A14	AF3
$t\bar{t}V$						
$t\bar{t}H$	POWHEGBOX v2	NLO	NNPDF3.0nlo		PYTHIA8 A14	FS
	POWHEGBOX v2	NLO	NNPDF3.0nlo		HERWIG7 H7.2-Default	FS
$t\bar{t}(Z/\gamma^*)$	MADGRAPH5_AMC@NLO NLO		NNPDF3.0nlo		PYTHIA8 A14	FS
	SHERPA	NLO	NNPDF3.0nnlo		SHERPA SHERPA	FS
$t\bar{t}W$	SHERPA	NLO	NNPDF3.0nnlo		SHERPA SHERPA	FS
	SHERPA	LO	NNPDF3.0nnlo		SHERPA SHERPA	FS
$t\bar{t}$ and Single-Top						
$t\bar{t}$	POWHEGBOX v2	NLO	NNPDF3.0nlo		PYTHIA8 A14	FS
tW	POWHEGBOX v2	NLO	NNPDF3.0nlo		PYTHIA8 A14	FS
$t(q)b$	POWHEGBOX v2	NLO	NNPDF3.0nlo (s)		PYTHIA8 A14	FS
			NNPDF3.0nlo 4f (t)			FS
tWZ	MADGRAPH5_AMC@NLO NLO		NNPDF3.0nlo		PYTHIA8 A14	FS
tZ	MADGRAPH5_AMC@NLO LO		NNPDF3.0nlo 4f		PYTHIA8 A14	FS
$t\bar{t}VV$						
$t\bar{t}WW$	MADGRAPH5_AMC@NLO LO		NNPDF3.0nlo		PYTHIA8 A14	FS
$t\bar{t}WZ$	MADGRAPH	LO	NNPDF3.0nlo		PYTHIA8 A14	AF3
$t\bar{t}HH$	MADGRAPH	LO	NNPDF3.0nlo		PYTHIA8 A14	AF3
$t\bar{t}WH$	MADGRAPH	LO	NNPDF3.0nlo		PYTHIA8 A14	AF3
$t\bar{t}ZZ$	MADGRAPH	LO	NNPDF3.0nlo		PYTHIA8 A14	AF3
$V(VV)+\text{jets}$ and VH						
$V+\text{jets}$	SHERPA	NLO	NNPDF3.0nnlo		SHERPA SHERPA	FS
$VV+\text{jets}$	SHERPA	NLO	NNPDF3.0nnlo		SHERPA SHERPA	FS
		LO ($gg \rightarrow VV$)				FS
$VVV+\text{jets}$	SHERPA	NLO	NNPDF3.0nnlo		SHERPA SHERPA	FS
VH	POWHEGBOX v2	NLO	NNPDF3.0aznlo		PYTHIA8 A14	FS

₁₂₀₆ **5.2.2 Background samples**

₁₂₀₇ **SM $t\bar{t}t\bar{t}$ background**

₁₂₀₈ The nominal SM $t\bar{t}t\bar{t}$ sample was generated with MADGRAPH5_AMC@NLO [121] at
₁₂₀₉ NLO in QCD with the NNPDF3.0nlo [122] PDF set and interfaced with PYTHIA8.230 [123]
₁₂₁₀ using A14 tune [124]. Decays for top quarks are simulated at LO with MADSPIN [125,
₁₂₁₁ 126] to preserve spin information, while decays for b - and c -hadrons are simulated with
₁₂₁₂ EVTGEN v1.6.0 [127]. The renormalization and factorization scales μ_R and μ_F are set
₁₂₁₃ to $1/4\sqrt{m^2 + p_T^2}$, which represents the sum of transverse mass of all particles generated
₁₂₁₄ from the ME calculation [128]. The ATLAS detector response was simulated with AF3.
₁₂₁₅ Additional auxiliary $t\bar{t}t\bar{t}$ samples are also generated to evaluate the impact of generator and
₁₂₁₆ PS uncertainties as shown in 5.2.

₁₂₁₇ **$t\bar{t}W$ background**

₁₂₁₈ Nominal $t\bar{t}W$ sample was generated using SHERPA v2.2.10 [129] at NLO in QCD with
₁₂₁₉ the NNPDF3.0nnlo [122] PDF with up to one extra parton at NLO and two at LO, which
₁₂₂₀ are matched and merged with the SHERPA PS based on Catani-Seymour dipole factorization
₁₂₂₁ [130] using the MEPS@NLO prescription [131–134] and a merging scale of 30 GeV. Higher-
₁₂₂₂ order ME corrections are provided in QCD by the OpenLoops 2 library [135–137] and in
₁₂₂₃ EW from $\mathcal{O}(\alpha^3) + \mathcal{O}(\alpha_S^2\alpha^2)$ (LO3 & NLO2) via two sets of internal event weights. An
₁₂₂₄ alternative sample with only EW corrections at LO from $\mathcal{O}(\alpha_S\alpha^3)$ (NLO3) diagrams were
₁₂₂₅ also simulated with the same settings.

1226 **$t\bar{t}(Z/\gamma^*)$ background**

1227 Nominal $t\bar{t}(Z/\gamma^*)$ samples were generated separately for different ranges of dilepton in-
1228 variant mass $m_{\ell\ell}$ to account for on-shell and off-shell Z/γ^* production. Sample for $m_{\ell\ell}$
1229 between 1 and 5 GeV was produced using MADGRAPH5_AMC@NLO [121] at NLO with
1230 the NNPDF3.0nlo [122] PDF set, interfaced with PYTHIA8.230 [123] using A14 tune [124] and
1231 NNPDF2.3l0 PDF set. Sample for $m_{\ell\ell} < 5$ GeV was produced with SHERPA v2.2.10 [129]
1232 at NLO using NNPDF3.0nnlo PDF set. To account for generator uncertainty, an alternative
1233 $m_{\ell\ell} > 5$ GeV sample was generated with identical settings to the low $m_{\ell\ell}$ sample. The
1234 ATLAS detector response was simulated with full detector simulation (FS).

1235 **$t\bar{t}H$ background**

1236 Generation of $t\bar{t}H$ background was done using POWHEGBox [138–141] at NLO in QCD
1237 with the NNPDF3.0nlo PDF [122] set. The nominal sample is interfaced with PYTHIA8.230
1238 [123] using the A14 tune [124] and the NNPDF2.3l0 [142] PDF set. Detector response is
1239 simulated using FS. An alternative $t\bar{t}H$ sample generated similarly, but instead interfaced
1240 with HERWIG7.2.3 [143, 144] to study the impact of parton shower and hadronization model.
1241 Detector response for the alternative sample is simulated using AF3.

1242 **$t\bar{t}t$ background**

1243 The $t\bar{t}t$ sample is generated using MADGRAPH5_AMC@NLO [121] at LO in QCD, inter-
1244 faced with PYTHIA8 [123] using the A14 tune [124]. The sample is produced in the five-flavor
1245 scheme [145] to prevent LO interference with $t\bar{t}t\bar{t}$.

1246 **$t\bar{t}$ background**

1247 The $t\bar{t}$ sample is modeled with POWHEGBox [138–141] at NLO in QCD with the NNPDF3.0nlo
1248 [122] PDF set and the h_{damp} parameter set to $1.5m_{\text{top}}$ [146]. Events are interfaced with
1249 PYTHIA8.230 [123] using the A14 tune [124] and the NNPDF2.3lō [142] PDF set.

1250 **Single-top (tW & $t(q)b$) background**

1251 Single-top tW -associated production is modeled using the POWHEGBox generator [138–
1252 141] at NLO in QCD in the five-flavor scheme [145] with the NNPDF3.0nlo [122] PDF set. In-
1253 terference with $t\bar{t}$ production [146] is handled using the diagram removal scheme [147]. Single-
1254 top $t(q)b$ production is modeled using the POWHEGBox generator at NLO in QCD with the
1255 s-channel production modeled in the five-flavor scheme with the NNPDF3.0nlo PDF set, while
1256 the t-channel production is modeled in the four-flavor scheme with the NNPDF3.0nlo 4f [122]
1257 PDF set. The $t\bar{t}WW$ contributions are normalized to NLO theoretical cross section. All
1258 single-top samples are interfaced with PYTHIA8.230 [123] using the A14 tune [124] and the
1259 NNPDF2.3lō [142] PDF set.

1260 **tWZ +jets background**

1261 The tWZ sample is generated using MADGRAPH5_AMC@NLO [121] at NLO in QCD
1262 with the NNPDF3.0nlo [122] PDF set, interfaced with PYTHIA8.212 [123] using the A14 tune
1263 [124] and the NNPDF2.3lō [142] PDF set.

1264 **tZ & $t\bar{t}VV$ background**

1265 Production of tZ is modeled using MADGRAPH5_AMC@NLO [121] at NLO in QCD
1266 with scale of $H_T/6$ and the NNPDF3.0nlo 4f [122] PDF set. Production of $t\bar{t}WW$ is modeled

1267 using `MADGRAPH5_AMC@NLO` [121] at LO, while production of $t\bar{t}WZ$, $t\bar{t}HH$, $t\bar{t}WH$ and
1268 $t\bar{t}ZZ$ are modeled using `MADGRAPH` at LO. All $t\bar{t}VV$ samples use the `NNPDF3.0nlo` [122]
1269 PDF set, and all samples in this section are interfaced with `PYTHIA8` [123] using the A14
1270 tune [124].

1271 Single boson (V) +jets background

1272 Production of V +jets is modeled with `SHERPA v2.2.10` [129] using NLO ME for up to two
1273 jets and LO ME for up to four jets, with the `NNPDF3.0nlo` [122] PDF set. Matrix elements
1274 are calculated with the Comix [148] and OpenLoops libraries [135, 136] and matched with
1275 the `SHERPA` PS based on Catani-Seymour dipole factorization [130] using the MEPS@NLO
1276 prescription [131–134]. The sample is normalized to the NNLO [149] theoretical cross section.

1277 Diboson (VV) +jets background

1278 Diboson samples are simulated with `SHERPA v2.2.14` [129] with the `NNPDF3.0nlo` [122]
1279 PDF set. Fully leptonic and semileptonic final states are generated using NLO ME for up to
1280 one extra parton and LO ME for up to three extra parton emissions. Loop-induced processes
1281 are generated using LO ME for up to one extra parton. Matrix elements are matched and
1282 merged with the `SHERPA` PS based on Catani-Seymour dipole factorization [130] using the
1283 MEPS@NLO prescription [131–134]. Virtual QCD ME corrections are provided by the
1284 OpenLoops library [135, 136].

1285 Triboson (VVV) +jets background

1286 The triboson sample is modeled with `SHERPA v2.2.10` [129] using factorized gauge boson
1287 decays. Matrix elements for the inclusive process at NLO and up to two extra partons at

1288 LO are matched and merged with the SHERPA PS based on Catani-Seymour dipole factor-
1289 ization [130] using the MEPS@NLO prescription [131–134]. Virtual QCD ME corrections
1290 are provided by the OpenLoops library [135, 136].

1291 ***VH* background**

1292 Generation of WH and ZH samples is performed using PowhegBox [138–141] at NLO
1293 with the NNPDF3.0aznlo [122] PDF set, interfaced with PYTHIA8.230 [123] using the A14
1294 tune [124] and the NNPDF2.3lo [142] PDF set.

1295

Chapter 6. Analysis Strategy

1296

6.1 Event selection

1297 Events for the analysis first are preselected following a list of criteria to optimize for event
1298 quality and background rejection. The following criteria are applied sequentially from top
1299 to bottom along with cleaning and veto cuts

1300 1. **Good Run List (GRL)**: data events must be part of a predefined list of suitable
1301 runs and luminosity blocks [[150](#)].

1302 2. **Primary vertex**: events must have at least one reconstructed vertex matched to 2 or
1303 more associated tracks with $p_T > 500$ MeV.

1304 3. **Trigger**: events must be selected by at least one trigger in Table 5.1.

1305 4. **Kinematic selection**: events must have exactly two *Tight* leptons with the same
1306 electric charge, or at least three *Tight* leptons of any charge. The leading lepton must
1307 have $p_T > 28$ GeV, and all leptons must satisfy $p_T > 15$ GeV.

1308 Events are separated into two channels based on the number of leptons: same-sign di-
1309 lepton (SS2L) for events with exactly two leptons of the same charge, or multilepton (ML)
1310 for events with three or more leptons. The channels are further separated into regions defined
1311 in section 6.2 to prepare for analysis.

1312 Additional selections are applied based on the lepton flavors present. In the SS2L channel,
1313 if both leptons are electrons, the invariant mass m_{ll} must satisfy $m_{ll} < 81$ GeV and $m_{ll} > 101$
1314 GeV to suppress background involving Z -bosons. In the ML channel, the same criteria must
1315 be satisfied for every opposite-sign same-flavor pair of leptons in an event.

1316 6.1.1 Event categorization

1317 Simulated events are categorized using truth information of leptons (e/μ) and their orig-
1318 inating MC particle (mother-particle). Each lepton can be classified as either prompt or
1319 non-prompt, with non-prompt leptons further categorized for background estimation pur-
1320 poses. If an event contains only prompt leptons, the event is classified as its correspond-
1321 ing process. If the event contains one non-prompt lepton, the event is classified as the corre-
1322 sponding type of the non-prompt lepton. If the event contains more than one non-prompt
1323 lepton, the event is classified as other.

1324 • **Prompt:** if the lepton originates from $W/Z/H$ boson decays, or from a mother-
1325 particle created by a final state photon.

1326 • **Non-prompt:**

1327 – **Charge-flip (e only):** if the reconstructed charge of the lepton differs from that
1328 of the first mother-particle.

1329 – **Material conversion (e only):** if the lepton originated from a photon conversion
1330 and the mother-particle is an isolated prompt photon, non-isolated final state
1331 photon, or heavy boson.

1332 – **γ^* -conversion (e only):** if the lepton originated from a photon conversion and
1333 the mother-particle is a background electron.

1334 – **Heavy flavor decay:** if the lepton originated from a b - or c -hadron.

1335 – **Fake:** if the lepton originated from a light- or s -hadron, or if the truth type of
1336 the lepton is hadron.

1337 – **Other:** any lepton that does not belong to one of the above categories.

1338 **6.2 Analysis regions**

1339 Events are selected and categorized into analysis regions belonging to one of two types:
1340 control regions (CRs) enriched in background events, and signal regions (SRs) enriched in
1341 signal events. This allows for the examination and control of backgrounds and systematic
1342 uncertainties, as well as study of signal sensitivities. The signal is then extracted from the
1343 SRs with a profile LH fit using all regions. The full selection criteria for each region are
1344 summarized in Table 6.1. The post-fit background compositions in different CRs and SR
1345 sub-regions are shown in Figure 6.1.

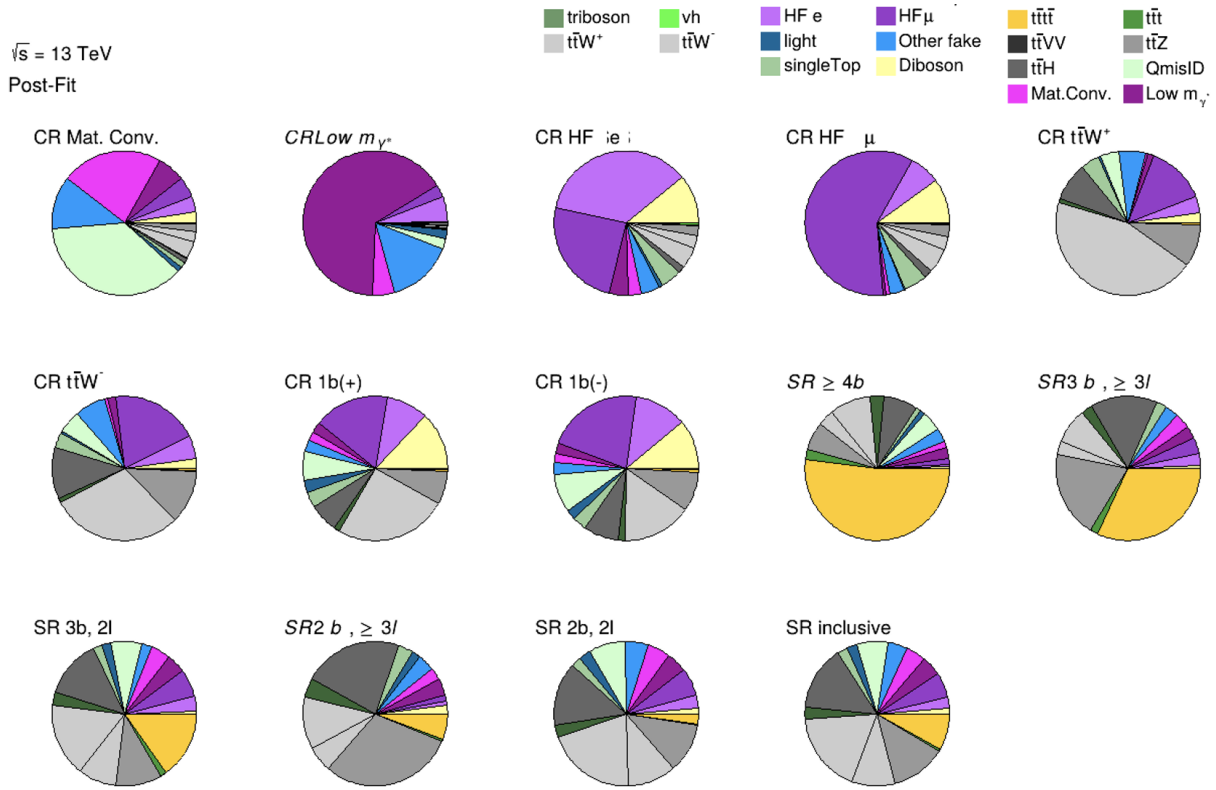


Figure 6.1: Post-fit background composition in each analysis region and sub-region. The fit was performed using ideal pseudo-datasets (Asimov data) in the SR.

Table 6.1: Definitions of signal, control and validation regions (VR) used in this analysis. N_{jets} and N_b refers to the number of jets and number of b -tagged jets respectively. ℓ_1 refers to the leading lepton, ℓ_2 refers to the subleading lepton and so on. H_T refers to the p_T scalar sum of all leptons and jets in the event. $m_{\ell\ell}$ refers to the dilepton invariant mass, which must not coincide with the Z -boson mass range of 81-101 GeV for SS2L+3L events.

Region	Channel	N_{jets}	N_b	Other selections	Fitted variable
CR Low m_{γ^*}	SS $e\ell$	[4, 6)	≥ 1	ℓ_1/ℓ_2 is from virtual photon decay $\ell_1 + \ell_2$ not from material conversion	event yield
CR Mat. Conv.	SS $e\ell$	[4, 6)	≥ 1	ℓ_1/ℓ_2 is from material conversion $\ell_1 + \ell_2$ not conversion candidates	event yield
CR HF μ	$\ell\mu\mu$	≥ 1	1	$100 < H_T < 300$ GeV $E_T^{\text{miss}} > 35$ GeV total charge = ± 1	$p_T(\ell_3)$
CR HF e	$e\ell\ell$	≥ 1	1	$\ell_1 + \ell_2$ not conversion candidates $100 < H_T < 275$ GeV $E_T^{\text{miss}} > 35$ GeV total charge = ± 1	$p_T(\ell_3)$
CR $t\bar{t}W^+$	SS $\ell\mu$	≥ 4	≥ 2	$ \eta(e) < 1.5$ for $N_b = 2$: $H_T < 500$ GeV or $N_{\text{jets}} < 6$ for $N_b \geq 3$: $H_T < 500$ GeV total charge > 0	N_{jets}
CR $t\bar{t}W^-$	SS $\ell\mu$	≥ 4	≥ 2	$ \eta(e) < 1.5$ for $N_b = 2$: $H_T < 500$ GeV or $N_{\text{jets}} < 6$ for $N_b \geq 3$: $H_T < 500$ GeV total charge < 0	N_{jets}
CR 1b(+)	SS2L+3L	≥ 4	1	$\ell_1 + \ell_2$ not from material conversion $H_T > 500$ GeV total charge > 0	N_{jets}
CR 1b(-)	SS2L+3L	≥ 4	1	$\ell_1 + \ell_2$ not from material conversion $H_T > 500$ GeV total charge < 0	N_{jets}
VR $t\bar{t}Z$	3L $\ell^\pm\ell^\mp$	≥ 4	≥ 2	$m_{\ell\ell} \in [81, 101]$ GeV	$N_{\text{jets}}, m_{\ell\ell}$
VR $t\bar{t}W +1b$	SS2L+3L			CR $t\bar{t}W^\pm$ CR 1b(\pm)	N_{jets}
VR $t\bar{t}W +1b+SR$	SS2L+3L			CR $t\bar{t}W^\pm$ CR 1b(\pm) SR	N_{jets}
SR	SS2L+3L	≥ 6	≥ 2	$H_T > 500$ GeV $m_{\ell\ell} \notin [81, 101]$ GeV	H_T

₁₃₄₆ **6.2.1 Signal regions**

₁₃₄₇ All events selected for the SR must satisfy the following criteria:

- ₁₃₄₈ • Contains 6 or more jets, with at least 2 jets b -tagged at the 85% OP.
- ₁₃₄₉ • Scalar sum of the transverse momenta of all leptons and jets $H_T > 500$ GeV.
- ₁₃₅₀ • Dilepton invariant mass $m_{\ell\ell}$ does not coincide with the Z -boson mass range of 81 – 101
- ₁₃₅₁ GeV

₁₃₅₂ The SR is further divided into sub-regions by the number of b -tagged jets and leptons
₁₃₅₃ present to study signal behavior and sensitivity with respect to the selection variables.

Table 6.2: Definitions of SR sub-regions. Events are sorted into different sub-regions based on the number of b -tagged jets and leptons present.

Sub-region	Selection criteria	
	b -jets	leptons
SR 2b2l	$N_b = 2$	$N_l = 2$
SR 2b3l4l	$N_b = 2$	$N_l \geq 3$
SR 3b2l	$N_b = 3$	$N_l = 2$
SR 3b3l4l	$N_b = 3$	$N_l \geq 3$
SR 4b	$N_b \geq 4$	

₁₃₅₄ **Signal extraction**

₁₃₅₅ Signal extraction in the SR is performed via a binned profile likelihood (LH) fit as de-
₁₃₅₆ scribed in section 8.1 using H_T as the discriminant observable. The discriminant observable
₁₃₅₇ for a LH fit serves as the set of observed data upon which the LH function is constructed.
₁₃₅₈ Ideally, the chosen observable shows significant separation between the functional forms of
₁₃₅₉ the signal and background distributions, allowing for effective separation of the two. Fig-
₁₃₆₀ ure 6.2 shows several pre-fit kinematic distributions in the inclusive SR. From empirical

1361 optimization studies, H_T possesses good discriminating power compared to other observ-
1362 ables constructed using event-level information.

1363 **6.2.2 Control regions**

1364 Control regions are defined for each background to be enriched in the targeted process, in
1365 order to maximize the background's purity and minimize contamination from other sources
1366 within the region. This helps to constrain and reduce correlation between background nor-
1367 malization factors in the final fit. Fit variables and selection criteria are determined via
1368 optimization studies performed on CRs that aimed to achieve the largest discriminating
1369 power possible between the target background and other event types.

1370 **$t\bar{t}W$ background CRs**

1371 Theoretical modeling for $t\bar{t}W + \text{jets}$ background in the phase space of this analysis suffers
1372 from large uncertainties, especially at high jet multiplicities [151]. A data-driven method was
1373 employed in a similar manner to the SM $t\bar{t}t\bar{t}$ observation analysis [44] to mitigate this effect
1374 and is described in further details in section 6.3.3. The method necessitates the definition of
1375 two groups of dedicated CRs to estimate the flavor composition and normalization of $t\bar{t}W$
1376 + jets background: CR $t\bar{t}W + \text{jets}$ to constrain flavor composition, and CR 1b to constrain
1377 the jet multiplicity spectrum. These are further split into CR $t\bar{t}W^\pm$ and CR 1b(\pm) to
1378 account for the pronounced asymmetry in $t\bar{t}W$ production from pp collisions at the LHC.
1379 The cross section of $t\bar{t}W^+$ production is approximately twice that of $t\bar{t}W^-$ [152] due to the
1380 combination of the main W^+ emission process being $u \rightarrow dW^+$ and the ratio of two u -quarks
1381 to one d -quark in the proton.

1382 Events in CR $t\bar{t}W^\pm$ are required to contain at least two b -tagged jets similar to the SR

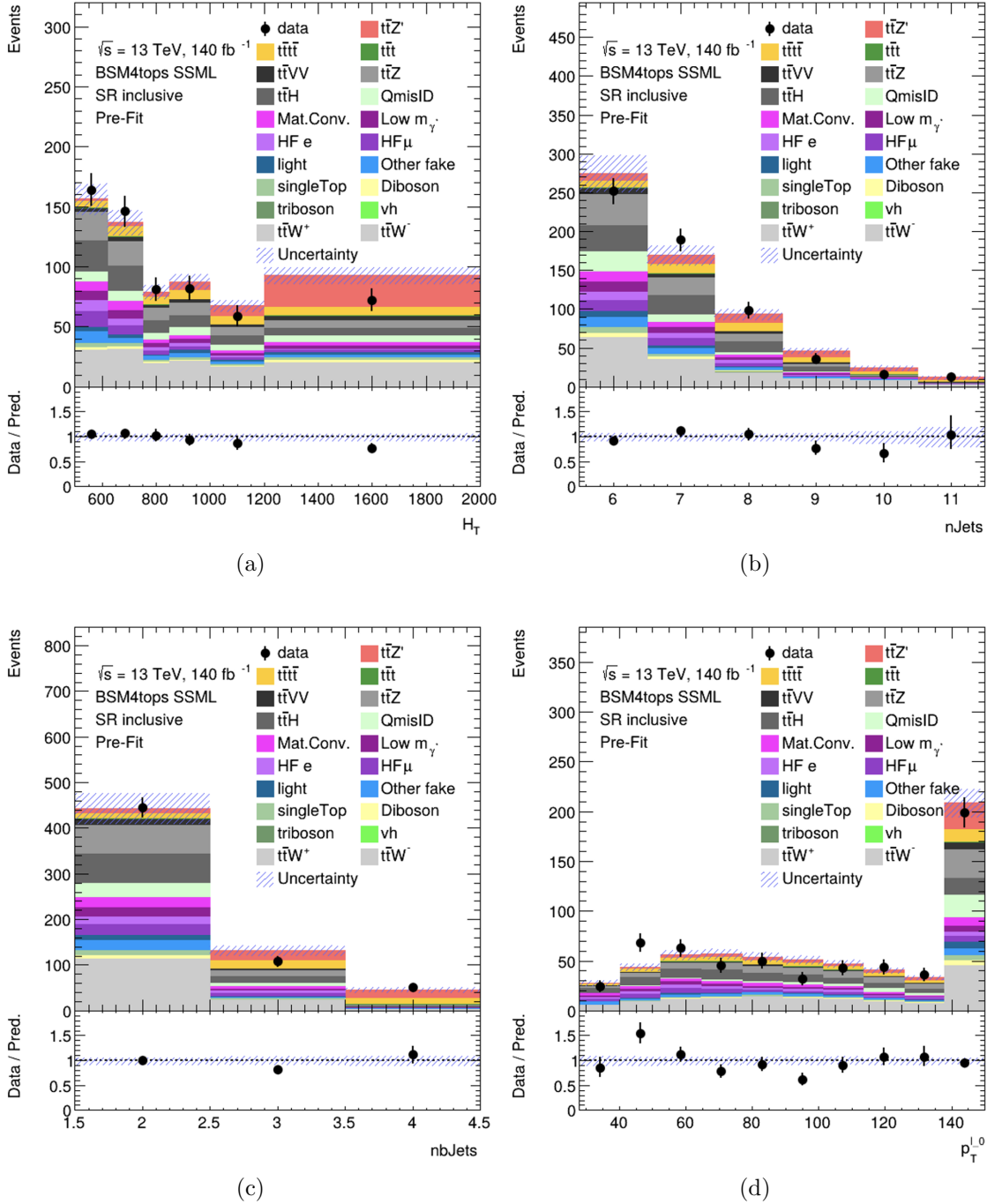


Figure 6.2: Pre-fit kinematic distributions and event compositions in the inclusive SR for (a) H_T i.e. scalar sum of p_T of all objects in the event, (b) jet multiplicity, (c) b -jet multiplicity, (d) leading lepton p_T . The shaded band represents the uncertainty in the total distribution. The first and last bins of each distribution contain underflow and overflow events respectively.

1383 to determine the $t\bar{t}W$ normalization within an SR-related phase space. Orthogonality with
 1384 SR is ensured by requiring $H_T < 500$ GeV or $N_{\text{jets}} < 6$ when $N_b = 2$, and $H_T < 500$
 1385 GeV when $N_b \geq 3$. Events in CR 1b(\pm) are required to have $H_T > 500$ GeV and at least
 1386 four jets to encompass events with high N_{jets} , which can be used to determine the $t\bar{t}W$ jet
 1387 multiplicity spectrum for fitting $a_{0,1}$. The selection criteria also include exactly one b -tagged
 1388 jet to maintain orthogonality with the SR.

1389 **Fake/non-prompt background CRs**

1390 Selection for fake/non-prompt CRs are determined using the `DFCommonAddAmbiguity`
 1391 (`DFCAA`) variable for reconstructed leptons.

Table 6.3: List of possible assigned values for DFCAA.

DFCAA	Description
-1	No 2nd track found
0	2nd track found, no conversion found
1	Virtual photon conversion candidate
2	Material conversion candidate

1392 Four CRs are defined for the three main types of fake/non-prompt backgrounds in the
 1393 analysis - virtual photon (γ^*) conversion, photon conversion in detector material (Mat.
 1394 Conv.) and heavy flavor decays (HF). The full selection criteria for fake/non-prompt CRs
 1395 are shown in Table 6.1.

1396 • **Low m_γ^* :** events with an e^+e^- pair produced from a virtual photon.

1397 Events are selected if there are two same-sign leptons with at least one electron recon-
 1398 structed as an internal conversion candidate, and neither reconstructed as a material
 1399 conversion candidate.

- 1400 • **Mat. Conv.**: events with an electron originating from photon conversion within the
1401 detector material.

1402 Events are selected if there are two same-sign leptons with at least one electron recon-
1403 structed as a material conversion candidate.

- 1404 • **HF $e(\mu)$** : events with a reconstructed non-prompt lepton from semi-leptonic decays of
1405 b - and c -hadrons (heavy flavor decays).

1406 Events are selected if there are three leptons with at least two electrons (muons), with
1407 no lepton reconstructed as a conversion candidate.

1408 6.3 Background estimation

1409 Background in this analysis consist of SM processes that can result in a signal signature
1410 similar to a $t\bar{t}t\bar{t}$ SSML final state and can be divided into two types, reducible and irreducible.
1411 Reducible background consists of processes that do not result in a SSML final state physically,
1412 but are reconstructed as such due to detector and reconstruction effects. The main types
1413 of reducible background considered are charge misidentification (QmisID) and fake/non-
1414 prompt leptons. Fake/non-prompt lepton backgrounds contaminate the SR when a non-
1415 prompt lepton is reconstructed as a prompt lepton in a $t\bar{t}$ -associated process, leading to
1416 a similar final state to that of SSML $t\bar{t}t\bar{t}$. These backgrounds are estimated using the
1417 template fitting method described in subsection 6.3.1, where MC simulations are normalized
1418 to their theoretical SM cross section via floating normalization factors (NFs) constrained by
1419 the corresponding CRs. Lepton charge misidentification background contaminates the SR
1420 similarly when one of the two leptons in a $t\bar{t}$ -associated process with two opposite-sign leptons
1421 is misidentified, producing a SS2L $t\bar{t}t\bar{t}$ final state. Charge misidentification background is

1422 estimated using a data-driven method described in section 6.3.2 along with ECIDS described
1423 in section 4.3.1.

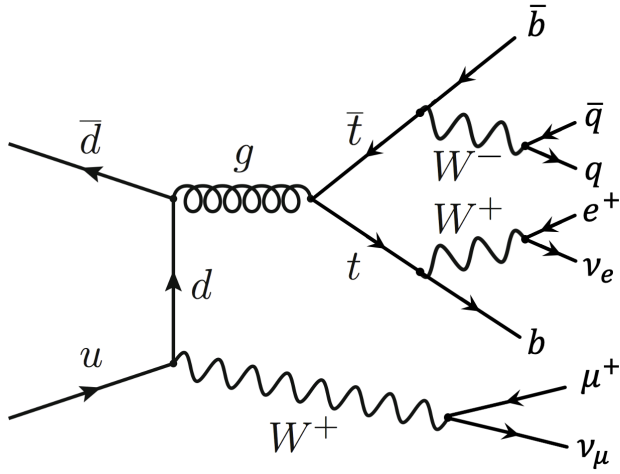


Figure 6.3: Feynman diagram for one possible $t\bar{t}W$ decay process with similar SS2L lepton signature to the $t\bar{t}Z'$ signal. Usually only two b -jets are present due to CKM suppression of b -quark production from W -boson decays; this is enough to allow $t\bar{t}W$ decays to enter and contaminate the SR.

1424 Irreducible background consists of SM processes that result in SSML final states with all
1425 leptons being prompt. The dominating background in the SR are SM $t\bar{t}t\bar{t}$, $t\bar{t}W$, $t\bar{t}Z$, and
1426 $t\bar{t}H$ production with smaller contributions from VV , VVV , VH and rarer processes like
1427 $t\bar{t}VV$, tWZ , tZq and $t\bar{t}t$. Most irreducible backgrounds are estimated using template fitting
1428 method, with the exception of $t\bar{t}W$ + jets background. The $t\bar{t}W$ + jets background is instead
1429 given four dedicated CRs, and estimated using a data-driven method with a fitted function
1430 parameterized in N_{jets} . All CRs and SR are included in the final profile LH fit to data.

1431 6.3.1 Template fitting for fake/non-prompt estimation

1432 The template fitting method is a semi-data-driven approach [151] that estimates fake/non-
1433 prompt background distributions by fitting the MC kinematic profile of background processes

1434 arising from fake/non-prompt leptons to data. The four main sources of fake/non-prompt
1435 leptons are generated from $t\bar{t}$ + jets samples and are constrained by four CRs enriched with
1436 the corresponding backgrounds. Each of the aforementioned background is assigned a free-
1437 floating NF resulting in $NF_{HF\ e}$, $NF_{HF\ \mu}$, $NF_{Mat.\ Conv.}$ and $NF_{Low\ m_{\gamma^*}}$. The NFs are fitted
1438 simultaneously with the signal within their constraining CRs.

1439 6.3.2 Charge misidentification data-driven estimation

1440 The ee and $e\mu$ channels in the SS2L $t\bar{t}t\bar{t}$ region are contaminated with opposite-sign
1441 (OS) dilepton $t\bar{t}$ -associated events where one electron has its charge misidentified. Charge
1442 misidentification (QmisID) largely affects electrons due to muons' precise curvature informa-
1443 tion using ID and MS measurements and low bremsstrahlung rate. The charge flip rates are
1444 significant at higher p_T and varies with $|\eta|$ which is proportional to the amount of detector
1445 material the electron interacted with.

1446 The charge flip probability ϵ is estimated in this analysis with a data-driven method
1447 [153] using a sample of $Z \rightarrow e^+e^-$ events with additional constraints on the invariant mass
1448 m_{ee} to be within 10 GeV of the Z -boson mass. The Z -boson mass window is defined to
1449 be within 4σ to include most events within the peak, and is determined by fitting the m_{ee}
1450 spectrum of the two leading electrons to a Breit-Wigner function, resulting in a range of
1451 [65.57, 113.49] for SS events and [71.81, 109.89] for OS events. Background contamination
1452 near the peak is assumed to be uniform and subtracted using a sideband method. Since the
1453 Z -boson decay products consist of a pair of opposite-sign electrons, all same-sign electron
1454 pairs are considered affected by charge misidentification.

1455 Let N_{ij}^{SS} be the number of events with SS electrons with the leading electron in the
1456 i^{th} 2D bin in $(p_T, |\eta|)$ and the sub-leading electron in the j^{th} bin. Assuming the QmisID

¹⁴⁵⁷ probabilities of electrons in an event are uncorrelated, N_{ij}^{SS} can be estimated as

$$N_{ij}^{\text{SS}} = N_{ij}^{\text{tot}} [\epsilon_i(1 - \epsilon_j) + \epsilon_j(1 - \epsilon_i)], \quad (6.1)$$

¹⁴⁵⁸ where N_{ij}^{tot} is the total number of events in the i^{th} and j^{th} bin regardless of charge, and

¹⁴⁵⁹ $\epsilon_{i(j)}$ is the QmisID rate in the $i^{\text{th}}(j^{\text{th}})$ bin. Assuming N_{ij}^{SS} follows a Poisson distribution

¹⁴⁶⁰ around the expectation value \bar{N}_{ij}^{SS} , the $(i, n)^{\text{th}}$ rate ϵ can be estimated by minimizing a

¹⁴⁶¹ negative-LLH function parameterized in p_T and $|\eta|$,

$$\begin{aligned} -\ln(\mathcal{L}(\epsilon | N_{\text{SS}})) &= -\ln \prod_{ij} \frac{(N_{ij}^{\text{tot}})^{N_{ij}^{\text{SS}}} \cdot e^{N_{ij}^{\text{tot}}}}{N_{ij}^{\text{SS}}!} \\ &= -\sum_{ij} \left[N_{ij}^{\text{SS}} \ln(N_{ij}^{\text{tot}}(\epsilon_i(1 - \epsilon_j) + \epsilon_j(1 - \epsilon_i))) - N_{ij}^{\text{tot}}(\epsilon_i(1 - \epsilon_j) + \epsilon_j(1 - \epsilon_i)) \right]. \end{aligned} \quad (6.2)$$

¹⁴⁶² The QmisID rates are then calculated separately for SR and CRs with different electron

¹⁴⁶³ definitions i.e. CR Low m_{γ^*} , CR Mat. Conv., CR $t\bar{t}W^\pm$, using events from data after

¹⁴⁶⁴ applying region-specific lepton selections and ECIDS. The events are required to satisfy

¹⁴⁶⁵ SS2L kinematic selections but contains OS electrons. The following weight is applied to OS

¹⁴⁶⁶ events to correct for misidentified SS events within the region,

$$w = \frac{\epsilon_i + \epsilon_j - 2\epsilon_i\epsilon_j}{1 - \epsilon_i - \epsilon_j + 2\epsilon_i\epsilon_j}. \quad (6.3)$$

¹⁴⁶⁷ The QmisID rates calculated for SR and CR $t\bar{t}W$ are shown in Figure 6.4

¹⁴⁶⁸ The QmisID rates obtained after applying w contain a dependency on jet multiplicity

¹⁴⁶⁹ and are underestimated at higher N_{jets} . This dependency affect the SR which require events

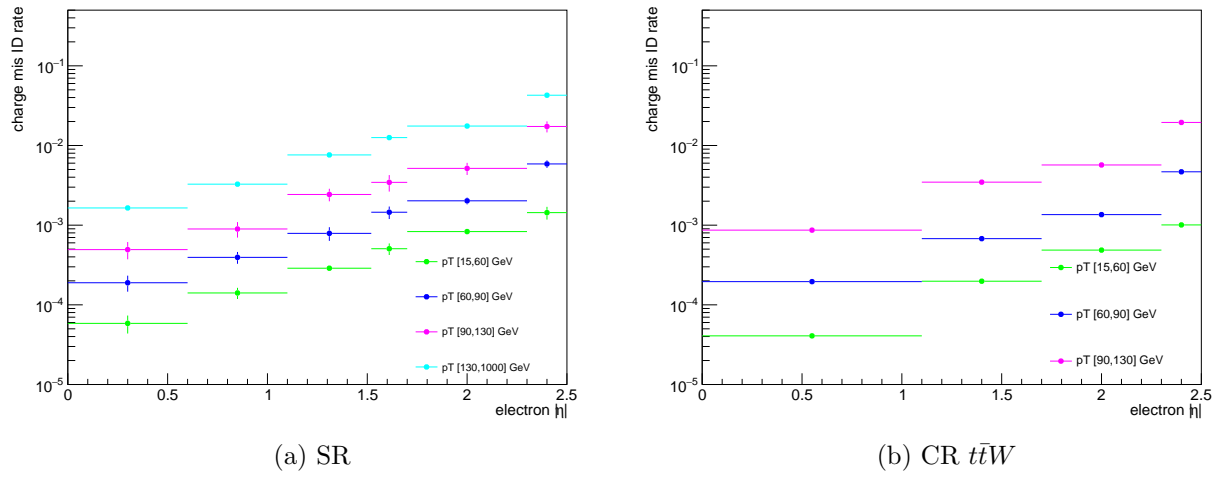


Figure 6.4: Charge flip rate calculated for SR and CR $t\bar{t}W$ in bins of $|\eta|$ and p_T .

with ≥ 6 jets, and is corrected by applying a correction factor $SF_{i,n} = \epsilon_{i,n}/\epsilon_{i,N}$ where N is the inclusive bin containing all N_{jets} and $\epsilon_{i,n}$ is the QmisID rate obtained from Equation 6.2 in the $(i, n)^{\text{th}}$ 2D bin in (p_T, N_{jets}) . Jet multiplicity and consequently the obtained SFs are assumed to be independent of $|\eta|$.

6.3.3 $t\bar{t}W$ background data-driven estimation

Previously, the $t\bar{t}W$ background in $t\bar{t}t\bar{t}$ final state analyses was handled by assigning large ad-hoc systematic uncertainties to $t\bar{t}W$ events with 7 or more jets [47]. A semi-data-driven method [154] was shown to be effective in the SM $t\bar{t}t\bar{t}$ observation analysis [44] by improving $t\bar{t}W$ modeling, especially in the showering step and switching $t\bar{t}W$ systematic uncertainties from predominantly modeling to statistical.

The data-driven method applies correction factors obtained from a fitted function parameterized in N_{jets} to $t\bar{t}W$ MC kinematic distributions. The QCD scaling patterns [155] can

1482 be represented by ratio of successive exclusive jet cross-sections

$$R_{(n+1)/n} = \frac{\sigma_{n+1}}{\sigma_n} = e^{-b} + \frac{\bar{n}}{n+1} = a_0 + \frac{a_1}{1+(j-4)}, \quad (6.4)$$

1483 where $a_{0(1)}$ and b are constants, n is the number of jets in addition to the hard process, j
1484 is the inclusive number of jets, and \bar{n} is the expectation value for the Poisson distribution
1485 of exclusive jet cross-section at jet multiplicity n . The $t\bar{t}W$ ME for SS2L events gives 4 jets
1486 in the hard process, so n is defined starting from the 5th jets and the inclusive number of
1487 jets $j = n + 4$. The two terms in Equation 6.4 correspond to staircase and Poisson scaling
1488 in cross section between successive jet multiplicities and are sensitive to high and low jet
1489 multiplicity events respectively [155]. The scaling pattern can then be reparameterized in
1490 a_0 and a_1 to obtain the $t\bar{t}W$ yield at $j' \equiv j + 1$ jets

$$\text{Yield}_{t\bar{t}W(j')} = \text{Yield}_{t\bar{t}W(N_{\text{jets}}=4)} \times \prod_{j=4}^{j'-1} \left(a_0 + \frac{a_1}{1+(j-4)} \right) \quad (6.5)$$

1491 with $j \geq 4$. The $t\bar{t}W$ yield in the 4-jet bin can be represented by a NF applied to $t\bar{t}W$ MC
1492 simulation

$$\text{Yield}_{t\bar{t}W(N_{\text{jets}}=4)} = \text{NF}_{t\bar{t}W(N_{\text{jets}}=4)} \times \text{MC}_{t\bar{t}W(N_{\text{jets}}=4)}. \quad (6.6)$$

1493 To account for the asymmetry in $t\bar{t}W^+$ and $t\bar{t}W^-$ cross-sections, $\text{NF}_{t\bar{t}W(N_{\text{jets}}=4)}$ is further
1494 split into $\text{NF}_{t\bar{t}W^\pm(N_{\text{jets}}=4)}$ assuming the scaling is the same for both processes. Both NFs
1495 are left free-floating to constrain $t\bar{t}W$ yields in the 4-jet bin within CR 1b(+) and CR 1b(-).

1496 The final N_{jets} -parameterized function can then be represented by $\text{NF}_{t\bar{t}W(j')}$ as

$$\text{NF}_{t\bar{t}W(j')} = \left(\text{NF}_{t\bar{t}W^+(N_{\text{jets}}=4)} + \text{NF}_{t\bar{t}W^-(N_{\text{jets}}=4)} \right) \times \prod_{j=4}^{j'-1} \left(a_0 + \frac{a_1}{1+(j-4)} \right). \quad (6.7)$$

1497 The normalization is calculated and applied separately for each sub-sample of $t\bar{t}W^+$ and
1498 $t\bar{t}W^-$ in a N_{jets} bin for $4 \leq N_{\text{jets}} < 10$. Due to small contributions in the CRs, events
1499 with $N_{\text{jets}} < 4$ and $N_{\text{jets}} \geq 10$ are not normalized with this scheme. Instead, $N_{\text{jets}} < 4$
1500 events are fitted by propagating the normalization in the 4-jet bin without additional shape
1501 correction. The correction factor for $t\bar{t}W$ events with $N_{\text{jets}} \geq 10$ is obtained by summing
1502 up the overflow from $N_{\text{jets}} = 10$ to $N_{\text{jets}} = 12$, described as $\sum_{j'=10}^{12} \prod_{j=4}^{j'-1} \left(a_0 + \frac{a_1}{1+(j-4)} \right)$.
1503 Events with $N_{\text{jets}} \geq 13$ are negligible and are not included in the sum.

1504 The four regions, CR $t\bar{t}W^\pm$ and CR 1b(\pm), are constructed to fit $\text{NF}_{t\bar{t}W^\pm(N_{\text{jets}}=4)}$ and
1505 the scaling parameters $a_{0(1)}$, as well as validating the parameterization. Assuming the N_{jets}
1506 distribution of $t\bar{t}W$ is similar across bins of N_b -jets, a fitted N_{jets} distribution in CR 1b(\pm)
1507 can be used to describe the $t\bar{t}W$ parameterization at higher N_{jets} .

1508 Chapter 7. Systematic Uncertainties

1509 Physics analysis inherently incurs uncertainties in the form of statistical and systematic
1510 uncertainties, depending on the source. Statistical uncertainties occur in this analysis from
1511 sample size of collected data and simulated MC samples, and from the maximizing of the
1512 LH function. Systematic uncertainties depend on identifiable sources in the analysis i.e.
1513 from detector and reconstruction effects (experimental uncertainties) or theoretical modeling
1514 (theoretical uncertainties). Systematic uncertainties are represented as nuisance parameters
1515 (NP_x) in the profile LH fit. During the fit, systematic uncertainties with negligible impact
1516 on the final results can be pruned to simplify the statistical model and reduce computational
1517 complexity. This section outlines all uncertainties considered in this analysis.

1518 7.1 Experimental uncertainties

1519 7.1.1 Luminosity & pile-up reweighting

1520 The uncertainty on the integrated luminosity of the 2015-2018 Run 2 data set is 0.83%
1521 [89], obtained by the LUCID-2 detector [156] for the primary luminosity measurements and
1522 complemented by the ID and calorimeters. Pile-up was modeled in MC and calibrated
1523 to data through pile-up reweighting, resulting in a set of calibration SFs and associated
1524 uncertainties.

1525 7.1.2 Leptons

1526 In general, calibrating MC simulations to match performance in data incurs uncertainties
1527 associated obtaining the MC-to-data calibration SFs, which are in turn propagated to observ-

ables in the analysis. The data-to-MC calibration of trigger, reconstruction, identification and isolation efficiencies for electrons and muons incur associated uncertainties, with separate systematic and statistical components for those related to muons. Similarly, electron energy scale, muon momentum scale and resolution are also subjected to calibration uncertainties estimated by re-simulating the events while varying the energy/momenta scale and resolution. Electron has an additional uncertainty related to ECIDS efficiency. Muon has additional uncertainties for charge-independent and charge-dependent momentum scale, as well as detector-specific track resolution. Systematic uncertainties for electron reconstruction, identification, isolation, ECIDS efficiencies and muon ID/MS energy resolution were not ready for the sample version used in this analysis, and are therefore not included.

7.1.3 Jets

Experimental uncertainties for jets are dominated by flavor tagging-related uncertainties, with subleading contributions from uncertainties related to JES [112], JER [111] and JVT [157] calibrations.

Jet energy scale

Uncertainties associated with JES are determined using data from LHC collisions along with MC simulated samples [112], decomposed into uncorrelated components:

- **Effective NPs:** 15 total p_T -dependent uncertainty components measured in situ, grouped based on their origin (2 detector-related, 4 modeling-related, 3 mixed, 6 statistical-related)
- **η intercalibration:** 6 total components (1 modeling-related, 4 non-closure and 1

1549 statistical-related) associated with the correction of the forward jets' ($0.8 \leq |\eta| < 4.5$)
1550 energy scale to that of the central jets ($|\eta| < 0.8$).

1551 • **Flavor composition & response:** 2 components for relative quark-gluon flavor com-
1552 positions in background and signal samples, and 2 components for responses to gluon-
1553 initiated versus quark-initiated jets.

1554 • **Pile-up subtraction:** 4 components, 2 for μ (`OffsetMu`) and N_{PV} (`OffsetNPV`) mod-
1555 eling, 1 for residual p_{T} -dependency (`PtTerm`) and 1 for topology dependence on the
1556 per-event p_{T} density modeling (`RhoTopology`).

1557 • **Punch-through effect treatment:** 2 terms for GSC punch-through jet response
1558 deviation between data and MC, one for each detector response simulation method
1559 (AF3 and FS).

1560 • **Non-closure:** 1 term applied to AF3 sample to account for the difference between
1561 AF3 and FS simulation.

1562 • **High- p_{T} single-particle response:** 1 term for the response to high- p_{T} jets from
1563 single-particle and test-beam measurements.

1564 • **b -jets response:** 1 term for the difference between b -jets and light-jets response.

1565 Jet energy resolution

1566 Measurements of JER were performed in bins of p_{T} and η , separately in data using in-
1567 situ techniques and in MC simulation using dijet events [111]. This analysis uses the full
1568 correlation JER uncertainty scheme provided for Run 2 analysis with 14 total components:

₁₅₆₉ 12 for effective NPs and 2 for difference between data and MC, separately for AF3 and FS
₁₅₇₀ [111].

₁₅₇₁ **Jet vertex tagging**

₁₅₇₂ The uncertainty associated with JVT is obtained by varying the JVT efficiency SFs
₁₅₇₃ within their uncertainty range [157]. This uncertainty accounts for remaining contamination
₁₅₇₄ from pile-up jets after applying pile-up suppression and MC generator choice.

₁₅₇₅ **Flavor tagging**

₁₅₇₆ Calibration SFs for b -tagging efficiencies and c -/light-jets mistagging rates are derived as
₁₅₇₇ a function of p_T for b -, c -, light-jets and PCBT score. The full set of flavor tagging-related
₁₅₇₈ uncertainties was reduced in dimensions by diagonalizing the uncertainty covariance matrix
₁₅₇₉ via eigendecomposition [115], resulting in a compact set of orthogonal NPs for this analysis:
₁₅₈₀ 85 for b -jets, 56 for c -jets and 42 for light-jets.

₁₅₈₁ **7.1.4 Missing transverse energy**

₁₅₈₂ Uncertainties on E_T^{miss} arise from possible mis-calibration of the soft-track component
₁₅₈₃ and are estimated using data-to-MC comparison of the p_T scale and resolution between
₁₅₈₄ the hard and soft E_T^{miss} components [119]. These uncertainties are represented by three
₁₅₈₅ independent terms: 1 for scale uncertainty and 2 for resolution uncertainty of the parallel
₁₅₈₆ and perpendicular components.

₁₅₈₇ **7.2 Modeling uncertainties**

₁₅₈₈ **7.2.1 Signal and irreducible background uncertainties**

₁₅₈₉ The signal and background samples used are modeled using MC simulation. Most uncer-
₁₅₉₀ tainties on simulation parameters (e.g. generator choice, PS model) are estimated by varying
₁₅₉₁ the relevant parameters and comparing them with the nominal sample. Uncertainties in-
₁₅₉₂ volving PDF in particular for most processes in the analysis are set to a flat 1% uncertainty.
₁₅₉₃ Cross-section uncertainties were considered for all irreducible background except $t\bar{t}W$, which
₁₅₉₄ is normalized in dedicated CRs following section 6.3.3. Extra uncertainties for the produc-
₁₅₉₅ tion of four or more b -jets (additional b -jets) in association with $t\bar{t}X$ and HF jets were also
₁₅₉₆ considered due to a lack of theoretical predictions or dedicated measurements, rendering
₁₅₉₇ MC modeling challenging. Uncertainties from missing higher-order QCD corrections in MC
₁₅₉₈ simulation are estimated by varying the renormalization scale μ_R and factorization scale μ_F
₁₅₉₉ within seven different combinations

$$(\mu_R, \mu_F) = \{(0.5, 0.5), (0.5, 1), (1, 0.5), (1, 1), (1, 2), (2, 1), (2, 2)\}.$$

₁₆₀₀ Process-specific uncertainty treatments are detailed below.

₁₆₀₁ **SM $t\bar{t}t\bar{t}$ background**

₁₆₀₂ The generator uncertainty for the SM $t\bar{t}t\bar{t}$ background was evaluated between a nominal
₁₆₀₃ sample of MADGRAPH5_AMC@NLO and SHERPA. The parton shower uncertainty was
₁₆₀₄ evaluated between PYTHIA8 and HERWIG. The cross-section uncertainty was estimated to

1605 be 20% computed from a prediction at NLO in QCD+EW [128].

1606 $t\bar{t}t$ background

1607 The cross-section uncertainty for $t\bar{t}t$ was estimated to be 30% computed from a prediction
1608 at NLO in QCD+EW [128]. Events with additional b -jets also incur a 50% uncertainty.

1609 $t\bar{t}W$, $t\bar{t}Z$, $t\bar{t}H$ backgrounds

1610 For $t\bar{t}W$, $t\bar{t}Z$ and $t\bar{t}H$ backgrounds, an uncertainty of 50% is assigned to events with one
1611 additional truth b -jets that did not originate from a top quark decay, and an added 50%
1612 uncertainty is assigned to events with two or more [158] additional b -jets. The generator
1613 uncertainty was estimated for $t\bar{t}Z$ using a MADGRAPH5_AMC@NLO nominal sample and
1614 a SHERPA sample, and for $t\bar{t}H$ using POWHEGBOX samples interfaced with PYTHIA8 (nom-
1615 inal) and HERWIG7. Cross-section uncertainties of 12% and 10% were applied to $t\bar{t}Z$ and
1616 $t\bar{t}H$ respectively [159]. No $t\bar{t}W$ cross-section or PDF uncertainty was considered since the
1617 normalizations and jet multiplicity spectrum for $t\bar{t}W$ are estimated using the data-driven
1618 method described in section 6.3.3.

1619 Other backgrounds

1620 Other backgrounds include processes with small overall contribution in the SR. The
1621 cross-section uncertainty for tZ and tWH is considered to be 30% [160, 161]. A conservative
1622 cross-section uncertainty of 50% is applied to $t\bar{t}VV$, VVV and VH . For VV , the cross-
1623 section uncertainty is dependent on jet multiplicity and is considered to be 20%/50%/60%
1624 for events with $\leq 3/4 \geq 5$ jets [162]. For VV , $t\bar{t}VV$, VVV and VH events with additional
1625 truth b -jets, an uncertainty of 50% is applied.

1626 7.2.2 Reducible background uncertainties

1627 Reducible backgrounds consist of $t\bar{t}/V + \text{HF}$ jets and single top events. Reducible back-
1628 ground has small contamination within the SR, thus uncertainties related to reducible back-
1629 ground have minor impact. Treatment for reducible background in this analysis largely
1630 follows Ref. [44], except for QmisID.

1631 Charge misidentification

1632 Uncertainties on the QmisID background originate from the charge flip rates obtained
1633 using the data-driven method described in section 6.3.2. Four sources of uncertainty were
1634 considered: statistical uncertainty from the maximum LLH estimation using Equation 6.2;
1635 uncertainty from choice of the Z -mass window and sidebands; non-closure uncertainty de-
1636 fined as the relative difference between the number of SS and OS events; and statistical
1637 uncertainty from the N_{jets} dependency correction SFs. The combined uncertainties from
1638 all four sources are calculated separately for each region involved in section 6.3.2, and are
1639 treated as correlated across all regions. Figure 7.1 shows the uncertainty calculated for SR.

1640 Internal (low γ^*) and material conversion

1641 The normalization for internal and material conversion backgrounds are free parameters
1642 in the fit, as a result the only uncertainties evaluated are from the shape of the distributions
1643 used in the template fit method (see section 6.3.1). The uncertainties on internal (material)
1644 conversion are estimated based on the difference between data and MC prediction in a region
1645 enriched in $Z + \gamma \rightarrow \mu^+\mu^- + e^+e^-$ events.

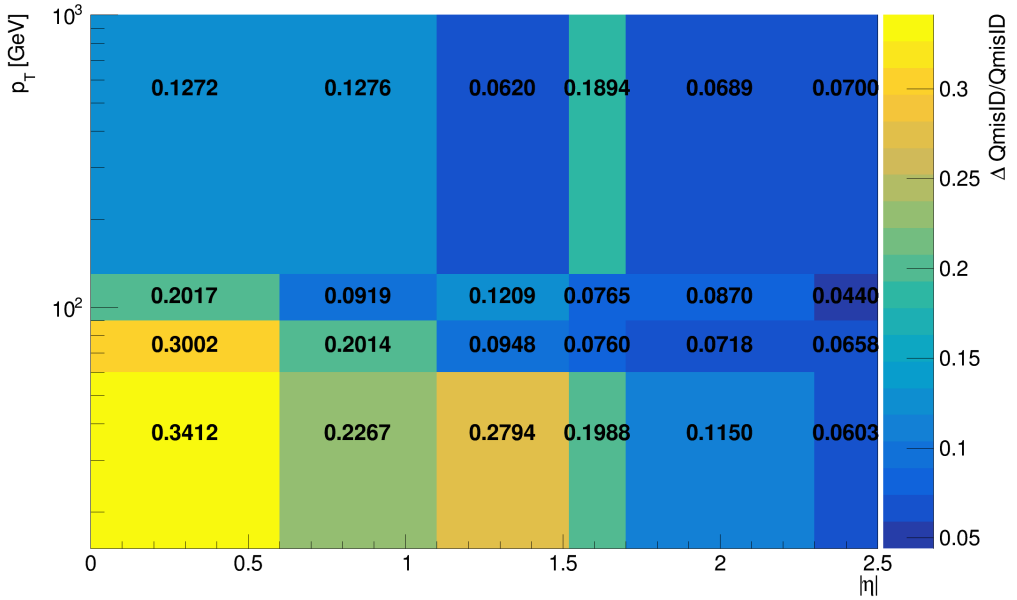


Figure 7.1: Combined QmisID uncertainty rate for SR in bins of $|\eta|$ and p_T .

1646 Heavy-flavor non-prompt lepton

1647 Similar to the conversion backgrounds, the uncertainties on non-prompt HF decays come
1648 from the shape of the distributions, and are estimated by comparing data and MC prediction
1649 between all regions in the analysis on a per bin basis. The events used are required to
1650 contain at least one *Loose* reconstructed lepton used in the region selection criteria detailed
1651 in Table 6.1 to maintain orthogonality with the SR.

1652 Light-flavor decays and other fake/non-prompt backgrounds

1653 A conservative normalization uncertainty of 100% is assigned for light-flavor non-prompt
1654 lepton background [151], and an ad-hoc normalization uncertainty of 30% is applied to all
1655 other fake and non-prompt backgrounds. The shape uncertainties for these backgrounds are
1656 negligible.

1657 **Chapter 8. Results**

1658 **8.1 Statistical interpretation**

1659 This section provides an overview of the statistical methods needed to interpret the
1660 collected and simulated data to estimate unknown physics parameters and determine com-
1661 patibility between data and the analysis hypothesis. For the BSM resonance search, the null
1662 hypothesis H_0 assumes only SM background contributions and none from any new BSM
1663 resonance in the data.

1664 **8.1.1 Profile likelihood fit**

1665 Given a set of observed data points $\mathbf{x} = [x_1, x_2, \dots]$ and unknown parameters $\boldsymbol{\theta} =$
1666 $[\theta_1, \theta_2, \dots, \theta_n]$, the maximum likelihood method aims to find an estimate $\hat{\boldsymbol{\theta}}$ that maximizes
1667 the joint probability function $f(\mathbf{x}, \boldsymbol{\theta})$, or in other words the set of parameters that gives the
1668 highest probability of observing the collected data points for a particular model. The func-
1669 tion to be maximized for this purpose is the log-likelihood (LLH) function $\ln \mathcal{L}(\mathbf{x}, \boldsymbol{\theta})$ where
1670 $\mathcal{L}(\mathbf{x}, \boldsymbol{\theta}) \equiv \prod_i f(x_i, \boldsymbol{\theta})$ is defined as the likelihood (LH) function. The LLH is maximized
1671 when $\partial/\partial\theta_i (\ln \mathcal{L}) = 0$ for each parameter θ_i .

1672 For an usual binned physics analysis, the above variables for the LH function \mathcal{L} can
1673 be expressed as nuisance parameters (NP) $\boldsymbol{\theta}$ and number of events for a model $N_i(\mu)$ for
1674 the i^{th} bin, where μ is the targeted parameter of interest (POI). In this analysis, N_i is
1675 assumed to follow a Poisson distribution and depends on the following quantities: the signal
1676 strength μ defined as the ratio of observed to expected cross sections $\sigma_{\text{obs}}/\sigma_{\text{exp}}$; nuisance
1677 parameters $\boldsymbol{\theta}$ which represents the effects of systematic uncertainties, implemented in the

1678 LH function as Gaussian constraints; and normalization factors (NFs) $\boldsymbol{\lambda}$ that control the
 1679 normalization of background components that do not have a well-known cross section. The
 1680 Poisson probability of observing exactly N_i events for an expected number of event n_i is

$$\mathcal{P}(N_i|n_i(\mu, \boldsymbol{\lambda})) = \frac{n_i^{N_i} e^{-n_i}}{N_i!}. \quad (8.1)$$

1681 The expected Poisson event number in a bin i can be parameterized as

$$n_i = \mu s_i(\boldsymbol{\theta}) + \sum_j \lambda_j b_{ij}(\boldsymbol{\theta}), \quad (8.2)$$

1682 where s_i is the number of signal events in bin i of every region, and b_{ij} is the number of
 1683 events for a certain background source index j in bin i . The LH function in this analysis
 1684 can be written as

$$\mathcal{L}(\mathbf{N}|\mu, \boldsymbol{\theta}, \boldsymbol{\lambda}) = \left(\prod_i \mathcal{P}(N_i|n_i) \right) \cdot \prod_k \mathcal{G}(\theta_k), \quad (8.3)$$

1685 where $\mathcal{G}(\theta_k)$ is the Gaussian constraint for a NP k . The signal significance μ and NFs $\boldsymbol{\lambda}$ are
 1686 left unconstrained and are fitted simultaneously in the profile LH fit. Define the profile LH
 1687 ratio [163] as

$$\lambda(\mu) = \frac{\mathcal{L}(\mu, \hat{\boldsymbol{\theta}}_\mu, \hat{\boldsymbol{\lambda}}_\mu)}{\mathcal{L}(\hat{\mu}, \hat{\boldsymbol{\theta}}, \hat{\boldsymbol{\lambda}})}, \quad (8.4)$$

1688 where $\hat{\mu}$, $\hat{\boldsymbol{\theta}}$ and $\hat{\boldsymbol{\lambda}}$ are parameter values that optimally maximizes the LH function, and $\hat{\boldsymbol{\theta}}_\mu$,
 1689 $\hat{\boldsymbol{\lambda}}_\mu$ are NP and NF values respectively that maximize the LH function for a given signal
 1690 strength μ . Using Neyman-Pearson lemma [164], the optimal test statistic for hypothesis
 1691 testing is

$$q_\mu \equiv -2 \ln \lambda(\mu), \quad (8.5)$$

1692 where $q_\mu = 0$ or $\lambda(\mu) = 1$ corresponds to perfect agreement between the optimal parameter
 1693 $\hat{\mu}$ obtained from data and the hypothesized value μ . From Wilks' theorem [165], the test
 1694 statistic q_μ approaches a χ^2 distribution and can be evaluated as $q_\mu = (\mu - \hat{\mu})^2 / \sigma_\mu^2$.

1695 When evaluating against the background-only hypothesis ($\mu = 0$), it can be assumed
 1696 that the number of events observed under the signal hypothesis is higher than that of the
 1697 background-only hypothesis, or $\mu \geq 0$ according to Equation 8.2. This leads to a corre-
 1698 sponding lower bound on the test statistic

$$q_0 = \begin{cases} -2 \ln \lambda(0), & \text{if } \hat{\mu} \geq 0, \\ 0, & \text{if } \hat{\mu} < 0. \end{cases} \quad (8.6)$$

1699 ***p*-value**

1700 To quantify the incompatibility between the observed data and the background-only hy-
 1701 pothesis, the *p*-value is defined as $p = P(q_\mu \geq q_{\mu, \text{obs}} | H_0)$ or in other words, the probability
 1702 of observing data with a test statistic q_μ under the null hypothesis H_0 that is less compat-
 1703 ible with H_0 than the actual observed data with test statistic $q_{\mu, \text{obs}}$. The *p*-value can be
 1704 expressed in terms of q_μ as

$$p_\mu = \int_{q_{\mu, \text{obs}}}^{\infty} f(q_\mu | \mu) dq_\mu, \quad (8.7)$$

1705 where $f(q_\mu | \mu) dq_\mu$ is the conditional probability density function of q_μ given μ .

1706 In some cases, it is more convenient to evaluate compatibility using the *Z*-value, defined
 1707 as the number of standard deviations between the observed data and the mean in a Gaussian

1708 distribution. The p -value can be converted to Z -value via the relation

$$Z = \Phi^{-1}(1 - p), \quad (8.8)$$

1709 where Φ is the quantile of the standard Gaussian. Rejecting the signal hypothesis usually
1710 requires a 95% confidence level (CL) which corresponds to a p -value of 0.05 or a Z -value of
1711 1.64, while rejecting the background-only hypothesis generally requires a Z -value of 5 or a
1712 p -value of 2.84×10^{-7} .

1713 8.1.2 Exclusion limit

1714 If the signal hypothesis is rejected, the exclusion upper limits can still be computed at
1715 a certain CL (usually 95%) to establish the maximum value of μ that is not excluded by
1716 or in conflict with the observed data. The exclusion limits are calculated based on the CLs
1717 method [166, 167] under which the test statistic is defined as $q_\mu = -2 \ln \frac{\mathcal{L}_{s+b}}{\mathcal{L}_b}$ with \mathcal{L}_{s+b}
1718 being the LH function for the signal and background hypothesis ($\mu > 0$) and \mathcal{L}_b being the
1719 LH function for the background-only hypothesis ($\mu = 0$). The p -value for both hypotheses
1720 can then be expressed as

$$\begin{aligned} p_{s+b} &= P(q \geq q_{\text{obs}} | s + b) = \int_{q_{\text{obs}}}^{\infty} f(q | s + b) dq \\ p_b &= P(q \geq q_{\text{obs}} | b) = \int_{-\infty}^{q_{\text{obs}}} f(q | b) dq. \end{aligned} \quad (8.9)$$

1721 The signal hypothesis is excluded for a CL α when the following condition is satisfied

$$\text{CL}_s \equiv \frac{p_{s+b}}{p_b} \geq 1 - \alpha. \quad (8.10)$$

1722 The value of μ such that the signal hypothesis leads to $CL_s = 1 - \alpha = 0.05$ is then the
 1723 exclusion upper limit at a 95% CL. Exclusion limits are usually reported in terms of expected
 1724 and observed limits. The expected limits show the exclusion limits obtained under the
 1725 background-only hypothesis and represent the analysis' sensitivity, while the observed limits
 1726 represent exclusion limits derived from observed data.

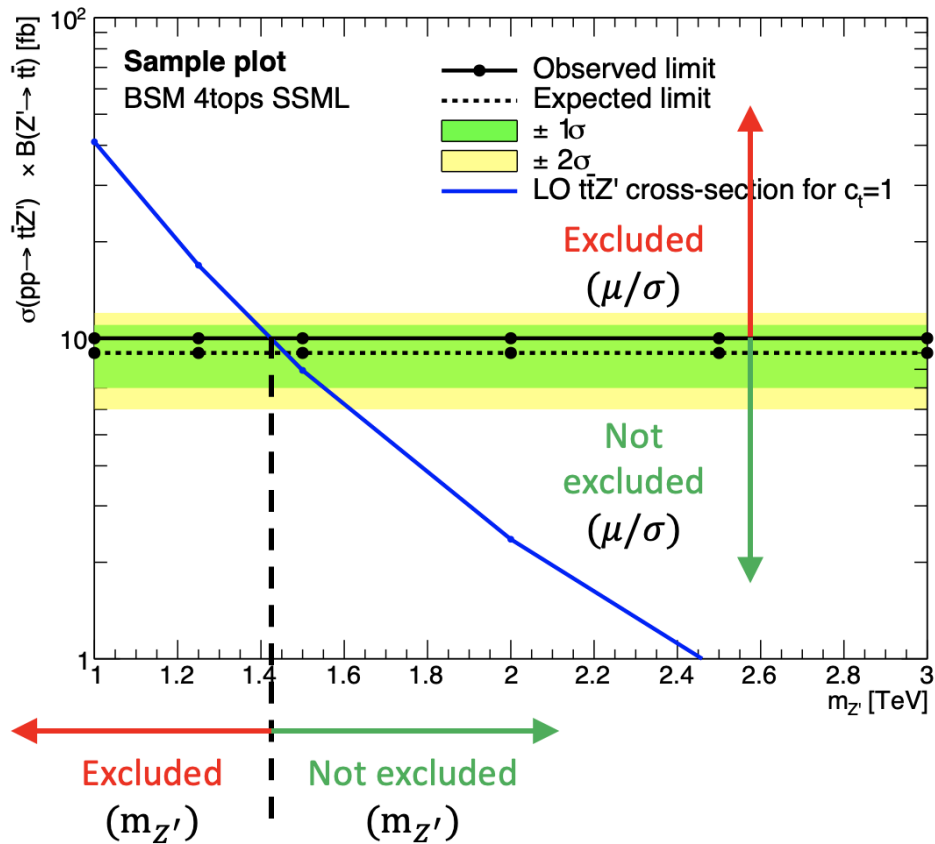


Figure 8.1: Example of an exclusion limit graph. The solid (dotted) line represents the observed (expected) upper limits as a function of the Z' mass at 95% CL on the cross-section of $pp \rightarrow t\bar{t}Z'$ production times the $Z' \rightarrow t\bar{t}$ branching ratio. The solid blue line represents the theoretical signal cross-section with $c_t = 1$ at LO in QCD [74]. The green and yellow bands represent the 68% ($\pm 1\sigma$) and 95% ($\pm 2\sigma$) confidence intervals for the expected upper limits. Cross section of $t\bar{t}Z'$ within the region above the observed limit is excluded under the current model. Masses below the $m_{Z'}$ value at which the observed limit intersect the theoretical cross section are excluded.

1727 In a search for an exotic particle of unknown mass, a lower bound on the mass can

1728 be determined using the theoretical cross section for the particle and the obtained observed
1729 limits. Figure 8.1 shows a sample exclusion limit graph of the $t\bar{t}Z'$ cross section as a function
1730 of the Z' mass. Values of the signal strength μ (and by proxy the cross section σ via $\mu =$
1731 $\sigma/\sigma_{\text{theory}}$) above the observed limits are incompatible with the analysis model. Consequently,
1732 mass points with a smaller observed cross section than the theoretical cross section are
1733 excluded from the model; the cross section for the particle predicted by the analysis model
1734 lies in the exclusion region obtained using observed data. Such masses are eliminated as a
1735 possibility for the model.

1736 8.2 Fit results

1737 The signal strength μ , background NFs, $t\bar{t}W$ scaling factors and uncertainty NPs are
1738 simultaneously fitted using a binned profile LLH fit under the background-only hypothesis
1739 to the H_T distribution in the SR and to corresponding distributions shown in Table 6.1 for
1740 CRs.

1741 Before fitting to real data (unblinded fit), the fit was first performed in both the SR
1742 and CRs using Asimov pseudo-datasets, in which the simulated data match exactly to MC
1743 prediction with nominal μ set to 0. This is done for the purpose of optimizing object selection
1744 criteria and region definition, refining background estimation techniques and testing the
1745 statistical interpretation model for signal extraction described in section 8.1. The fit is then
1746 performed with Asimov data in the SR and real data in CRs to validate background modeling,
1747 estimate sensitivity and assess the influence of statistical effects on fitted parameters. Finally,
1748 the fully unblinded fit is performed with real data in all regions.

1749 The unblinded fit results are presented below. No significant variation is observed in fit

1750 output behavior using $t\bar{t}Z'$ samples of different $m_{Z'}$; results fitted using $m_{Z'} = 2$ TeV are
1751 shown without substantial loss of generality. The background modeling is evaluated under
1752 the background-only hypothesis. The fitted background NFs are shown in Table 8.1 and
1753 are consistent with their nominal values within one standard deviation, or two standard
1754 deviations in the case of $\text{NF}_{\text{HF } e}$ and $\text{NF}_{t\bar{t}W^+(4j)}$. Figure 8.2 shows good agreement between
1755 data and post-fit background distributions in non-prompt background CRs and $t\bar{t}W$ CRs.

1756 The pre-fit and post-fit background yields are shown in Table 8.2. Except for HF e
1757 background, post-fit yields for various backgrounds e.g. $t\bar{t}t\bar{t}$, $t\bar{t}H$, other fake, etc. are
1758 increased; the pre-fit to post-fit variations are consistent within $\pm\sigma$. Post-fit yield for HF e
1759 background is lowered compared to pre-fit yield within 2σ which can be related to the fitted
1760 value of $\text{NF}_{\text{HF } e}$ in Table 8.1; however, this difference in pre- and post-fit yields of HF e
1761 background has negligible impact on the μ as seen in Table 8.3. Post-fit yields for signal are
1762 consistent with zero within $\pm 2\sigma$. Data and total post-fit yields are consistent within $\pm 1\sigma$.

1763 Table 8.3 outlines the impact on the signal strength μ of various sources of uncertainty
1764 grouped by their corresponding category. The background sources of uncertainty with the
1765 largest impact is $t\bar{t}t\bar{t}$ modeling, in particular $t\bar{t}t\bar{t}$ generator choice and cross-section uncer-
1766 tainties, followed by $t\bar{t}W$ modeling due to their significant contributions in the SR observed
1767 in Figure 6.1, especially in the more sensitive regions requiring three or more b -tagged jets.
1768 The most significant impact on μ within the set of instrumental uncertainties are uncertain-
1769 ties on jet b -tagging attributable to the high jet and b -jet multiplicities in the BSM $t\bar{t}t\bar{t}$ signal
1770 signature.

1771 Figure 8.4 shows the post-fit pull from the nominal pre-fit value for each nuisance param-
1772 eter. Pull for all NPs are consistent within one standard deviation from the nominal pre-fit
1773 value. Overall, modeling uncertainties suffer from more significant pull compared to experi-

1774 mental uncertainties. Uncertainty sources with the largest pull are SM $t\bar{t}t\bar{t}$ cross section and
 1775 generator choice, along with $t\bar{t}Z$ generator choice and diboson cross section. Additionally, no
 1776 significant constraints are placed on NPs by the fit to data, with the exception of moderate
 1777 constraint on the diboson cross section.

1778 No significant excess over SM predictions is observed, and the fitted signal strength μ is
 1779 compatible with zero for all Z' mass points. Figure 8.5 shows the observed and expected
 1780 upper limits at 95% confidence level on the cross-section of $pp \rightarrow t\bar{t}Z'$ production times
 1781 the branching ratio of $Z' \rightarrow t\bar{t}$ as a function of the Z' resonance mass. The $\pm 1\sigma$ and $\pm 2\sigma$
 1782 confidence intervals around the expected exclusion limits are also shown. The observed
 1783 exclusion limits range from 7.9 fb to 9.44 fb depending on $m_{Z'}$. The distribution of limits
 1784 across $m_{Z'}$ is flat and show little correlation to signal kinematics and phase space modeling.
 1785 The observed limits exclude Z' masses below ≈ 15 TeV.

Table 8.1: Normalization factors for backgrounds with dedicated CRs, obtained from a simultaneous fit in all CRs and SR under the background-only hypothesis. The nominal pre-fit value is 1 for all NFs and 0 for the scaling factors a_0 and a_1 . Uncertainties shown include both statistical and systematic uncertainties.

Parameter	NF _{HF e}	NF _{HF μ}	NF _{Mat. Conv.}	NF _{Low m_{γ^*}}	a_0	a_1	NF _{$t\bar{t}W^+(4j)$}	NF _{$t\bar{t}W^-(4j)$}
Fit value	$0.68^{+0.23}_{-0.22}$	$0.97^{+0.17}_{-0.16}$	$0.97^{+0.31}_{-0.28}$	$0.97^{+0.23}_{-0.20}$	$0.39^{+0.11}_{-0.11}$	$0.42^{+0.25}_{-0.24}$	$1.21^{+0.18}_{-0.18}$	$1.10^{+0.26}_{-0.26}$

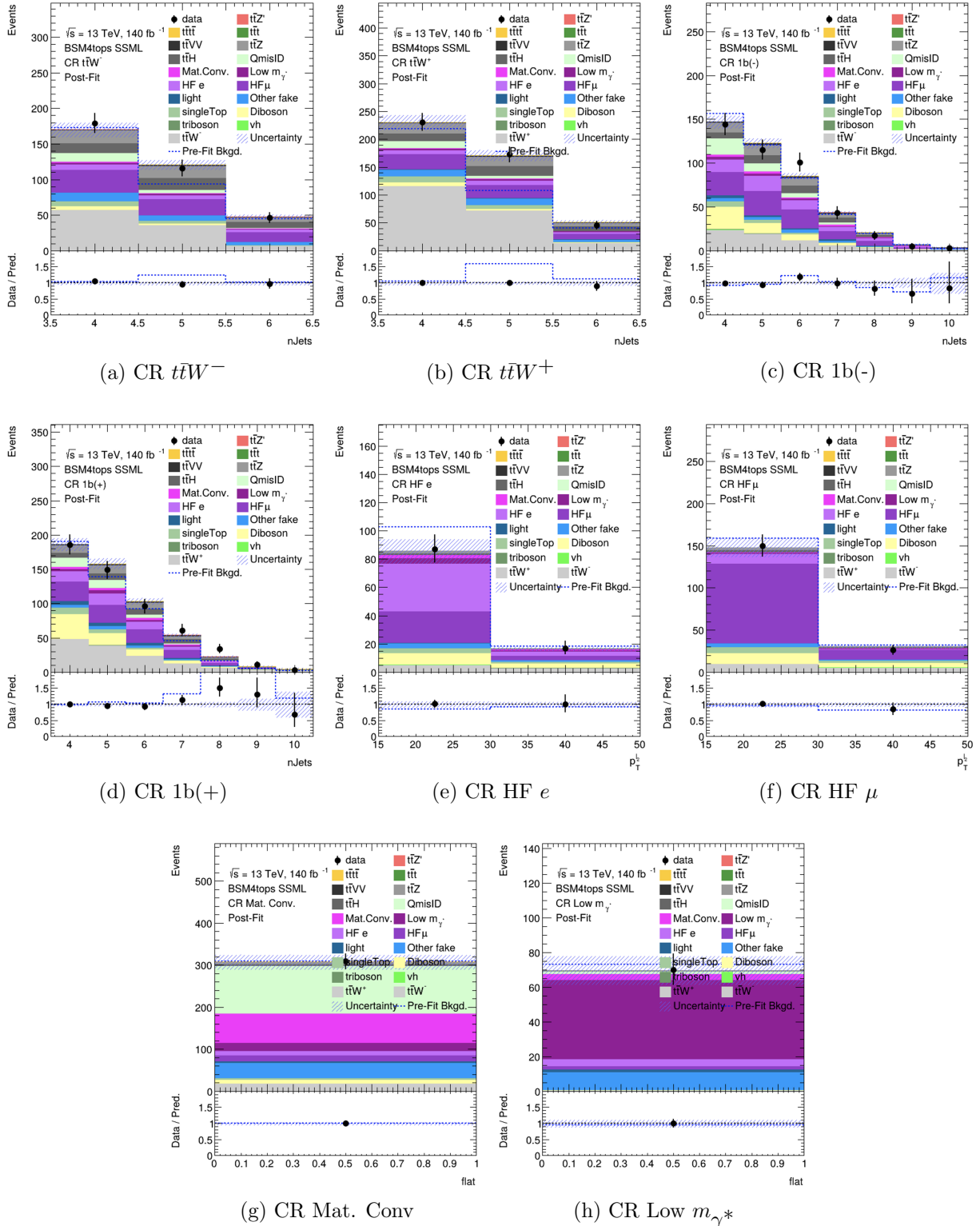
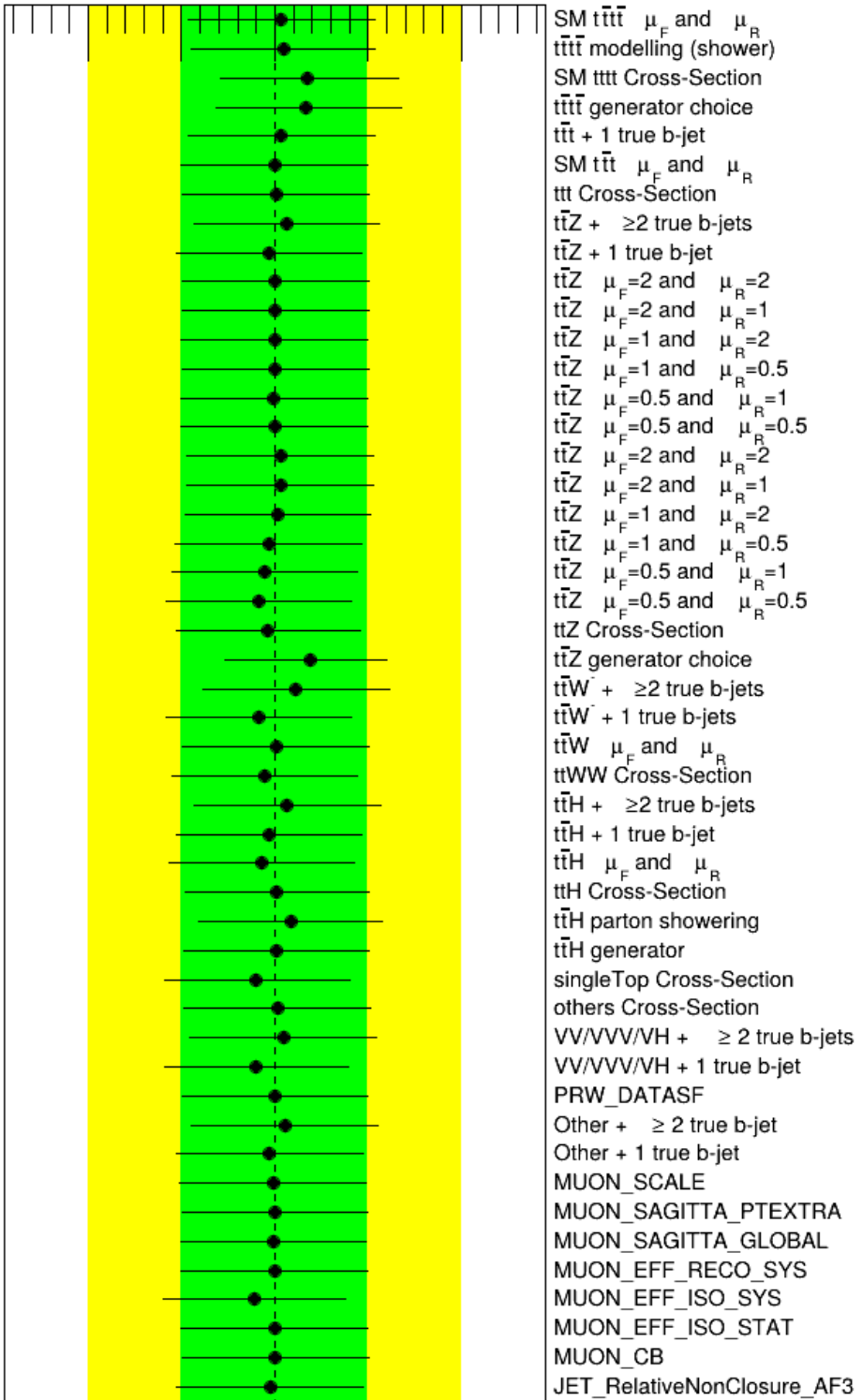
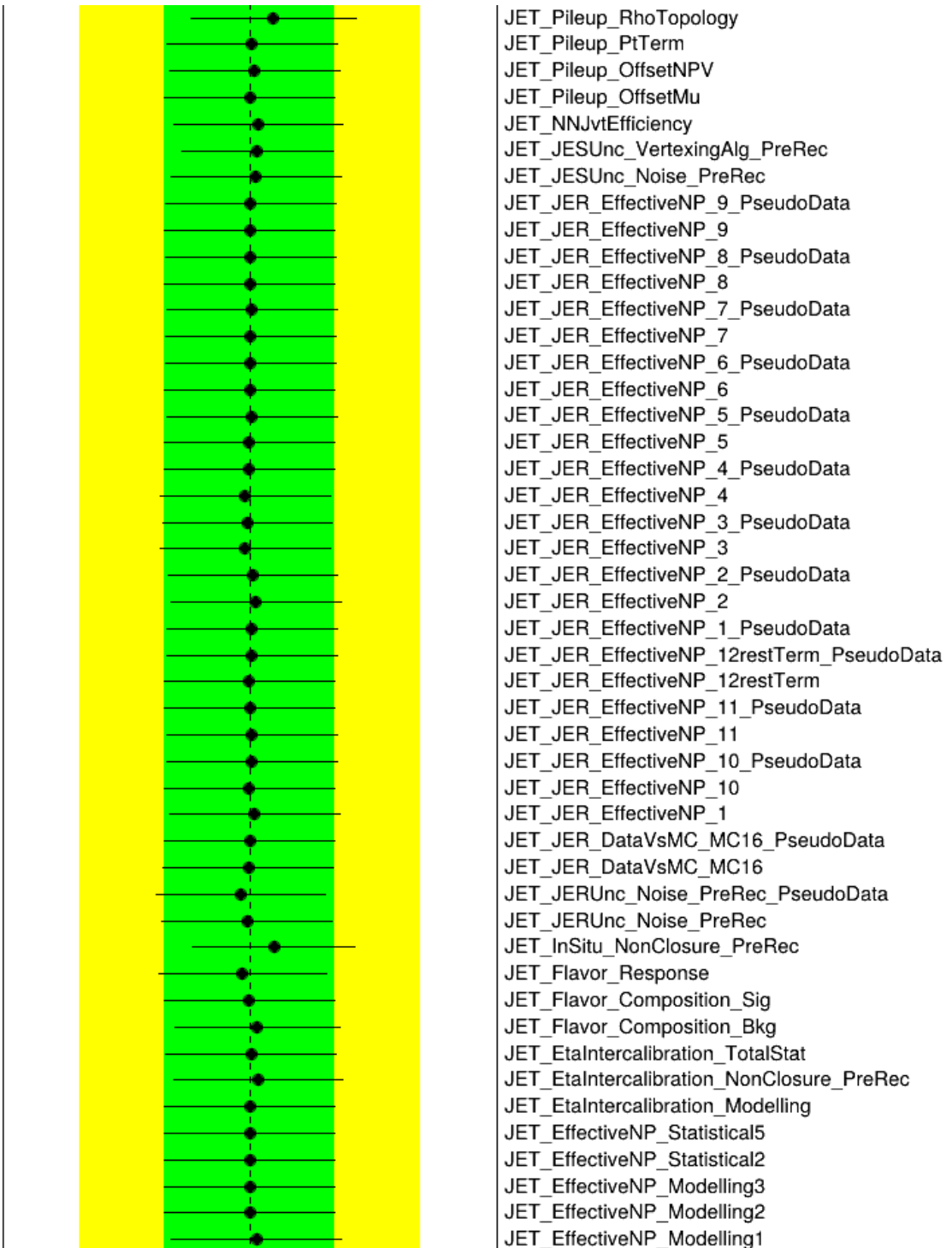


Figure 8.2: Comparison between data and post-fit prediction for the discriminant observable in each CR. Distributions shown are obtained from the fit using the $t\bar{t}Z'$ signal sample with $m_{Z'} = 2$ TeV. The lower panel shows the ratio between data and post-fit predictions. The shaded band represents the total uncertainty on the fit. The dashed line represents the pre-fit distribution.





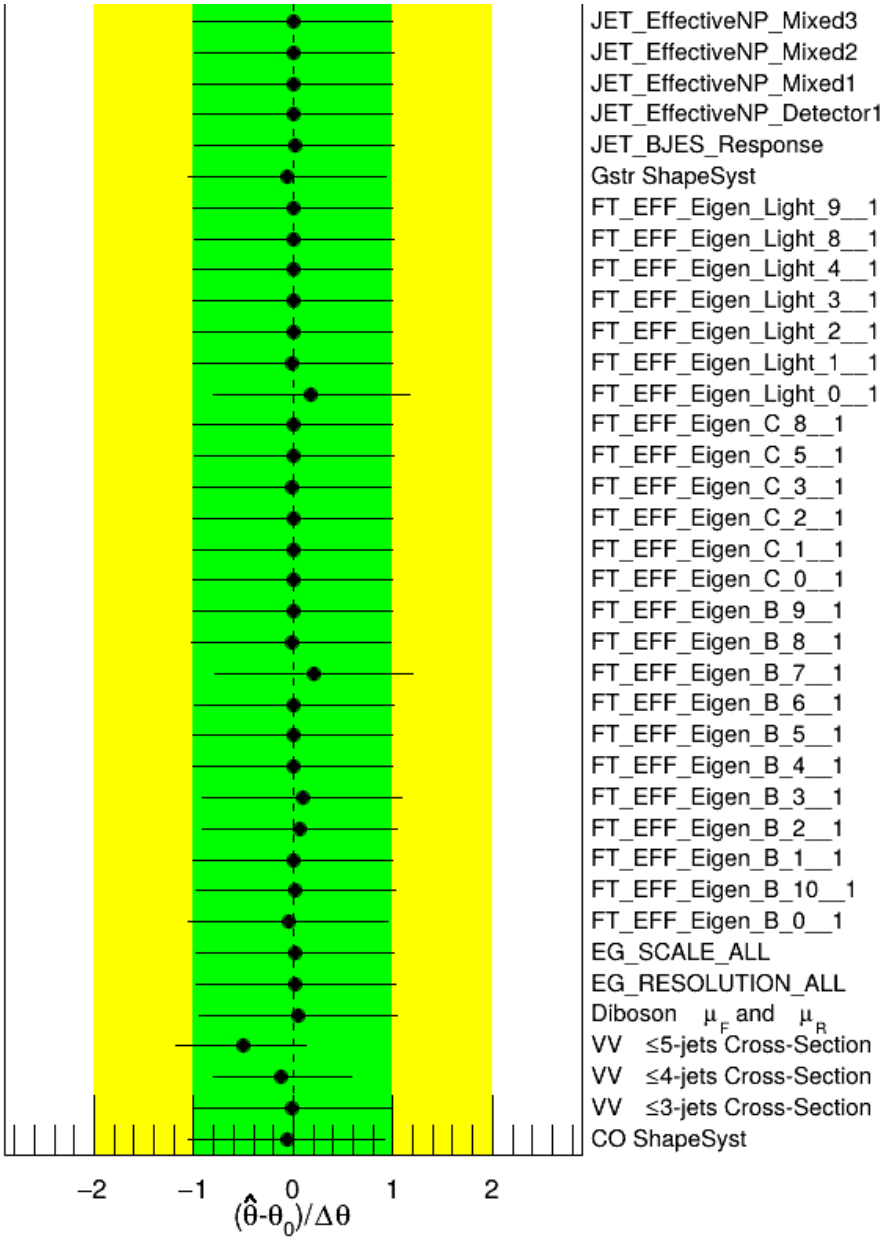


Figure 8.4: Post-fit pull from nominal values for nuisance parameters representing systematic uncertainties. Systematics pruned during the fit are not shown. The dashed line represents the nominal pre-fit values. The green and yellow bands represent the 68% ($\pm 1\sigma$) and 95% ($\pm 2\sigma$) confidence intervals for the nominal fit value.

Table 8.2: Pre-fit and post-fit background yields in the inclusive SR. The number of data events and pre-fit estimate signal yields are also shown. Background yields shown are obtained using the $t\bar{t}Z'$ signal sample with $m_{Z'} = 2$ TeV. Total yield uncertainty differs from the quadrature sum of constituent uncertainties due to (anti-)correlation effects.

[†]Pre-fit yields for $t\bar{t}W$ background are nominally set to 0 prior to data-driven normalization. Yields shown are estimated using best fit parameters.

Process	Pre-fit	Post-fit
Background		
$t\bar{t}t\bar{t}$	42.35 ± 9.57	46.80 ± 9.75
$t\bar{t}W^+$	$97.38 \pm 0.71^\dagger$	104.36 ± 19.44
$t\bar{t}W^-$	$56.92 \pm 0.42^\dagger$	55.36 ± 13.88
$t\bar{t}Z$	78.02 ± 19.24	71.51 ± 15.29
$t\bar{t}H$	81.00 ± 9.91	83.16 ± 9.76
$t\bar{t}t$	3.33 ± 1.03	3.36 ± 1.04
Single-top (tq , tZq , tWZ , etc.)	13.38 ± 4.08	12.70 ± 4.01
$t\bar{t}VV/t\bar{t}VH/t\bar{t}HH$	17.07 ± 6.75	16.42 ± 6.66
Charge misidentification	40.31 ± 0.32	40.31 ± 0.00
$VV/VVV/VH$	10.01 ± 6.27	6.72 ± 3.62
Mat. Conv.	26.20 ± 0.95	25.72 ± 7.88
Low m_{γ^*}	26.14 ± 0.74	25.51 ± 5.61
HF e	21.99 ± 2.02	15.37 ± 5.01
HF μ	31.33 ± 3.96	31.41 ± 6.07
Light-flavor decays	13.47 ± 0.55	13.51 ± 0.53
Other fake & non-prompt	24.90 ± 2.73	26.01 ± 2.35
Total background	$583.77 \pm 32.02^\dagger$	578.23 ± 27.11
Signal $t\bar{t}Z' \rightarrow t\bar{t}t\bar{t}$		
$m_{Z'} = 1$ TeV	52.83 ± 2.75	26.96 ± 16.31
$m_{Z'} = 1.25$ TeV	52.94 ± 2.72	25.02 ± 15.45
$m_{Z'} = 1.5$ TeV	53.07 ± 2.78	24.55 ± 15.07
$m_{Z'} = 2$ TeV	52.49 ± 2.76	24.52 ± 14.91
$m_{Z'} = 2.5$ TeV	53.07 ± 2.78	25.35 ± 15.20
$m_{Z'} = 3$ TeV	52.45 ± 2.80	25.64 ± 15.26
Data	604	

Table 8.3: Post-fit impact of uncertainty sources on the signal strength μ , grouped by categories. Values shown are obtained from the fit using the $t\bar{t}Z'$ signal sample with $m_{Z'} = 2$ TeV. Impact on μ is evaluated for each uncertainty category by re-fitting with the corresponding set of NPs fixed to their best-fit values. Total uncertainty differs from the quadrature sum of constituent uncertainties due to correlation between NPs in the fit.

Uncertainty source	$\Delta\mu$	
Signal modeling		
$t\bar{t}Z'$	+0.00	-0.00
Background modeling		
$t\bar{t}\bar{t}$	+0.15	-0.13
$t\bar{t}W$	+0.04	-0.03
$t\bar{t}Z$	+0.02	-0.02
$t\bar{t}H$	+0.02	-0.02
Non-prompt leptons	+0.00	-0.00
Other backgrounds	+0.02	-0.02
Instrumental		
Luminosity	+0.00	-0.00
Jet uncertainties	+0.04	-0.04
Jet flavor tagging (b -jets)	+0.04	-0.04
Jet flavor tagging (c -jets)	+0.01	-0.01
Jet flavor tagging (light-jets)	+0.02	-0.01
MC simulation sample size	+0.01	-0.01
Other experimental uncertainties	+0.01	-0.01
Total systematic uncertainty	+0.15	-0.17
Statistical		
$t\bar{t}W$ NFs and scaling factors	+0.01	-0.01
Non-prompt lepton NFs (HF, Mat. Conv., Low m_{γ^*})	+0.00	-0.00
Total statistical uncertainty	+0.25	-0.23
Total uncertainty	+0.29	-0.29

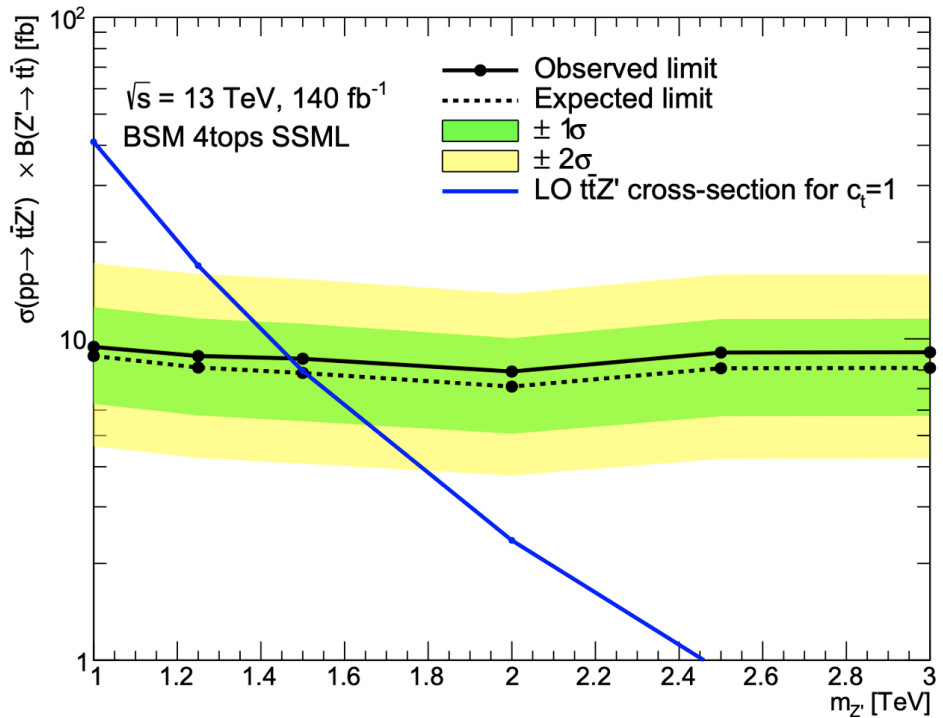


Figure 8.5: Observed (solid line) and expected (dotted line) upper limits as a function of the Z' mass at 95% CL on the cross-section of $pp \rightarrow t\bar{t}Z'$ production times the $Z' \rightarrow t\bar{t}$ branching ratio. The region above the observed limit is excluded. The solid blue line represents the theoretical signal cross-section with $c_t = 1$ at LO in QCD [74]. The green and yellow bands represent the 68% ($\pm 1\sigma$) and 95% ($\pm 2\sigma$) confidence intervals for the expected upper limits.

1786 Chapter 9. Summary

1787 This dissertation presents a search for BSM top-philic heavy vector resonance based on a
1788 simplified top-philic color singlet $Z'(\rightarrow t\bar{t})$ model in the top-quark pair associated production
1789 channel ($t\bar{t}Z'$). The search is performed in the same-sign dilepton and multilepton channel
1790 of the $t\bar{t}t\bar{t}$ final states, using the full Run 2 data set collected between 2015 and 2018 by the
1791 ATLAS detector at the LHC, corresponding to an integrated luminosity of 140 fb^{-1} of pp
1792 collisions at center-of-mass energy $\sqrt{s} = 13 \text{ TeV}$.

1793 New data-driven estimation methods for $t\bar{t}W$ and charge misidentification background
1794 are employed to improve background modeling and signal sensitivity compared to previous
1795 analysis [28]. No significant excess over Standard Model predictions is observed. Observed
1796 exclusion limits at 95% confidence level as a function of the Z' mass are set on the production
1797 cross section of $pp \rightarrow t\bar{t}Z'$ times the $Z' \rightarrow t\bar{t}$ branching ratio, ranging from 7.9 fb (at $m_{Z'} = 2$
1798 TeV) to 9.4 fb (at $m_{Z'} = 1 \text{ TeV}$) depending on the Z' mass. This represent a significant
1799 improvement in the exclusion limit for $t\bar{t}Z'$ [28], and are currently the most stringent upper
1800 limits to date. The analysis probes a Z' mass range from 1 TeV to 3 TeV under the
1801 assumption of a top- Z' coupling strength of $c_t = 1$ and chirality angle $\theta = \pi/4$.

1802 Further improvements in analysis strategies, including multivariate techniques for signal
1803 discrimination, are expected to increase discovery potential in future searches. Looking
1804 forward, the upcoming Run 3 data at $\sqrt{s} = 13.6 \text{ TeV}$ will increase the total integrated
1805 luminosity by about a factor of 2 [169] and the $pp \rightarrow t\bar{t}t\bar{t}$ cross section by at least 19% [168],
1806 which will help to improve modeling for the SM $t\bar{t}t\bar{t}$ background. Run 3 improvements along
1807 with prospects of the High-Luminosity LHC will enhance sensitivity to BSM physics and offer
1808 more opportunities to explore top-philic resonances and other exciting new phenomena.

1809 References

- 1810 [1] J. Schwinger. *On Quantum-Electrodynamics and the Magnetic Moment of the Elec-*
tron. *Phys. Rev.* **73** (4 1948), pp. 416–417 (cit. on p. 1).
- 1811
1812 [2] R. P. Feynman. *Space-Time Approach to Quantum Electrodynamics.* *Phys. Rev.* **76**
1813 (6 1949), pp. 769–789 (cit. on p. 1).
- 1814 [3] S. Tomonaga. *On a relativistically invariant formulation of the quantum theory of*
1815 *wave fields.* *Prog. Theor. Phys.* **1** (1946), pp. 27–42 (cit. on p. 1).
- 1816 [4] E. Fermi. *An attempt of a theory of beta radiation. I.* *Nuclear Physics B* **4** (1967).
1817 Translated from the original 1934 German article by C. P. Enz and C. H. Beck, pp. 1–
1818 27 (cit. on p. 1).
- 1819 [5] D. J. Griffiths. *Introduction to Elementary Particles.* 2nd. Weinheim: Wiley-VCH,
1820 2008. ISBN: 978-3-527-40601-2 (cit. on p. 1).
- 1821 [6] C. Yang and R. Mills. *Conservation of Isotopic Spin and Isotopic Gauge Invariance.*
1822 *Phys. Rev.* **96** (1 1954), pp. 191–195 (cit. on pp. 1, 10).
- 1823 [7] A. Milsted and T. J. Osborne. *Quantum Yang-Mills theory: An overview of a program.*
1824 *Phys. Rev. D* **98** (1 2018), p. 014505 (cit. on pp. 1, 10).

- 1825 [8] S. L. Glashow. *Partial-symmetries of weak interactions*. Nuclear Physics 22.4 (1961),
1826 pp. 579–588. ISSN: 0029-5582 (cit. on p. 1).
- 1827 [9] D. J. Gross and F. Wilczek. *Ultraviolet Behavior of Non-Abelian Gauge Theories*.
1828 Phys. Rev. Lett. 30 (26 1973), pp. 1343–1346 (cit. on p. 1).
- 1829 [10] H. D. Politzer. *Reliable Perturbative Results for Strong Interactions?* Phys. Rev. Lett.
1830 30 (26 1973), pp. 1346–1349 (cit. on p. 1).
- 1831 [11] P. Higgs. *Broken symmetries and the masses of gauge bosons*. Phys. Rev. Lett. 13 (16
1832 1964), pp. 508–509 (cit. on pp. 1, 14).
- 1833 [12] P. Higgs. *Broken symmetries, massless particles and gauge fields*. Physics Letters 12.2
1834 (1964), pp. 132–133. ISSN: 0031-9163 (cit. on pp. 1, 14).
- 1835 [13] F. Englert and R. Brout. *Broken Symmetry and the Mass of Gauge Vector Mesons*.
1836 Phys. Rev. Lett. 13 (9 1964), pp. 321–323 (cit. on pp. 1, 14).
- 1837 [14] S. Weinberg. *The making of the Standard Model*. The European Physical Journal C
1838 34.1 (May 2004), 513. ISSN: 1434-6052. arXiv: hep-ph/0401010 [hep-ph] (cit. on
1839 p. 2).
- 1840 [15] D. P. Barber et al. *Discovery of Three-Jet Events and a Test of Quantum Chromody-
1841 namics at PETRA*. Phys. Rev. Lett. 43 (12 1979), pp. 830–833 (cit. on p. 2).
- 1842 [16] G. Arnison et al. *Experimental Observation of Isolated Large Transverse Energy Elec-
1843 trons with Associated Missing Energy at $\sqrt{s} = 540 \text{ GeV}$* . Phys. Lett. B 122 (1983),
1844 pp. 103–116 (cit. on p. 2).

- 1845 [17] G. Arnison and others. *Experimental Observation of Lepton Pairs of Invariant Mass*
1846 *Around $95 \text{ GeV}/c^2$ at the CERN SPS Collider.* [Phys. Lett. B 126 \(1983\), pp. 398–410](#)
1847 (cit. on p. 2).
- 1848 [18] CDF Collaboration. *Observation of Top Quark Production in $\bar{p}p$ Collisions with the*
1849 *Collider Detector at Fermilab.* [Phys. Rev. Lett. 74 \(14 1995\), pp. 2626–2631](#) (cit. on
1850 p. 2).
- 1851 [19] DØ Collaboration. *Observation of the Top Quark.* [Phys. Rev. Lett. 74 \(14 1995\),](#)
1852 pp. 2632–2637 (cit. on p. 2).
- 1853 [20] ATLAS Collaboration. *Observation of a new particle in the search for the Standard*
1854 *Model Higgs boson with the ATLAS detector at the LHC.* [Phys. Lett. B 716 \(2012\),](#)
1855 p. 1. arXiv: 1207.7214 [[hep-ex](#)] (cit. on pp. 2, 14).
- 1856 [21] CMS Collaboration. *Observation of a new boson at a mass of 125 GeV with the CMS*
1857 *experiment at the LHC.* [Phys. Lett. B 716 \(2012\), p. 30.](#) arXiv: 1207.7235 [[hep-ex](#)]
1858 (cit. on pp. 2, 14).
- 1859 [22] S. Navas et al. *Review of particle physics.* [Phys. Rev. D 110.3 \(2024\), p. 030001](#) (cit.
1860 on pp. 2, 7, 8).
- 1861 [23] Y. Fukuda et al. *Evidence for Oscillation of Atmospheric Neutrinos.* [Phys. Rev. Lett.](#)
1862 81 (8 1998), pp. 1562–1567 (cit. on p. 2).
- 1863 [24] M. Cristinziani and M. Mulders. *Top-quark physics at the Large Hadron Collider.*
1864 Journal of Physics G: Nuclear and Particle Physics 44.6 (2017), p. 063001. arXiv:
1865 1606.00327 [[hep-ex](#)] (cit. on pp. 2, 8).

- 1866 [25] ATLAS and CMS Collaborations. *Combination of inclusive top-quark pair production*
1867 *cross-section measurements using ATLAS and CMS data at $\sqrt{s} = 7$ and 8 TeV.* *JHEP*
1868 **07** (2023), p. 213. arXiv: [2205.13830 \[hep-ex\]](#) (cit. on p. 3).
- 1869 [26] C. Degrande, J.-M. Grard, C. Grojean, F. Maltoni, and G. Servant. *Non-resonant new*
1870 *physics in top pair production at hadron colliders.* *Journal of High Energy Physics*
1871 **2011.3** (Mar. 2011). ISSN: 1029-8479. arXiv: [1010.6304 \[hep-ph\]](#) (cit. on p. 3).
- 1872 [27] ATLAS Collaboration. *The ATLAS Experiment at the CERN Large Hadron Collider.*
1873 *JINST* **3** (2008), S08003 (cit. on pp. 3, 22, 25, 26, 28–32).
- 1874 [28] ATLAS Collaboration. *Search for top-philic heavy resonances in pp collisions at $\sqrt{s} =$*
1875 *13 TeV with the ATLAS detector.* *Eur. Phys. J. C* **84** (2024), p. 157. arXiv: [2304.01678 \[hep-ex\]](#) (cit. on pp. 3, 4, 18, 97).
- 1877 [29] H. P. Nilles. *Supersymmetry, Supergravity and Particle Physics.* *Phys. Rept.* **110**
1878 (1984), pp. 1–162 (cit. on p. 3).
- 1879 [30] G. R. Farrar and P. Fayet. *Phenomenology of the Production, Decay, and Detection*
1880 *of New Hadronic States Associated with Supersymmetry.* *Phys. Lett. B* **76** (1978),
1881 pp. 575–579 (cit. on p. 3).
- 1882 [31] T. Plehn and T. M. P. Tait. *Seeking sgluons.* *Journal of Physics G: Nuclear and*
1883 *Particle Physics* **36.7** (2009), p. 075001. arXiv: [0810.3919 \[hep-ph\]](#) (cit. on p. 3).
- 1884 [32] S. Calvet, B. Fuks, P. Gris, and L. Valry. *Searching for sgluons in multitop events*
1885 *at a center-of-mass energy of 8 TeV.* *Journal of High Energy Physics* **2013.4** (Apr.
1886 2013). ISSN: 1029-8479. arXiv: [1212.3360 \[hep-ph\]](#) (cit. on p. 3).

- 1887 [33] A. Pomarol and J. Serra. *Top quark compositeness: Feasibility and implications*. Phys-
1888 ical Review D 78.7 (Oct. 2008). ISSN: 1550-2368. arXiv: 0806.3247 [hep-ph] (cit. on
1889 p. 3).
- 1890 [34] K. Kumar, T. M. Tait, and R. Vega-Morales. *Manifestations of top compositeness at*
1891 *colliders*. Journal of High Energy Physics 2009.05 (May 2009), 022022. ISSN: 1029-
1892 8479. arXiv: 0901.3808 [hep-ph] (cit. on p. 3).
- 1893 [35] G. Banelli, E. Salvioni, J. Serra, T. Theil, and A. Weiler. *The present and future of*
1894 *four top operators*. Journal of High Energy Physics 2021.2 (Feb. 2021). ISSN: 1029-
1895 8479. arXiv: 2010.05915 [hep-ph] (cit. on p. 3).
- 1896 [36] R. Aoude, H. El Faham, F. Maltoni, and E. Vryonidou. *Complete SMEFT predictions*
1897 *for four top quark production at hadron colliders*. Journal of High Energy Physics
1898 2022.10 (Oct. 2022). ISSN: 1029-8479. arXiv: 2208.04962 [hep-ph] (cit. on p. 3).
- 1899 [37] C. Zhang. *Constraining qqtt operators from four-top production: a case for enhanced*
1900 *EFT sensitivity*. Chinese Physics C 42.2 (Feb. 2018), p. 023104. ISSN: 1674-1137.
1901 arXiv: 1708.05928 [hep-ph] (cit. on p. 3).
- 1902 [38] L. Darmé, B. Fuks, and F. Maltoni. *Topophilic heavy resonances in four-top final*
1903 *states and their EFT interpretation*. Journal of High Energy Physics 2021.9 (Sept.
1904 2021). ISSN: 1029-8479. arXiv: 2104.09512 [hep-ph] (cit. on pp. 3, 17).
- 1905 [39] N. Craig, F. D'Eramo, P. Draper, S. Thomas, and H. Zhang. *The Hunt for the Rest*
1906 *of the Higgs Bosons*. JHEP 06 (2015), p. 137. arXiv: 1504.04630 [hep-ph] (cit. on
1907 pp. 3, 17).

- 1908 [40] N. Craig, J. Hajer, Y.-Y. Li, T. Liu, and H. Zhang. *Heavy Higgs bosons at low $\tan \beta$:
1909 from the LHC to 100 TeV*. Journal of High Energy Physics 2017.1 (Jan. 2017). ISSN:
1910 1029-8479. arXiv: 1605.08744 [hep-ph] (cit. on pp. 3, 17).
- 1911 [41] G. C. Branco et al. *Theory and phenomenology of two-Higgs-doublet models*. Phys.
1912 Rept. 516 (2012), pp. 1–102. arXiv: 1106.0034 [hep-ph] (cit. on pp. 3, 17).
- 1913 [42] S. Gori, I.-W. Kim, N. R. Shah, and K. M. Zurek. *Closing the wedge: Search strategies
1914 for extended Higgs sectors with heavy flavor final states*. Phys. Rev. D 93 (7 2016),
1915 p. 075038 (cit. on pp. 3, 17).
- 1916 [43] P. S. B. Dev and A. Pilaftsis. *Maximally symmetric two Higgs doublet model with
1917 natural Standard Model alignment*. Journal of High Energy Physics 2014.12 (Dec.
1918 2014), p. 024. arXiv: 1408.3405 [hep-ph] (cit. on pp. 3, 17).
- 1919 [44] ATLAS Collaboration. *Observation of four-top-quark production in the multilepton
1920 final state with the ATLAS detector*. Eur. Phys. J. C 83 (2023), p. 496. arXiv: 2303.
1921 15061 [hep-ex] (cit. on pp. 3, 4, 18, 51, 64, 71, 80).
- 1922 [45] N. Greiner, K. Kong, J.-C. Park, S. C. Park, and J.-C. Winter. *Model-independent
1923 production of a topophilic resonance at the LHC*. Journal of High Energy Physics
1924 2015.4 (2015), p. 29. ISSN: 1029-8479. arXiv: 1410.6099 [hep-ph] (cit. on pp. 3, 18–
1925 20).
- 1926 [46] ATLAS Collaboration. *Search for $t\bar{t}H/A \rightarrow t\bar{t}t\bar{t}$ production in the multilepton final
1927 state in proton–proton collisions at $\sqrt{s} = 13$ TeV with the ATLAS detector*. JHEP 07
1928 (2023), p. 203. arXiv: 2211.01136 [hep-ex] (cit. on p. 4).

- 1929 [47] ATLAS Collaboration. *Evidence for $t\bar{t}t\bar{t}$ production in the multilepton final state in*
- 1930 proton–proton collisions at $\sqrt{s} = 13\text{TeV}$ with the ATLAS detector. *Eur. Phys. J. C*
- 1931 80 (2020), p. 1085. arXiv: 2007.14858 [hep-ex] (cit. on pp. 4, 71).
- 1932 [48] D. H. Perkins. *Introduction to High Energy Physics*. 4th. Cambridge, UK: Cambridge
- 1933 University Press, Apr. 2000. ISBN: 9780521621960 (cit. on p. 5).
- 1934 [49] C. Burgard and D. Galbraith. *Standard Model of Physics*. URL: <https://texample.net/model-physics/> (visited on 06/02/2025) (cit. on p. 6).
- 1935
- 1936 [50] H. Georgi. *Lie Algebras in Particle Physics: from Isospin to Unified Theories*. 2nd.
- 1937 CRC Press, 2000. ISBN: 9780429499210 (cit. on pp. 7, 10).
- 1938 [51] ATLAS and CMS Collaborations. *Combination of Measurements of the Top Quark*
- 1939 *Mass from Data Collected by the ATLAS and CMS Experiments at $\sqrt{s} = 7$ and 8 TeV*.
- 1940 *Phys. Rev. Lett.* 132 (2023), p. 261902. arXiv: 2402.08713 [hep-ex] (cit. on p. 8).
- 1941 [52] H. de la Torre and T. Farooque. *Looking beyond the Standard Model with Third Gen-*
- 1942 *eration Quarks at the LHC*. *Symmetry* 14.3 (2022), p. 444 (cit. on p. 8).
- 1943 [53] Q.-H. Cao, J.-N. Fu, Y. Liu, X.-H. Wang, and R. Zhang. *Probing Top-philic New*
- 1944 *Physics via Four-Top-Quark Production*. *Chinese Physics C* 45.9 (2021), p. 093107.
- 1945 arXiv: 2105.03372 [hep-ph] (cit. on p. 8).
- 1946 [54] H. Beauchesne et al. *A case study about BSM vector resonances with direct couplings*
- 1947 *to the third quark generation*. *European Physical Journal C* 80.5 (2020), p. 485. arXiv:
- 1948 1908.11619 [hep-ph] (cit. on p. 8).
- 1949 [55] F. Maltoni, D. Pagani, and S. Tentori. *Top-quark pair production as a probe of light*
- 1950 *top-philic scalars and anomalous Higgs interactions*. *Journal of High Energy Physics*
- 1951 2024.9 (Sept. 2024), p. 098. arXiv: 2406.06694 [hep-ph] (cit. on p. 8).

- 1952 [56] CMS Collaboration. *Search for $t\bar{t}H$ production in the $H \rightarrow b\bar{b}$ decay channel with*
- 1953 leptonic $t\bar{t}$ decays in proton–proton collisions at $\sqrt{s} = 13$ TeV. *JHEP* **03** (2019),
- 1954 p. 026. arXiv: [1804.03682 \[hep-ex\]](https://arxiv.org/abs/1804.03682) (cit. on p. 8).
- 1955 [57] Y. Grossman and Y. Nir. *The Standard Model: From Fundamental Symmetries to Ex-*
- 1956 *perimental Tests.* See Chapter 8.2. Cambridge University Press, 2023. ISBN: 9781009320378
- 1957 (cit. on p. 9).
- 1958 [58] M. E. Peskin and D. V. Schroeder. *An Introduction to Quantum Field Theory.* 1st.
- 1959 Reading, MA, USA: AddisonWesley, 1995. ISBN: 978-0-201-50397-5 (cit. on p. 9).
- 1960 [59] D. J. Gross. *The role of symmetry in fundamental physics.* *Proceedings of the National*
- 1961 *Academy of Sciences of the United States of America* **93**.25 (Dec. 1996), pp. 14256–
- 1962 14259 (cit. on p. 9).
- 1963 [60] M. Bañados and I. Reyes. *A short review on Noethers theorems, gauge symmetries*
- 1964 *and boundary terms.* *International Journal of Modern Physics D* **25**.10 (Aug. 2016),
- 1965 p. 1630021. ISSN: 1793-6594. arXiv: [1601.03616 \[hep-th\]](https://arxiv.org/abs/1601.03616) (cit. on p. 9).
- 1966 [61] A. Pich. *The Standard Model of electroweak interactions.* *2004 European School of*
- 1967 *High-Energy Physics.* Feb. 2005, pp. 1–48. arXiv: [hep-ph/0502010 \[hep-ex\]](https://arxiv.org/abs/hep-ph/0502010) (cit. on
- 1968 pp. 11–13).
- 1969 [62] P. Dev and A. Pilaftsis. *High-temperature electroweak symmetry non-restoration from*
- 1970 *new fermions and implications for baryogenesis.* *Journal of High Energy Physics*
- 1971 **2020**.9 (Sept. 2020), p. 012. arXiv: [2002.05174 \[hep-ph\]](https://arxiv.org/abs/2002.05174) (cit. on p. 13).
- 1972 [63] J. Riebesell. *Higgs Potential.* URL: <https://tikz.net/higgs-potential/> (visited on
- 1973 07/07/2025) (cit. on p. 15).

- 1974 [64] J. Goldstone, A. Salam, and S. Weinberg. *Broken Symmetries*. Phys. Rev. 127 (3
1975 1962), pp. 965–970 (cit. on p. 15).
- 1976 [65] J. Ellis. *Higgs Physics. 2013 European School of High-Energy Physics*. 2015, pp. 117–
1977 168. arXiv: 1312.5672 [hep-ph] (cit. on pp. 15, 16).
- 1978 [66] G. Ferretti and D. Karateev. *Fermionic UV completions of composite Higgs models*.
1979 Journal of High Energy Physics 2014.3 (Mar. 2014). ISSN: 1029-8479 (cit. on p. 17).
- 1980 [67] L. Vecchi. *A dangerous irrelevant UV-completion of the composite Higgs*. JHEP 02
1981 (2017), p. 094. arXiv: 1506.00623 [hep-ph] (cit. on p. 17).
- 1982 [68] CDF Collaboration. *Search for New Physics in High-Mass Electron-Positron Events
1983 in $p\bar{p}$ Collisions at $\sqrt{s} = 1.96$ TeV*. Phys. Rev. Lett. 99 (17 2007), p. 171802. arXiv:
1984 0707.2524 [hep-ex] (cit. on p. 17).
- 1985 [69] M. Battaglia and G. Servant. *Four-top production and $t\bar{t}$ +missing energy events at
1986 multi TeV e^+e^- colliders*. Nuovo Cim. C 033N2 (2010), pp. 203–208. arXiv: 1005.4632
1987 [hep-ex] (cit. on p. 17).
- 1988 [70] N. Arkani-Hamed, A. G. Cohen, and H. Georgi. *Electroweak symmetry breaking from
1989 dimensional deconstruction*. Physics Letters B 513.1-2 (July 2001), pp. 232–240. arXiv:
1990 hep-ph/0105239 [hep-ph] (cit. on p. 17).
- 1991 [71] T. Han, H. E. Logan, B. McElrath, and L.-T. Wang. *Phenomenology of the little Higgs
1992 model*. Phys. Rev. D 67 (9 2003), p. 095004. arXiv: hep-ph/0301040 [hep-ph] (cit. on
1993 p. 17).
- 1994 [72] P. Langacker and M. Plümacher. *Flavor changing effects in theories with a heavy Z'
1995 boson with family nonuniversal couplings*. Phys. Rev. D 62 (1 2000), p. 013006. arXiv:
1996 hep-ph/0001204 [hep-ph].

- 1997 [73] P. Langacker. *The Physics of Heavy Z' Gauge Bosons*. *Rev. Mod. Phys.* **81** (2009),
1998 pp. 1199–1228. arXiv: [0801.1345 \[hep-ph\]](#) (cit. on p. 17).
- 1999 [74] J. H. Kim, K. Kong, S. J. Lee, and G. Mohlabeng. *Probing TeV scale top-philic*
2000 *resonances with boosted top-tagging at the high luminosity LHC*. *Phys. Rev. D* **94** (3
2001 2016), p. 035023. arXiv: [1604.07421 \[hep-ph\]](#) (cit. on pp. xi, 17, 18, 20, 86, 96).
- 2002 [75] P. J. Fox, I. Low, and Y. Zhang. *Top-philic Z' forces at the LHC*. *Journal of High*
2003 *Energy Physics* **2018**.3 (Mar. 2018). ISSN: 1029-8479. arXiv: [1801.03505 \[hep-ph\]](#)
2004 (cit. on p. 17).
- 2005 [76] CMS Collaboration. *Observation of four top quark production in proton-proton col-*
2006 *lisions at $\sqrt{s} = 13\text{TeV}$* . *Physics Letters B* **847** (2023), p. 138290. arXiv: [2305.13439](#)
2007 [\[hep-ex\]](#) (cit. on p. 18).
- 2008 [77] G. Brooijmans et al. *New Physics at the LHC. A Les Houches Report: Physics at*
2009 *TeV Colliders 2009 - New Physics Working Group. 6th Les Houches Workshop on*
2010 *Physics at TeV Colliders*. See Chapter 12. May 2010, pp. 191–380. arXiv: [1005.1229](#)
2011 [\[hep-ph\]](#) (cit. on p. 20).
- 2012 [78] P. Sabatini. *Evidence for four-top-quarks production with the ATLAS detector at the*
2013 *Large Hadron Collider*. Tech. rep. Geneva: CERN, 2021. URL: <https://cds.cern.ch/record/2784150> (cit. on p. 21).
- 2015 [79] L. Evans and P. Bryant. *LHC Machine*. *JINST* **3** (2008), S08001 (cit. on p. 22).
- 2016 [80] CMS Collaboration. *The CMS Experiment at the CERN LHC*. *JINST* **3** (2008),
2017 S08004 (cit. on p. 22).
- 2018 [81] The ALICE Collaboration. *The ALICE experiment at the CERN LHC*. *JINST* **3**
2019 (2008), S08002 (cit. on p. 22).

- 2020 [82] The LHCb Collaboration. *The LHCb Detector at the LHC*. *JINST* **3** (2008), S08005
2021 (cit. on p. 22).
- 2022 [83] E. e. a. Gschwendtner. *AWAKE, The Advanced Proton Driven Plasma Wakefield*
2023 *Acceleration Experiment at CERN*. Nuclear Instruments and Methods in Physics Re-
2024 search Section A **829** (2016), pp. 76–82. arXiv: 1512.05498 [physics.acc-ph] (cit. on
2025 p. 23).
- 2026 [84] J. L. Feng, I. Galon, F. Kling, and S. Trojanowski. *ForwArd Search ExpeRiment at*
2027 *the LHC*. *Phys. Rev. D* **97** (3 2018), p. 035001. arXiv: 1708.09389 [hep-ph] (cit. on
2028 p. 23).
- 2029 [85] The KATRIN collaboration. *The design, construction, and commissioning of the KA-*
2030 *TRIN experiment*. *Journal of Instrumentation* **16.08** (2021), T08015. arXiv: 2103.
2031 04755 [physics.ins-det] (cit. on p. 23).
- 2032 [86] E. Lopienska. *The CERN accelerator complex, layout in 2022*. General Photo. 2022.
2033 URL: <https://cds.cern.ch/record/2800984> (visited on 07/08/2025) (cit. on p. 23).
- 2034 [87] High Luminosity LHC Project Organization. *The HL-LHC project*. 2025. URL: <https://hilumilhc.web.cern.ch/content/hl-lhc-project> (visited on 06/11/2025) (cit. on
2035 p. 24).
- 2036 [88] ATLAS Collaboration. *Performance of the ATLAS detector using first collision data*.
2037 *JHEP* **09** (2010), p. 056. arXiv: 1005.5254 [hep-ex] (cit. on p. 24).
- 2039 [89] ATLAS Collaboration. *Luminosity determination in pp collisions at $\sqrt{s} = 13 \text{ TeV}$*
2040 *using the ATLAS detector at the LHC*. *Eur. Phys. J. C* **83** (2023), p. 982. arXiv:
2041 2212.09379 [hep-ex] (cit. on pp. 25, 51, 74).

- 2042 [90] J. M. Butterworth, G. Dissertori, and G. P. Salam. *Hard Processes in Proton-Proton*
2043 *Collisions at the Large Hadron Collider*. *Annu. Rev. Nucl. Part. Sci.* **62** (2012),
2044 pp. 387–405. arXiv: [1202.0583 \[hep-ex\]](https://arxiv.org/abs/1202.0583) (cit. on p. 25).
- 2045 [91] J. Campbell, J. Huston, and W. J. Stirling. *Hard interactions of quarks and gluons:*
2046 *a primer for LHC physics*. *Reports on Progress in Physics* **70**.1 (2006), p. 89. arXiv:
2047 [hep-ph/0611148 \[hep-ex\]](https://arxiv.org/abs/hep-ph/0611148) (cit. on p. 25).
- 2048 [92] ATLAS Collaboration. *Standard Model Summary Plots October 2023*. ATL-PHYS-
2049 PUB-2023-039. 2023. URL: <https://cds.cern.ch/record/2882448> (cit. on p. 26).
- 2050 [93] J. Pequenao and P. Schaffner. *How ATLAS detects particles: diagram of particle*
2051 *paths in the detector*. 2013. URL: <https://cds.cern.ch/record/1505342> (visited on
2052 07/08/2025) (cit. on p. 27).
- 2053 [94] J. Pequenao. *Computer generated image of the ATLAS inner detector*. 2008. URL:
2054 <https://cds.cern.ch/record/1095926> (visited on 07/08/2025) (cit. on p. 28).
- 2055 [95] J. Pequenao. *Computer Generated image of the ATLAS calorimeter*. 2008. URL: <https://cds.cern.ch/record/1095927> (visited on 07/08/2025) (cit. on p. 30).
- 2057 [96] ATLAS Collaboration. *Operation of the ATLAS trigger system in Run 2*. *JINST* **15**
2058 (2020), P10004. arXiv: [2007.12539 \[physics.ins-det\]](https://arxiv.org/abs/2007.12539) (cit. on p. 33).
- 2059 [97] ATLAS Collaboration. *Performance of the ATLAS track reconstruction algorithms*
2060 *in dense environments in LHC Run 2*. *Eur. Phys. J. C* **77** (2017), p. 673. arXiv:
2061 [1704.07983 \[hep-ex\]](https://arxiv.org/abs/1704.07983) (cit. on p. 34).
- 2062 [98] T. Cornelissen et al. *Concepts, design and implementation of the ATLAS New Track-*
2063 *ing (NEWT)*. Tech. rep. Geneva: CERN, 2007. URL: <https://cds.cern.ch/record/1020106> (cit. on p. 34).

- 2065 [99] A. Salzburger. *Optimisation of the ATLAS Track Reconstruction Software for Run-2*.
2066 *Journal of Physics: Conference Series* 664.7 (2015), p. 072042 (cit. on p. 34).
- 2067 [100] R. Frühwirth. *Application of Kalman filtering to track and vertex fitting*. *Nucl. In-*
2068 *strum. Methods Phys. Res. A* 262.2 (1987), pp. 444–450. ISSN: 0168-9002 (cit. on
2069 p. 34).
- 2070 [101] T. Cornelissen et al. *The global χ^2 track fitter in ATLAS*. *Journal of Physics: Con-*
2071 *ference Series* 119.3 (2008), p. 032013 (cit. on p. 34).
- 2072 [102] ATLAS Collaboration. *Improved electron reconstruction in ATLAS using the Gaus-*
2073 *sian Sum Filter-based model for bremsstrahlung*. ATLAS-CONF-2012-047. 2012. URL:
2074 <https://cds.cern.ch/record/1449796> (cit. on p. 34).
- 2075 [103] D. Wicke. *A new algorithm for solving tracking ambiguities*. Tech. rep. Oct. 1998.
2076 URL: <https://cds.cern.ch/record/2625731> (cit. on p. 35).
- 2077 [104] ATLAS Collaboration. *Reconstruction of primary vertices at the ATLAS experiment*
2078 *in Run 1 proton–proton collisions at the LHC*. *Eur. Phys. J. C* 77 (2017), p. 332.
2079 arXiv: [1611.10235 \[physics.ins-det\]](https://arxiv.org/abs/1611.10235) (cit. on p. 35).
- 2080 [105] W. Waltenberger, R. Frühwirth, and P. Vanlaer. *Adaptive vertex fitting*. *Journal of*
2081 *Physics G: Nuclear and Particle Physics* 34.12 (2007), N343 (cit. on p. 35).
- 2082 [106] ATLAS Collaboration. *Secondary vertex finding for jet flavour identification with the*
2083 *ATLAS detector*. ATL-PHYS-PUB-2017-011. 2017. URL: <https://cds.cern.ch/record/2270366> (cit. on p. 35).
- 2085 [107] ATLAS Collaboration. *Performance of pile-up mitigation techniques for jets in pp*
2086 *collisions at $\sqrt{s} = 8 \text{ TeV}$ using the ATLAS detector*. *Eur. Phys. J. C* 76 (2016),
2087 p. 581. arXiv: [1510.03823 \[hep-ex\]](https://arxiv.org/abs/1510.03823) (cit. on pp. 36, 39).

- 2088 [108] ATLAS Collaboration. *Topological cell clustering in the ATLAS calorimeters and its*
2089 *performance in LHC Run 1.* *Eur. Phys. J. C* **77** (2017), p. 490. arXiv: [1603.02934](#)
2090 [[hep-ex](#)] (cit. on pp. 36, 37).
- 2091 [109] ATLAS Collaboration. *Jet reconstruction and performance using particle flow with*
2092 *the ATLAS Detector.* *Eur. Phys. J. C* **77** (2017), p. 466. arXiv: [1703.10485](#) [[hep-ex](#)]
2093 (cit. on p. 38).
- 2094 [110] M. Cacciari, G. P. Salam, and G. Soyez. *The anti- k_t jet clustering algorithm.* *JHEP*
2095 **04** (2008), p. 063. arXiv: [0802.1189](#) [[hep-ph](#)] (cit. on p. 38).
- 2096 [111] ATLAS Collaboration. *Jet energy scale and resolution measured in proton–proton*
2097 *collisions at $\sqrt{s} = 13\text{ TeV}$ with the ATLAS detector.* *Eur. Phys. J. C* **81** (2021),
2098 p. 689. arXiv: [2007.02645](#) [[hep-ex](#)] (cit. on pp. 39, 75–77).
- 2099 [112] ATLAS Collaboration. *Jet energy scale measurements and their systematic uncertain-*
2100 *ties in proton–proton collisions at $\sqrt{s} = 13\text{ TeV}$ with the ATLAS detector.* *Phys. Rev.*
2101 **D 96** (2017), p. 072002. arXiv: [1703.09665](#) [[hep-ex](#)] (cit. on pp. 39, 75).
- 2102 [113] ATLAS Collaboration. *Transforming jet flavour tagging at ATLAS.* Tech. rep. Sub-
2103 mitted to: Nature Communications. Geneva: CERN, 2025. arXiv: [2505.19689](#) (cit. on
2104 pp. 40–42).
- 2105 [114] A. Vaswani et al. *Attention Is All You Need.* 2023. arXiv: [1706.03762](#) [[cs.CL](#)] (cit. on
2106 p. 40).
- 2107 [115] ATLAS Collaboration. *Measurements of b -jet tagging efficiency with the ATLAS de-*
2108 *tector using $t\bar{t}$ events at $\sqrt{s} = 13\text{ TeV}.$* *JHEP* **08** (2018), p. 089. arXiv: [1805.01845](#)
2109 [[hep-ex](#)] (cit. on pp. 42, 77).

- 2110 [116] ATLAS Collaboration. *Electron reconstruction and identification in the ATLAS ex-*
 2111 *periment using the 2015 and 2016 LHC proton–proton collision data at $\sqrt{s} = 13$ TeV.*
 2112 *Eur. Phys. J. C* **79** (2019), p. 639. arXiv: [1902.04655 \[physics.ins-det\]](#) (cit. on
 2113 pp. 43–45).
- 2114 [117] ATLAS Collaboration. *Muon reconstruction and identification efficiency in ATLAS*
 2115 *using the full Run 2 pp collision data set at $\sqrt{s} = 13$ TeV.* *Eur. Phys. J. C* **81** (2021),
 2116 p. 578. arXiv: [2012.00578 \[hep-ex\]](#) (cit. on pp. 46, 47).
- 2117 [118] ATLAS Collaboration. *Muon reconstruction performance of the ATLAS detector in*
 2118 *proton–proton collision data at $\sqrt{s} = 13$ TeV.* *Eur. Phys. J. C* **76** (2016), p. 292. arXiv:
 2119 [1603.05598 \[hep-ex\]](#) (cit. on p. 47).
- 2120 [119] ATLAS Collaboration. *Performance of missing transverse momentum reconstruction*
 2121 *with the ATLAS detector using proton–proton collisions at $\sqrt{s} = 13$ TeV.* *Eur. Phys.*
 2122 *J. C* **78** (2018), p. 903. arXiv: [1802.08168 \[hep-ex\]](#) (cit. on pp. 48, 77).
- 2123 [120] ATLAS Collaboration. *E_T^{miss} performance in the ATLAS detector using 2015–2016*
 2124 *LHC pp collisions.* ATLAS-CONF-2018-023. 2018. URL: <https://cds.cern.ch/record/2625233> (cit. on p. 49).
- 2126 [121] J. Alwall et al. *The automated computation of tree-level and next-to-leading order*
 2127 *differential cross sections, and their matching to parton shower simulations.* *JHEP* **07**
 2128 (2014), p. 079. arXiv: [1405.0301 \[hep-ph\]](#) (cit. on pp. 52, 54–57).
- 2129 [122] NNPDF Collaboration, R. D. Ball, et al. *Parton distributions for the LHC run II.*
 2130 *JHEP* **04** (2015), p. 040. arXiv: [1410.8849 \[hep-ph\]](#) (cit. on pp. 52, 54–58).
- 2131 [123] T. Sjöstrand et al. *An introduction to PYTHIA 8.2.* *Comput. Phys. Commun.* **191**
 2132 (2015), p. 159. arXiv: [1410.3012 \[hep-ph\]](#) (cit. on pp. 52, 54–58).

- 2133 [124] ATLAS Collaboration. *ATLAS Pythia 8 tunes to 7 TeV data*. ATL-PHYS-PUB-2014-
 2134 021. 2014. URL: <https://cds.cern.ch/record/1966419> (cit. on pp. 54–58).
- 2135 [125] S. Frixione, E. Laenen, P. Motylinski, and B. R. Webber. *Angular correlations of*
 2136 *lepton pairs from vector boson and top quark decays in Monte Carlo simulations*.
 2137 JHEP 04 (2007), p. 081. arXiv: [hep-ph/0702198](https://arxiv.org/abs/hep-ph/0702198) (cit. on p. 54).
- 2138 [126] P. Artoisenet, R. Frederix, O. Mattelaer, and R. Rietkerk. *Automatic spin-entangled*
 2139 *decays of heavy resonances in Monte Carlo simulations*. JHEP 03 (2013), p. 015.
 2140 arXiv: [1212.3460 \[hep-ph\]](https://arxiv.org/abs/1212.3460) (cit. on p. 54).
- 2141 [127] D. J. Lange. *The EvtGen particle decay simulation package*. Nucl. Instrum. Meth. A
 2142 462 (2001), p. 152 (cit. on p. 54).
- 2143 [128] R. Frederix, D. Pagani, and M. Zaro. *Large NLO corrections in $t\bar{t}W^\pm$ and $t\bar{t}t\bar{t}$*
 2144 *hadroproduction from supposedly subleading EW contributions*. JHEP 02 (2018), p. 031.
 2145 arXiv: [1711.02116 \[hep-ph\]](https://arxiv.org/abs/1711.02116) (cit. on pp. 54, 79).
- 2146 [129] E. Bothmann et al. *Event generation with Sherpa 2.2*. SciPost Phys. 7.3 (2019), p. 034.
 2147 arXiv: [1905.09127 \[hep-ph\]](https://arxiv.org/abs/1905.09127) (cit. on pp. 54, 55, 57).
- 2148 [130] S. Schumann and F. Krauss. *A parton shower algorithm based on Catani–Seymour*
 2149 *dipole factorisation*. JHEP 03 (2008), p. 038. arXiv: [0709.1027 \[hep-ph\]](https://arxiv.org/abs/0709.1027) (cit. on
 2150 pp. 54, 57, 58).
- 2151 [131] S. Höche, F. Krauss, M. Schönherr, and F. Siegert. *A critical appraisal of NLO+PS*
 2152 *matching methods*. JHEP 09 (2012), p. 049. arXiv: [1111.1220 \[hep-ph\]](https://arxiv.org/abs/1111.1220) (cit. on pp. 54,
 2153 57, 58).

- 2154 [132] S. Höche, F. Krauss, M. Schönherr, and F. Siegert. *QCD matrix elements + parton*
 2155 *showers. The NLO case.* JHEP 04 (2013), p. 027. arXiv: [1207.5030 \[hep-ph\]](#) (cit. on
 2156 pp. 54, 57, 58).
- 2157 [133] S. Catani, F. Krauss, B. R. Webber, and R. Kuhn. *QCD Matrix Elements + Parton*
 2158 *Showers.* JHEP 11 (2001), p. 063. arXiv: [hep-ph/0109231](#) (cit. on pp. 54, 57, 58).
- 2159 [134] S. Höche, F. Krauss, S. Schumann, and F. Siegert. *QCD matrix elements and truncated*
 2160 *showers.* JHEP 05 (2009), p. 053. arXiv: [0903.1219 \[hep-ph\]](#) (cit. on pp. 54, 57, 58).
- 2161 [135] F. Cascioli, P. Maierhöfer, and S. Pozzorini. *Scattering Amplitudes with Open Loops.*
 2162 Phys. Rev. Lett. 108 (2012), p. 111601. arXiv: [1111.5206 \[hep-ph\]](#) (cit. on pp. 54,
 2163 57, 58).
- 2164 [136] A. Denner, S. Dittmaier, and L. Hofer. *COLLIER: A fortran-based complex one-loop*
 2165 *library in extended regularizations.* Comput. Phys. Commun. 212 (2017), pp. 220–238.
 2166 arXiv: [1604.06792 \[hep-ph\]](#) (cit. on pp. 54, 57, 58).
- 2167 [137] F. Buccioni et al. *OpenLoops 2.* Eur. Phys. J. C 79.10 (2019), p. 866. arXiv: [1907.13071](#)
 2168 [hep-ph] (cit. on p. 54).
- 2169 [138] S. Frixione, G. Ridolfi, and P. Nason. *A positive-weight next-to-leading-order Monte*
 2170 *Carlo for heavy flavour hadroproduction.* JHEP 09 (2007), p. 126. arXiv: [0707.3088](#)
 2171 [hep-ph] (cit. on pp. 55, 56, 58).
- 2172 [139] P. Nason. *A new method for combining NLO QCD with shower Monte Carlo algo-*
 2173 *rithms.* JHEP 11 (2004), p. 040. arXiv: [hep-ph/0409146](#) (cit. on pp. 55, 56, 58).
- 2174 [140] S. Frixione, P. Nason, and C. Oleari. *Matching NLO QCD computations with parton*
 2175 *shower simulations: the POWHEG method.* JHEP 11 (2007), p. 070. arXiv: [0709.2092](#)
 2176 [hep-ph] (cit. on pp. 55, 56, 58).

- 2177 [141] S. Alioli, P. Nason, C. Oleari, and E. Re. *A general framework for implementing NLO*
 2178 *calculations in shower Monte Carlo programs: the POWHEG BOX*. *JHEP* **06** (2010),
 2179 p. 043. arXiv: [1002.2581 \[hep-ph\]](#) (cit. on pp. 55, 56, 58).
- 2180 [142] NNPDF Collaboration, R. D. Ball, et al. *Parton distributions with LHC data*. *Nucl.*
 2181 *Phys. B* **867** (2013), p. 244. arXiv: [1207.1303 \[hep-ph\]](#) (cit. on pp. 55, 56, 58).
- 2182 [143] M. Bähr et al. *Herwig++ physics and manual*. *Eur. Phys. J. C* **58** (2008), p. 639.
 2183 arXiv: [0803.0883 \[hep-ph\]](#) (cit. on p. 55).
- 2184 [144] J. Bellm et al. *Herwig 7.0/Herwig++ 3.0 release note*. *Eur. Phys. J. C* **76**.4 (2016),
 2185 p. 196. arXiv: [1512.01178 \[hep-ph\]](#) (cit. on p. 55).
- 2186 [145] S. Alekhin, J. Blümlein, S. Klein, and S. Moch. *The 3-, 4-, and 5-flavor NNLO parton*
 2187 *distribution functions from deep-inelastic-scattering data at hadron colliders*. *Physical*
 2188 *Review D* **81**.1 (Jan. 2010). ISSN: 1550-2368. arXiv: [0908.2766 \[hep-ph\]](#) (cit. on
 2189 pp. 55, 56).
- 2190 [146] ATLAS Collaboration. *Studies on top-quark Monte Carlo modelling for Top2016*.
 2191 ATL-PHYS-PUB-2016-020. 2016. URL: <https://cds.cern.ch/record/2216168> (cit. on
 2192 p. 56).
- 2193 [147] S. Frixione, E. Laenen, P. Motylinski, C. White, and B. R. Webber. *Single-top hadropro-*
 2194 *duction in association with a W boson*. *JHEP* **07** (2008), p. 029. arXiv: [0805.3067](#)
 2195 [\[hep-ph\]](#) (cit. on p. 56).
- 2196 [148] T. Gleisberg and S. Höche. *Comix, a new matrix element generator*. *JHEP* **12** (2008),
 2197 p. 039. arXiv: [0808.3674 \[hep-ph\]](#) (cit. on p. 57).

- 2198 [149] C. Anastasiou, L. Dixon, K. Melnikov, and F. Petriello. *High-precision QCD at hadron*
 2199 *colliders: Electroweak gauge boson rapidity distributions at next-to-next-to leading or-*
 2200 *der.* Phys. Rev. D 69 (2004), p. 094008. arXiv: [hep-ph/0312266](#) (cit. on p. 57).
- 2201 [150] ATLAS Collaboration. *ATLAS data quality operations and performance for 2015–*
 2202 *2018 data-taking.* JINST 15 (2020), P04003. arXiv: [1911.04632 \[physics.ins-det\]](#)
 2203 (cit. on p. 59).
- 2204 [151] ATLAS Collaboration. *Analysis of $t\bar{t}H$ and $t\bar{t}W$ production in multilepton final states*
 2205 *with the ATLAS detector.* ATLAS-CONF-2019-045. 2019. URL: <https://cds.cern.ch/record/2693930> (cit. on pp. 64, 68, 81).
- 2207 [152] ATLAS Collaboration. *Measurement of the total and differential cross-sections of $t\bar{t}W$*
 2208 *production in pp collisions at $\sqrt{s} = 13 \text{ TeV}$ with the ATLAS detector.* JHEP 05 (2024),
 2209 p. 131. arXiv: [2401.05299 \[hep-ex\]](#) (cit. on p. 64).
- 2210 [153] ATLAS Collaboration. *Search for new phenomena in events with same-charge leptons*
 2211 *and b -jets in pp collisions at $\sqrt{s} = 13 \text{ TeV}$ with the ATLAS detector.* JHEP 12 (2018),
 2212 p. 039. arXiv: [1807.11883 \[hep-ex\]](#) (cit. on p. 69).
- 2213 [154] ATLAS Collaboration. *Search for R -parity-violating supersymmetry in a final state*
 2214 *containing leptons and many jets with the ATLAS experiment using $\sqrt{s} = 13 \text{ TeV}$*
 2215 *proton–proton collision data.* Eur. Phys. J. C 81 (2021), p. 1023. arXiv: [2106.09609 \[hep-ex\]](#) (cit. on p. 71).
- 2217 [155] E. Gerwick, T. Plehn, S. Schumann, and P. Schichtel. *Scaling Patterns for QCD Jets.*
 2218 JHEP 10 (2012), p. 162. arXiv: [1208.3676 \[hep-ph\]](#) (cit. on pp. 71, 72).
- 2219 [156] G. Avoni et al. *The new LUCID-2 detector for luminosity measurement and moni-*
 2220 *toring in ATLAS.* JINST 13.07 (2018), P07017 (cit. on p. 74).

- 2221 [157] ATLAS Collaboration. *Tagging and suppression of pileup jets*. ATL-PHYS-PUB-2014-
2222 001. 2014. URL: <https://cds.cern.ch/record/1643929> (cit. on pp. 75, 77).
- 2223 [158] ATLAS Collaboration. *Measurements of inclusive and differential fiducial cross-sections*
2224 *of $t\bar{t}$ production with additional heavy-flavour jets in proton–proton collisions at $\sqrt{s} =$*
2225 *13 TeV with the ATLAS detector*. JHEP 04 (2019), p. 046. arXiv: 1811.12113 [hep-ex]
2226 (cit. on p. 79).
- 2227 [159] D. de Florian et al. *Handbook of LHC Higgs Cross Sections: 4. Deciphering the Nature*
2228 *of the Higgs Sector*. CERN Yellow Rep. Monogr. 2 (2017), pp. 1–869. arXiv: 1610.
2229 07922 [hep-ph] (cit. on p. 79).
- 2230 [160] ATLAS Collaboration. *Measurement of the production cross-section of a single top*
2231 *quark in association with a Z boson in proton–proton collisions at 13 TeV with the*
2232 *ATLAS detector*. ATLAS-CONF-2017-052. 2017. URL: <https://cds.cern.ch/record/2273868> (cit. on p. 79).
- 2234 [161] F. Demartin, B. Maier, F. Maltoni, K. Mawatari, and M. Zaro. *tWH associated*
2235 *production at the LHC*. EPJC 77.1 (2017). arXiv: 1607.05862 [hep-ph]. URL: <https://doi.org/10.1140/epjc/s10052-017-4601-7> (cit. on p. 79).
- 2237 [162] ATLAS Collaboration. *Measurement of $W^\pm Z$ production cross sections and gauge*
2238 *boson polarisation in pp collisions at $\sqrt{s} = 13$ TeV with the ATLAS detector*. Eur.
2239 Phys. J. C 79 (2019), p. 535. arXiv: 1902.05759 [hep-ex] (cit. on p. 79).
- 2240 [163] G. Cowan, K. Cranmer, E. Gross, and O. Vitells. *Asymptotic formulae for likelihood-*
2241 *based tests of new physics*. The European Physical Journal C 71.2 (Feb. 2011). ISSN:
2242 1434-6052. arXiv: 1007.1727 [physics.data-an]. URL: <http://dx.doi.org/10.1140/epjc/s10052-011-1554-0> (cit. on p. 83).

- 2244 [164] J. Neyman and E. S. Pearson. *IX. On the problem of the most efficient tests of*
2245 *statistical hypotheses.* Philosophical Transactions of the Royal Society of London.
2246 Series A, Containing Papers of a Mathematical or Physical Character 231.694-706
2247 (1933), pp. 289–337 (cit. on p. 83).
- 2248 [165] S. S. Wilks. *The large-sample distribution of the likelihood ratio for testing composite*
2249 *hypotheses.* Annals of Mathematical Statistics 9.1 (1938), pp. 60–62 (cit. on p. 84).
- 2250 [166] T. Junk. *Confidence level computation for combining searches with small statistics.*
2251 Nuclear Instruments and Methods in Physics Research Section A: Accelerators, Spec-
2252 trometers, Detectors and Associated Equipment 434.23 (Sept. 1999), 435443. ISSN:
2253 0168-9002. arXiv: [hep-ex/9902006 \[hep-ex\]](https://arxiv.org/abs/hep-ex/9902006) (cit. on p. 85).
- 2254 [167] A. L. Read. *Modified frequentist analysis of search results: The CLs method.* Tech.
2255 rep. CERN-OPEN-2000-205. Presented at Workshop on Confidence Limits, Geneva,
2256 Switzerland. CERN, 2000. URL: <https://cds.cern.ch/record/451614> (cit. on p. 85).
- 2257 [168] M. van Beekveld, A. Kulesza, and L. Moreno Valero. *Threshold Resummation for the*
2258 *Production of Four Top Quarks at the LHC.* Phys. Rev. Lett. 131 (21 2023), p. 211901
2259 (cit. on p. 97).
- 2260 [169] ATLAS Collaboration. *Preliminary analysis of the luminosity calibration of the AT-*
2261 *LAS 13.6 TeV data recorded in 2022.* ATL-DAPR-PUB-2023-001. 2023. URL: <https://cds.cern.ch/record/2853525> (cit. on p. 97).